Theory and Interpretation of L-shell X-ray Absorption Spectra.

Alexey I. Nesvizhskii

A dissertation submitted in partial fulfillment of
the requirements for the degree of

Doctor of Philosophy

University of Washington

2001

Program Authorized to Offer Degree: Department of Physics

University of Washington

Graduate School

This is to certify that I have examined this copy of a doctoral dissertation by

Alexey I. Nesvizhskii

and have found that it is complete and satisfactory in all respects,
and that any and all revisions required by the final
examining committee have been made.

Chair of Supervisory Committee:

_____

John J. Rehr

Reading Committee:

_____

John J. Rehr

_____

George F. Bertsch

_____

Edward A. Stern

Date: _____

In presenting this dissertation in partial fulfillment of the requirements for the Doctoral degree at the University of Washington, I agree that the Library shall make its copies freely available for inspection. I further agree that extensive copying of this dissertation is allowable only for scholarly purposes, consistent with "fair use" as prescribed in the U.S. Copyright Law. Requests for copying or reproduction of this dissertation may be referred to Bell and Howell Information and Learning, 300 North Zeeb Road, Ann Arbor, MI 48106-1346, to whom the author has granted "the right to reproduce and sell (a) copies of the manuscript in microform and/or (b) printed copies of the manuscript made from microform."

Signature_____

Date_____

University of Washington

Abstract

Theory and Interpretation of L-shell X-ray Absorption Spectra.

by Alexey I. Nesvizhskii

Chair of Supervisory Committee:

Professor John J. Rehr
Department of Physics

X-ray absorption near edge structure (XANES) directly reflects the electronic structure in a material. However, despite significant progress in XANES theory, the quantitative analysis of XANES is not fully developed and remains a challenge.

In this work, a detailed analysis of the $L_{2,3}$ edge XANES in transition metals was performed using relativistic, self-consistent real space Green's function code FEFF8. Several prescriptions for taking into account core hole in calculations of x-ray absorption spectra (XAS) were discussed. It was found that in most cases of $L_{2,3}$ edge XANES in transition metals, the initial state (ground state) calculations were in the best agreement with experimental data.

A procedure was developed for quantitative applications of the sum rules for XAS, e.g., for x-ray magnetic circular dichroism and for obtaining hole counts. The approach is based on theoretical atomic calculations of transformations relating various experimental spectra to corresponding operator-spectral densities. This approach overcomes the difficulties of background subtraction and hole-count normalization of other sum rule analysis methods and yields quantitative values for spin- and orbital-moments from experimental absorption spectra. The developed approach was theo-

retically tested and applied to experimental XAS data in Cu, Ni, Co, Fe, and other materials.

Hole counts obtained from XAS are often interpreted in terms of free-atom occupation numbers or Mülliken counts. We demonstrated that renormalized-atom (RA) counts are a better choice to characterize the configuration of occupied electron states in molecules and condensed matter. A projection-operator approach was introduced to subtract delocalized states and to determine such hole counts from XAS quantitatively. Theoretical tests for the s- and d-electrons in transition metals showed that the approach works well.

A formalism was developed based on time dependent local density approximation (TDLDA) theory that takes into account polarization-type many body effects. This effect, which is essentially a screening of the local x-ray field due to the Coulomb interaction, mostly affects dipole matrix elements. The effect is most important for soft x-rays with energies less than 1 keV. Results of the TDLDA calculations for the L_3/L_2 white-line ratio in $3d$ metals are in good agreement with experiment.

TABLE OF CONTENTS

LIST OF FIGURES

LIST OF TABLES

ACKNOWLEDGMENTS

I would like to thank many people who helped me during various stages of my graduate studies. I am especially indebted to my thesis advisor John J. Rehr for his invaluable guidance and support during all these years, and for suggesting many interesting projects that are parts of this dissertation. I am also very grateful to Alexei Ankudinov for his constant assistance during the entire time of this thesis project. I would like to express my gratitude to Professors Edward Stern, George Bertsch, and Klaus Baberschke for many valuable discussions, and to all members of the FEFF project, especially Anna Poiarkova and Luke Campbell, for their assistance. Also, I would like to thank Klaus Baberschke, Li-Shing Hsu, Wilhelm Fabrice, and Joe Stöhr for fruitful discussions and for providing experimental data, and Frank de Groot for his help with the atomic multiplet code. Finally, I would like to thank my family and, most of all, my dearest friend, Cindy for their love, understanding, and endless support.

DEDICATION

I dedicate this dissertation to my grandfather Boris Ilyich Nesvizhskii

Chapter 1

INTRODUCTION

Recent advances both in theory and analysis methods over the past decade have revolutionized the technique of extended x-ray absorption fine structure (EXAFS). EXAFS refers to the oscillatory structure in the x-ray absorption coefficient beyond about 40 eV of threshold, where the photoelectron scattering responsible for this phenomena is relatively weak. EXAFS has matured into a powerful and widely used technique for studying local atomic structure and vibrational properties of solids. The EXAFS technique has been successfully applied to biological systems, amorphous, glass and liquid materials, semiconductors, nanostructures and other systems. Many excellent reviews of the subject are available, see e.g. [1, 2].

Now there is a hope that x-ray absorption near edge structure (XANES), which refers to first 40 eV above the edge, can also become a reliable and direct way of obtaining local chemical information of complex and disordered materials. The recent progress in understanding XANES is based on the development of modern relativistic multiple scattering (MS) calculation methods. Several *ab initio* codes for calculations of XANES are available [3, 4, 5, 6, 7].

The L-shell x-ray absorption is less understood than the K-shell. In XANES region, L-shell absorption spectra are often the most interesting and informative, especially in the case of transition metals. $L_{2,3}$ edge absorption spectra can provide quantitative information about the electronic structure at or above the Fermi level and other information of great importance for studying charge transfer, catalysis, and

x-ray magnetic circular dichroism (XMCD) in these systems. Theoretical calculations and interpretation of L-shell XANES and XMCD spectra is the main topic of this dissertation.

L_3 and L_2 edges in XAS correspond to processes in which an x-ray photon is absorbed by promoting an electron from the $2p_{1/2}$ and $2p_{3/2}$ core states respectively. The most prominent and important feature in most $L_{2,3}$ edge spectra in transition metals is the so called white line, i.e. the enhanced absorption right near the absorption edge. These peaks were first correctly interpreted by Mott [8] as being due to transitions from $2p$ to unoccupied d-like states near the Fermi level. In case of L_1 absorption the dipole allowed transitions are from $2s$ to p-like states, and the absorption does not contain any sharp lines. The peaks in $L_{2,3}$ edge absorption have been called white lines because they were first observed as overexposed regions on the photographic film originally used to record x-ray-absorption spectra.

Intensity of the white-line depends on the number of unoccupied states in the d band of the metal. Therefore, x-ray absorption spectroscopy (XAS) can be used to directly probe unoccupied excited states of a system. Determination of hole counts from XAS has been of interest for many years. Already in the 1970s, the Pt white line was related to the number of d-holes by Brown, Peierls, and Stern [9] and later by Mattheiss and Dietz [10].

In recent years, a related x-ray absorption technique called x-ray magnetic circular dichroism has emerged as one of the most effective tools for obtaining information about magnetic systems. The XMCD effect, that is the difference in absorption of right and left circular polarized light, had been first predicted by Erskine and Stern [11] in 1975 and experimentally observed by Schütz et al. [12] twelve years later. The XMCD signal is directly related to the spin and orbital polarization of the final state and has unique element specific properties. Various XAS and XMCD sum rules have been used to investigate spin and orbital moments in $3d$ transition metals [13]. In principle, these sum rules provide a way of determining these properties from

experiment – information often hard to obtain with other techniques. However, the practical application of the sum rules is complicated by the presence of contributions to the XAS from both localized orbitals and delocalized atomic continuum states. Their separation is typically done using an *ad hoc* step function subtraction of the delocalized states, but this procedure is not well justified and is reexamined here [14, 15].

A fully quantitative treatment of XANES remains challenging, mostly due to many-body effects, such as core hole effect, multiplet splitting, the photoelectron self energy, and inelastic losses. The transition of an electron from a deep core level into the unoccupied orbital results in the creation of a core hole in XAS process. The creation of a positively charged core hole changes the effective potential seen by the residual electrons. This, in turn, leads to changes of the photoelectron wave function and modified x-ray absorption absorption coefficient. A fully quantitative treatment of the core hole effect in XAS is not yet developed, and the calculations are typically carried out in two limits, namely for static initial (ground state) and final state (with a core hole) potentials [16]. The question of whether XANES is a measure of the ground state or excited (modified due to presence of a core-hole) electron density of states is of great importance for studying charge transfer, catalysis, and magnetic circular dichroism in transition metals.

Another relevant many-body effect is a dielectric polarization-type effect [17]. The external x-ray field acts on all electrons in the systems and distorts the atomic charge cloud. In response to the perturbation the electrons redistribute themselves and produce internal screening (or antiscreening) fields which in turn can strongly modify the photoabsorption cross-section. This effect mostly affects dipole matrix elements and is important for soft x-rays with energies less than 1keV. It is well known [18, 19] that the single-electron theory of XANES, which does not take the local field into account, fails to describe experimentally observed L_3/L_2 white line ratio in transition metals.

1.1 Goals

The work presented here deals with different aspects of x-ray absorption near edge theory and *ab initio* codes for accurate calculations, with a main focus on the L shell. The main goals of this dissertation are:

- Quantitative interpretation and extensive *ab initio* calculations of the L-shell XANES and XMCD spectra of $3d$ transition metals and metallic systems.

- To develop a procedure for quantitative applications of the sum rules for x-ray absorption spectra, e.g. for XMCD and for obtaining hole counts from experiment.

- To develop a formalism based on time-dependent local density function theory to deal with local field effects in x-ray absorption.

In order to achieve these goals, we have done the following:

- Calculated electronic structure and XANES spectra of $3d$ transition metals using the real space Green's function code FEFF8 and the linearized augmented plane wave code WIEN97.

- Check the applicability of the final state rule to describe the core-hole effect on absorption spectra.

- Presented an interpretation of the spectral features in the Ni $L_{2,3}$ XANES and XMCD signals, based on both one-electron multiple-scattering and atomic-multiplet calculations. Performed a detailed comparison between experimental and theoretical XANES spectra of intermetallic systems Ni_3Al, Ni_3Ga, Ni_3In, and NiGa.

- Developed a quantitative relationship between the projected density of states and x-ray absorption spectra.

- Suggested an unambiguous way to separate contributions from delocalized (continuum) states to x-ray absorption, based on projection on atomic states and renormalized atom model.

- Developed a procedure for quantitative applications of the sum rules for x-ray absorption spectra based in part on transferable, atomic calculations of linear relations between XAS and various spectral densities. Theoretically tested the developed approaches and applied them to experimental data for Cu, Ni, Co, and Fe to extract the values of spin and orbital moments and hole counts in these materials.

- Extended the theoretical approach of Zangwill and Soven [17] based on time dependent local density function formalism (TDLDA) to take into account polarization-type many body effect (local field effect) on $L_{2,3}$ edge XAS in transition metals. Calculated $L_{2,3}$ XANES spectra and the L_3/L_2 white line ratio in $3d$ transition metals including the local field effects.

1.2 Dissertation overview

Here we give a brief overview of this dissertation. In Chapter 2 we review the most important concepts of the single electron theory of x-ray absorption. In Chapter 3 we discuss L-shell XANES of $3d$ transition metals. There we provide an interpretation of the experimental data based on the results of single-electron multiple scattering calculations. We discuss several prescriptions for taking into account the core hole effect on x-ray absorption spectra, and point out some of the limitations of the single-electron approach. In Chapter 4 we use both single-electron multiple-scattering and atomic-multiplet theory to perform a comprehensive analysis of XMCD and XANES

spectra at the $L_{2,3}$ edges of bulk fcc Ni. XANES spectra of Ni_3Al, Ni_3Ga, Ni_3In, and NiGa materials are analyzed in Chapter 5. In Chapters 6 and 7 we investigate the sum rules for x-ray absorption spectra and develop a quantitative procedure for obtaining spin and orbital moments, and hole counts from XAS and XMCD spectra. We demonstrate how this approach overcomes the difficulties of background subtraction and hole-count normalization of other sum rule analysis methods. In Chapter 8 we are moving toward a more complete picture of the x-ray absorption and address the polarization-type many-body effect. There we extend the TDLDA formalism to deal with x-ray absorption in solids and calculate $L_{2,3}$ edge XANES in $3d$ transition metals including local field effect. Conclusions are given in Chapter 9.

1.3 Terminology in x-ray absorption

In an x-ray absorption experiment, light with intensity I is falling on the sample with width dx. The reduction in intensity due to the sample is dI. The measured absorption coefficient, defined as

$$\mu(E) = (dI/dx)/I \tag{1.1}$$

is simply connected to the total absorption cross section, if the concentration of absorbing atoms n_a is known:

$$\sigma_{tot}(E) = \mu(E)/n_a \ . \tag{1.2}$$

In Chapter 2 we will show that there is a natural theoretical separation of the total absorption coefficient $\mu(E)$ into a smooth embedded atom absorption $\mu_0(E)$ and an oscillating fine structure, which is conveniently described by the XAFS function,

$$\chi(E) = \frac{\mu(E) - \mu_0(E)}{\mu_0(E)} \quad . \tag{1.3}$$

There are a number of commonly used abbreviations, used in this paper:

- XAS - x-ray absorption spectra - $\mu(E)$

- EXAFS - extended XAFS - $\chi(E)$, E above 40 eV of threshold
- XANES - x-ray absorption near edge structure - $\mu(E)$, first 40 eV above the edge including edge and below
- XAFS - x-ray absorption fine structure - $\chi(E)$ including EXAFS and XANES
- XMCD - x-ray magnetic circular dichroism - difference in absorption of right and left circular polarized light
- LDA - local density approximation
- TDLDA - time-dependent LDA
- MS - multiple scattering

Chapter 2

SINGLE-ELECTRON THEORY OF X-RAY ABSORPTION

In this Chapter, we will review the single-electron theory of x-ray absorption. The accent is made on the multiple scattering formulation of the problem. For a good review of the subject one can refer to a recent manuscript by Rehr and Albers [2] and other papers [7, 20, 21, 22, 23, 24, 25] describing the details of the FEFF code used throughout this work.

2.1 Multiple scattering formula for the absorption coefficient

The total absorption cross-section can be calculated in practice by using the Fermi's Golden rule in one electron approximation. The nonrelativistic expression (in Gaussian units) has the following form:

$$\mu(\omega) = \frac{4\pi^2 e^2 c}{\omega} \sum_{i,f} \left| \langle \psi_f | \vec{r} \cdot \hat{\epsilon} e^{i\vec{k}\cdot\vec{r}} | \psi_i \rangle \right|^2 \delta(\hbar\omega + E_i - E) \,, \tag{2.1}$$

where ω is frequency of the x-rays with wave vector $\vec{k}$ and unit polarization $\hat{\epsilon}$, E_F is the Fermi level, and $\delta(E)$ is the Dirac delta function. The wave functions ψ_i and ψ_f refer, respectively, to the initial (occupied) and final (unoccupied) states of the effective one-electron Hamiltonian H for the initial state and H' for the final state, with energies E_i and E_f, respectively. The rest of the notations are standard. In the following more convenient atomic units ($\hbar = e = m = 1$, $c = 1/\alpha$, α being fine structure constant) will be used. The relativistic form of Eq. 2.1 can be obtained by substituting $\vec{p} \rightarrow c\vec{\alpha}$, where $\vec{\alpha}$ are the Dirac matrices. The formula 2.1 can be rewritten in terms of single-electron Green's function [26, 27] $G(\vec{r}, \vec{r}', E) = 1/(E - H' - \Sigma)$, H'

is the final state Hamiltonian, and Σ the electron self-energy. The advantage of this formulation is that we avoid the necessity of explicit calculations of wave functions. Using the spectral representation for G,

$$G(\vec{r},\vec{r}\,',E) = \sum_f \frac{\psi_f(\vec{r})\psi_f^*(\vec{r}\,')}{E - E_f + i\Gamma}\,, \tag{2.2}$$

where Γ is a net lifetime that includes both extrinsic and intrinsic loses, we obtain the following expression for the absorption

$$\mu(\omega) = -\frac{4\pi}{c\omega}\mathrm{Im}\sum_i \langle i|d_\epsilon^* G(\vec{r}\,',\vec{r},\omega+E_i)\,d_\epsilon|i\rangle\theta(\omega+E_i-E_F)\,, \tag{2.3}$$

where $d_\epsilon = c\vec{r}\cdot\hat{\epsilon}e^{i\vec{k}\cdot\vec{r}}$ is the dipole operator. The function θ is a step function that has to be added to exclude the poles in the Green's function lying below the Fermi level. The finite temperature effect is small and can be taken into account by using a broadened θ (i.e. Fermi) function of the form $\theta = 1/(1+\exp((\omega+E_i-E_F)/kT)$.

Because full-potential calculations are extremely difficult and time consuming, the scattering potential is often approximated as a sum of overlapping spherically symmetric potentials and is set to be zero in the interstitial region. Thus the single-electron Hamiltonian H is expressed to a good approximation as sum of the free electron Hamiltonian $H_0 = -\frac{1}{2}\vec{\nabla}^2 + V_{mt}$, where V_{mt} is the muffin-tin potential, and the scattering potential $V(\vec{r}) = \sum_i V_i(|\vec{r}-\vec{R}_i|)$. The multiple scattering approach is based on separation of the scattering potential into the potential of a single scatterer at the absorption site, "central atom" part, and all other scatterers ("scattering part"), $V = V_c + \sum_{i\neq c} V_i$. Accordingly, the Green's function $G(\vec{r},\vec{r}\,',E)$ can be separated into the central atom part $G^c = 1/(E-H_0-V_c+i\Gamma)$ and scattering part G^{sc}, $G = G^c + G^{sc}$. In the interstitial region the Green's function has a free particle form

$$G^0(\vec{r},\vec{r}\,',E) = -\frac{2k}{4\pi}\frac{e^{ik|\vec{r}-\vec{r}\,'|}}{k|\vec{r}-\vec{r}\,'|}\,, \tag{2.4}$$

where $k = \sqrt{2(E-V_{mt})}$. The total Green's function is found formally from the Dyson

series expansion in V,

$$G = G^0 + \sum_i G^0 V_i G^0 + \sum_{i,j} G^0 V_i G^0 V_j G^0 + \dots \,. \tag{2.5}$$

It is convenient to introduce the scattering t-matrix, $t_i = V_i + V_i G^0 t_i$ which sums all MS at a given site and rewrite the above expansion as

$$G = G^0 + \sum_i G^0 t_i G^0 + \sum_{i \neq j} G^0 t_i G^0 t_j G^0 + \dots \,, \tag{2.6}$$

where t_i is the scattering matrix at each scattering site. The total Green's function then can be written as a sum that starts and ends at the absorbing atom and contains only single scattering events at each atom

$$G = G^c + G^c \left[\sum_{c \neq i \neq c} t_i + \sum_{c \neq i \neq j \neq c} t_i G^0 t_j + \sum_{c \neq i \neq j \neq k \neq c} \cdots \right] G^c = G^c + G^{sc} \,. \tag{2.7}$$

The first term, G^c is the background absorption from the absorbing (central) atom alone, while the successive terms, grouped as G^{sc}, represent the contributions from single scattering, double scattering, and etc.

The central atom Green's function, $G^c = G^0 + G^0 t_c G^0$, and the scattering part G^{sc} can be calculated as

$$\begin{aligned} G^c(\vec{r}, \vec{r}\,', E) &= -2k \sum_L (R_L(\vec{r}_<, E) N_L(\vec{r}_>, E) + i R_L(\vec{r}, E) R_L(\vec{r}\,', E) \,, \\ G^{sc}(\vec{r}, \vec{r}\,', E) &= -2k \sum_{L, L'} R_L(\vec{r}, E) R_{L'}(\vec{r}\,', E)\, G^{sc}_{Lc, L'c}(E) \,, \end{aligned} \tag{2.8}$$

where $L = (\ell, m)$, $R_L(\vec{r}, E) = i^\ell R_\ell(r, E) Y_L(\hat{r})$ and $N_L(\vec{r}, E) = i^\ell N_\ell(r, E) Y_L(\hat{r})$ are the regular and irregular solutions of the Shrödinger equation in a central potential V_c. The functions R_ℓ and N_ℓ are normalized in such a way that at distances larger than the central atom muffin tin radius, r^c_{mt}, they behave as $R_\ell(r, E) = \cos(\delta_\ell) j_\ell(kr) + \sin(\delta_\ell) n_\ell(kr)$ and $N_\ell(r, E) = -\sin(\delta_\ell) j_\ell(kr) + \cos(\delta_\ell) n_\ell(kr)$.

The total scattering-propagator matrix $G^{sc}_{L\vec{R}, L'\vec{R}'}$ can be obtained by matrix inversion of the full-multiple scattering equation

$$G^{sc}_{Li, L'i'} = e^{(i\delta_\ell + i\delta_{\ell'})} (\mathbf{1} - G^0 t)^{-1} G^0 \,, \tag{2.9}$$

where G^0 is the dimensionless two-center free propagator $G^0_{Li,L'i'}$ and the dimensionless scattering $t-$matrix $t_{Li,L'i'} = e^{i\delta_{\ell,i}} \sin(\delta_{\ell,i})\delta_{i,i'}\delta_{L,L'}$, $\delta_{\ell,i}$ being partial wave phase shifts for all different sites in solid. Note that we need to calculate only the submatrix of $G_{Li,L'i'}$ for which i and i' both refer to the central (absorbing) atom. A related approach based on the so-called scattering-path operators τ has also been used in many treatments of XANES [28, 29].

Finally, we arrive at following MS expression for the absorption coefficient:

$$\begin{aligned} \mu(\omega) &= -\frac{8\pi\, c\, k}{\omega} \mathrm{Im} \sum_{i,L,L'} \langle i|d^*_\epsilon|R_L\rangle \\ &\quad \left[-i\,\delta_{L,L'} + e^{i(\delta_\ell+\delta_{\ell'})} G^{sc}_{Lc,L'c}(\omega+E_i)\right] \langle R_{L'}|d_\epsilon|i\rangle \theta(\omega+E_i-E_F)\,. \end{aligned} \tag{2.10}$$

As one can see from 2.10 the expression for $\mu(\omega)$ in the multiple-scattering formalism can be factored in terms of a smoothly varying (embedded) atomic contribution $\mu_0(\omega)$ modulated by the x-ray absorption fine structure or XAFS, χ, due to MS from the environment [27], i.e,

$$\mu(\omega) = \mu_0(\omega)\,[1+\chi(\omega)]\ . \tag{2.11}$$

Note that the atomic-background absorption $\mu_0(\omega)$ is defined by the central potential V_c rather than being that for a "free-atom" [30]. This factorization of μ clearly separates atomic and scattering parts and is very important for interpretation of x-ray absorption fine structure experiments. The XAFS spectrum $\chi(\omega)$ contains detailed structural information, such as interatomic distances and coordination numbers. A quantitative parametrization of $\chi(\omega)$ in term of this parameters (the EXAFS equation) is well established [27, 31, 32, 33].

2.2 Relativistic x-ray absorption

The relativistic generalization of the MS theory is straightforward [34, 24]. One only has to change the basis from $|LS\rangle$ to $|J\rangle$ (or $|\kappa\rangle$) which are connected through Clebsch-Gordon coefficients, and to calculate t_{Ji} for each $j = l \pm 1/2$ instead of t_{Li}. . Regular

and irregular functions R_L^α and N_L^α are solutions of the Dirac equation, with index α labeling the spinor components. As a results, all expressions will have an additional summation over index α, but otherwise will not change.

Since spin-orbit interaction is negligible in the interstitial region, one can use the same two center Green's function matrix elements $\langle LS|G^0|L'S'\rangle = G^0_{L,L'}\delta_{S,S'}$. This can be used even for spin-dependent potentials.

If one neglects spin-dependent effects, than the spin-orbit interaction within this approach is treated exactly. Simultaneous treatment of spin and relativistic effects required for calculations of XMCD in magnetic materials is discussed in Chapter 4.

2.3 Multipole matrix elements

The relativistic expression for the matrix elements of multipole transitions $\langle n\kappa m|\vec{\alpha}\cdot\hat{\epsilon}\,\hat{e}^{i\vec{k}\vec{r}}|n'\kappa'm'\rangle$ are given in Grant's review [35], an also summarized in [36]. The quantum number is defined as $\kappa = \ell$ if $j = \ell - 1/2$, and $\kappa = -\ell - 1$ if $j = \ell + 1/2$. Without any loss of generality we can consider the vector $\vec{k}$ along the z-axis and right and left circular polarizations $\hat{\epsilon}_1 = -(\hat{\epsilon}_x + i\hat{\epsilon}_y)/\sqrt{2}$ and $\hat{\epsilon}_{-1} = (\hat{\epsilon}_x - i\hat{\epsilon}_y)/\sqrt{2}$. Expression for matrix elements can be most easily obtained using irreducible tensor algebra [37, 38]. Using the decomposition of $e^{i\vec{k}\cdot\vec{r}}$ in terms of the irreducible tensors $C_0^{(\ell)}$

$$e^{i\vec{k}\cdot\vec{r}} = \sum_{\ell=0}^{\infty} i^\ell (2\ell+1) j_\ell(kr) C_0^{(\ell)}(\hat{r})\,. \tag{2.12}$$

In the dipole approximation ($\ell = 0$) the matrix element have the following form

$$\langle n\kappa m|\,\vec{\alpha}\cdot\hat{\epsilon}\,\hat{e}^{i\vec{k}\vec{r}}|n'\kappa'm'\rangle = (-1)^{j-m}\begin{pmatrix} j & L & j' \\ -m & p & m' \end{pmatrix} R^{\ell L}_{\kappa\kappa'}\,. \tag{2.13}$$

The reduced matrix element $R_{\kappa\kappa'}$ is

$$R_{\kappa\kappa'} = i\int dr\; j_0(kr)\left[P_\kappa Q_{\kappa'} C_{\kappa\kappa'}(1) + Q_\kappa P_{\kappa'} C_{\kappa\kappa'}(-1)\right] \quad , \tag{2.14}$$

where $C_{\kappa\kappa'}(\beta)$, with $\beta = \pm 1$ corresponding to the upper (lower) component of Dirac spinor, can be expressed as [36]

$$C_{\kappa\kappa'}(\beta) = \beta(-1)^{(\Delta-1)} \frac{\sqrt{|(\Delta+\beta)(2\kappa+\Delta)(2\kappa+\Delta-1)(2\kappa+\Delta+1)|}}{2\kappa+\beta} \tag{2.15}$$

where $\Delta = 0$ if $\kappa = -\kappa'$, otherwise $\Delta = \kappa' - \kappa = \pm 1$. These are the only possible pairs of $\kappa\kappa'$ in the dipole approximation.

As a result, for a smooth atomic contribution $\mu_0(\omega)$ for transitions from an initial state with n, j one obtains:

$$\mu_0(\omega) = \frac{8\pi ck}{3\omega} \sum_{k'} |R_{\kappa\kappa'}|^2 \quad , \tag{2.16}$$

where factor $1/3$ comes from summation over m and m'. To obtain an expression for the fine structure $\chi(\omega)$ we can define normalized reduced matrix elements as

$$\tilde{R}_{\kappa\kappa'} = e^{i\delta_{j'}} R_{\kappa\kappa'} / [\Sigma_{\kappa'} |R_{\kappa\kappa'}|^2 / 3]^{1/2} \, , \tag{2.17}$$

so that the equation for the fine structure, $\chi = (\mu - \mu_0)/\mu_0$, is

$$\chi = \sum_{\kappa'\kappa''} \tilde{R}_{\kappa\kappa'} \tilde{R}_{\kappa\kappa''} \begin{pmatrix} j & 1 & j' \\ m & \epsilon & m' \end{pmatrix} \begin{pmatrix} j & 1 & j'' \\ m & \epsilon & m'' \end{pmatrix} \tilde{G}^{sc}_{J',J''} \, , \tag{2.18}$$

where

$$G^{sc}_{J,J'}(E) = \langle J|LS\rangle G^{sc}_{L,L'}(E) \langle L'S'|J'\rangle \, . \tag{2.19}$$

2.4 Density of states

The radial and energy dependence of the electron density can be calculated using the same single electron Green's function operator discussed above. The total electron density at point $\vec{r}$ is given by

$$\rho(\vec{r}) = -\frac{2}{\pi} \mathrm{Im} \int_{-\infty}^{E_F} dE \; G(\vec{r}, \vec{r}, E) \tag{2.20}$$

where the factor of 2 comes from summation over spin indices. The density of one electron states is

$$\rho(E) = -\frac{2}{\pi} \mathrm{Im} \int_{-\infty}^{E_F} d\vec{r} \; G(\vec{r}, \vec{r}, E) \, . \tag{2.21}$$

2.5 Real space Green's function code FEFF8

The self-consistent field, real space Green's function code FEFF8 has a number of advantages which are important for a quantitative description of XANES. The code determines overlapped MT potentials self-consistently in the presence or absence of a core-hole. It naturally includes final-state broadening due to core hole lifetime and photoelectron energy dependent self-energy (usually the Heidin-Lundqvist model [39]). The code permits quantitative calculations of XAS up to very high energies (of order 1000 eV above threshold), while traditional band-structure codes usually are limited to 20-30 eV above the edge. In addition, it incorporates effects of correlated vibrations and disorder. Finally, the code is semi-automated, thereby making XAS calculations and the interpretation of spectral features in terms of geometrical and electronic structure readily accessible. In the rest of this section, we will describe key elements of the FEFF8 code.

2.5.1 Multiple scattering expansion

The scattering contribution $G^{sc}_{L,L'}(E)$ may be expressed by the MS path expansion [40] in terms of the two center matrix elements of the free propagator G^0 and the scattering t-matrix, i.e.,

$$\begin{aligned} G^{sc}_{Lc,L'c}(E) &= \sum_{i\neq c} G^0_{Lc,L_1 i} t_{\ell_1 i} G^0_{L_1 i,L'c} + \\ &+ \sum_{i\neq c, i\neq j, j\neq c} G^0 t_i G^0 t_j G^0 + \cdots, \end{aligned} \tag{2.22}$$

where summation over intermediate angular momentum indices is implied. Here we use dimensionless G^0 and t as defined in [40]. The summation restrictions prohibit the photoelectron from scattering from the same atom twice in a row in a MS path of any order. The propagators $G^0_{Li,L'i'}$ are calculated using the exact Rehr-Albers (RA) algorithm[40].

Usually a finite MS path expansion converges well at high energies but can fail in

the XANES region. Typically non-convergence is due to large MS contributions from short bonds at low energy. To handle this situation the full MS method is applied to a finite cluster around the central atom. In full MS treatments, the infinite series in Eq. 2.22 is summed implicitly by matrix inversion, i.e.,

$$G = G^0(1 - tG^0)^{-1} = (1 - G^0t)^{-1}G^0. \tag{2.23}$$

Because the partial wave phase shifts decay exponentially with increasing ℓ beyond $\ell_{max} \sim kr^c_{\rm mt}$, where $r^c_{\rm mt}$ is the MT radius of the central atom, and because the cluster size is relatively small, G can be calculated with reasonable computer resources. The time required for the matrix inversion in Eq. (2.23) scales as the cube of the dimension $N(\ell_{max}+1)^2$ of G, where N is the number of atoms in the cluster.

As shown by Schaich [26], this real-space matrix-inverse formulation is formally similar to the KKR band structure approach and the X_α MS approach. However, in the KKR and X_α methods discrete wave functions are calculated using the Lippman-Schwinger equation of MS theory, while in the RSMS method, the electron Green's function is calculated, which implicitly sums over all one-particle states. This distinguishes the RSMS method from most other electronic structure methods [41, 42].

2.5.2 Self-consistent muffin tin potentials

The SCF approach is essential for calculations of charge transfer between atoms and also for an accurate determination of the Fermi level. The iterative procedure for calculating scattering potentials is outlined below. Initially, a relativistic Dirac-Fock atomic code [22] is used to obtain free atomic densities. The scattering potentials are calculated by overlapping the free atomic densities within the muffin tin approximation using Mattheiss prescription [10]. The ground state von Barth-Hedin exchange-correlation potential [43] is used on all iterations. After the SCF loop is finished, the Hedin-Lundqvist energy dependent self-energy [39] is added, but only for x-ray absorption calculations. Next, the density of states (DOS) is calculated for

each distinguishable site i in a solid or molecule. The space integration of $\rho_i(r, E)$ yields $\rho_i(E)$, the DOS. The Fermi level is found by energy integration of the DOS. The energy integration of $\rho_i(r, E)$ to the Fermi level gives the new total electron density $\rho_i(r)$. The energy integration is done by contour integration in the upper half of the complex E plane. This greatly simplifies calculations since the spectral quantities of interest are much smoother above the real axis. The space integration is done in way that is similar to the atomic sphere approximation (ASA). The Norman radii R_{nm} (i.e., the analog of the Wigner-Seitz radii of neutral spheres) are calculated using the definition

$$\int_0^{R_{nm}} dr\, 4\pi r^2 \rho_i(r) = Z_i, \tag{2.24}$$

where Z_i is the charge of the i-th nucleus. These Norman radii are kept fixed for all iterations. The density $\rho_i(E)$ is then can be obtained as

$$\rho_i(E) = \int_0^{R_{nm}} d^3 r \rho_i(r, E). \tag{2.25}$$

This method, as in case of ASA, double counts charge in the region where two Norman spheres overlap and does not count charge at all in the region not covered by any of Norman spheres. However, is a fairly good practical approximation to account for charge transfer within the MS approach in XAS calculations when the density is slowly varying in space. On the last step of each iteration, the new position of the Fermi level and the new densities around each i-th site are found. Once the new density is calculated it is used to start a new iteration. The Broyden algorithm is used to achieve the self-consistency.

2.5.3 Inelastic mean free path

The photoelectron propagating in solid will eventually lose its energy due to creation of elementary excitations (plasmons, electron-hole pairs, etc.). This can be accounted for by introducing a complex energy-depended self-energy Σ. In many cases, the

Heidin-Lundqvist self-energy gives the best agreement with experiment. In addition, one should add the core hole broadening Γ_{ch} which describing the interaction of the photoelectron with passive electrons, which is assumed independent of the energy of outgoing photoelectron. Both damping factors can be combined in the total optical potential for the absorption measurement:

$$V_{opt}(k) = \Gamma_{ch}/2 + |\mathrm{Im}(\Sigma(k))| \,. \tag{2.26}$$

The corresponding mean free path is then $\lambda_k = k/V_{opt}(k)$.

2.5.4 Debye-Waller factors

To account for thermal vibration, a factor $\exp(-\sigma^2_{ii'}k^2)$ to each free propagator $G^0(\mathbf{R}_i - \mathbf{R}_{i'})$ for each pair of atoms i, i'. Effects of lattice vibrations can only be taken into account approximately in the FMS technique. This approximation yields the correct thermal factor only for the single scattering terms in the harmonic approximation. The thermal factors for MS paths will not have the correct weight, but in any case, their contribution will be reduced both by thermal factors and by the mean free path.

Chapter 3

L-SHELL X-RAY ABSORPTION IN TRANSITION METALS

In this Chapter we discuss XANES of $3d$ transition metal L edges [44]. The interpretation of the experimental data is based on the results of single-electron multiple scattering calculations. We make a detailed comparison with experimental data and with results of band structure codes. We also discuss several prescriptions for taking the effect of a core hole on x-ray absorption spectra. The question of whether XANES is a measure of the ground state or excited (modified due to presence of a core-hole) electron density of states is of great importance for studying charge transfer, catalysis, and magnetic circular dichroism in transition metals. Based on the results presented in this Chapter, and Chapters 4 and 5, where we focus on XAS and XMCD spectra of Ni and Ni compounds, we will show in Chapters 6 and 7 that the area under the white line can provide quantitative information about the number of unoccupied d holes at or above the Fermi level. We will also point out the limitations of the single-electron approximation, which will be further discussed in Chapter 8.

3.1 Electronic structure and XANES

The fact that the near edge region in the x-ray absorption reflects the electronic structure of the corresponding final state band was understood long time ago. The white line peaks in the $L_{2,3}$ edge XAS were first correctly interpreted by Mott [8] as being due transitions from $2p$ to unoccupied d-like states near the Fermi level. Intensity of the white-line depends on the number of unoccupied states in the d band

of the metal. The white lines are quite intense for the early transition metals of each transition series, but almost absent in case of metals with almost filled d band such as Cu. In most cased, L_3 and L_2 edges have relatively similar spectral shapes. One of the interesting exceptions is metallic Pt where a white line is observed at the L_3 edge but is almost absent at the L_2 edge. In fact, it was Pt that initially attracted the attention to studies of x-ray absorption in metals.

According to dipole selection rules, an electron from a core state of p symmetry can have a transition into a final state of s or d symmetry. The contribution from transitions to the final s states is negligible. The density of s-symmetric final states is relatively small and spread over an extended energy range. As a result, the radial part of the dipole transition matrix element for s states is approximately an order of magnitude smaller than that for d states, and the d density of final states is large and narrow. The density of states for fcc-Cu resolved for the orbital angular momentum ℓ is shown in Fig. 3.1. The size of the cluster used in the calculation is 125 atoms, and the resulting DOS curves were convoluted with a small 0.1 eV broadening factor. The electronic structure of fcc-Cu is very typical for transition metals. The s and p density of states can be described as a free-electron-like band. The d-band complex is narrow and atomic like (about 5 eV wide), with its peak located about 1.4 eV below the Fermi level. Unlike purely atomic case, though, the d-like band in metallic Cu is not completely filled, and the number of d electrons in the occupied part of the d band is around 9.55.

The white lines at the L_2 and L_3 edge onsets increase in intensity with decreasing Z across the transition metal series, reflecting changes in filling of the d band. To completely understand the $L_{2,3}$ edge x-ray absorption, we need to consider the electronic structure in relativistic case. The initial $2p$ state is splitted due to spin-orbit interaction into $2p_{1/2}$ and $2p_{3/2}$ levels that give rise to L_2 and L_3 absorption edges, respectively. The value of the spin-orbit splitting varies across the periodic table. It is quite large in case of Cu, around 20 eV, but gradually decreases when moving left

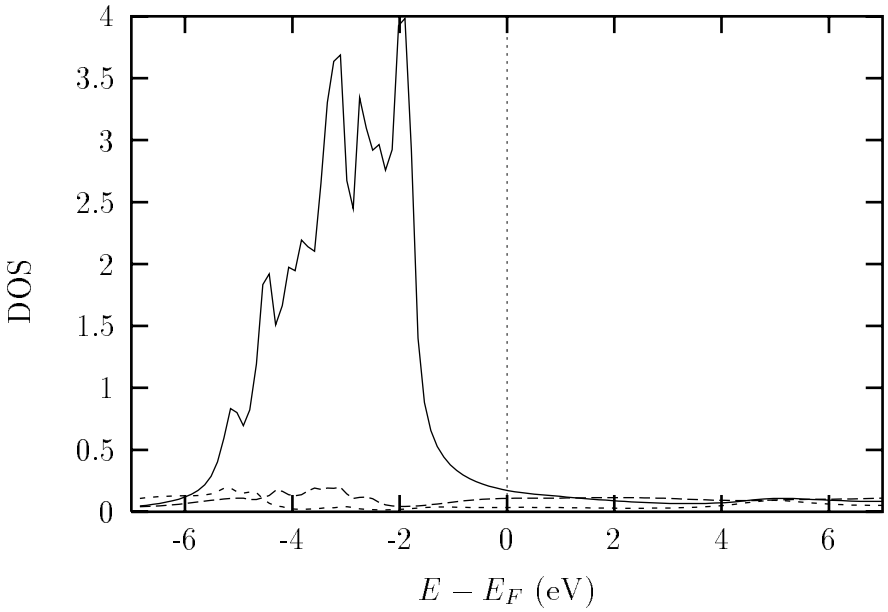

Figure 3.1: Projected ground state density of states in Cu. Solid line, long dashes, and short dashes correspond to the d, p, and s density of states respectively.

in the periodic table, and gets as small as 3 eV in Ca. As a result, the degree of overlap between L_3 and L_2 absorption edges increases when going from Cu to Ca. The spin-orbit splitting of the final d band is of the order of only 0.1 eV. The $d_{3/2}$ states are shifted toward higher energies, while the $d_{5/2}$ states are shifted toward lower energies. According to the relativistic dipole selection rules, the L_2 edge is represented by $2p_{1/2} \rightarrow d_{3/2}$ and $2p_{1/2} \rightarrow s_{1/2}$ transitions. The L_3 edge is due to transitions from $2p_{3/2}$ core state ($\kappa = 1$) to the final $s_{1/2}$ ($\kappa = 1$), $d_{3/2}$ ($\kappa = 2$), and $d_{5/2}$ ($\kappa = -3$) states above the Fermi level. The $2p_{1/2} \rightarrow d_{5/2}$ transition is the dominant one with around 90% of the total intensity. For both edges, L_3 and L_2, $2p \rightarrow s$ transitions contribute less than 5% of the total intensity. The absorption coefficient can be, to a good approximation, factorized in terms of the density of states and transition matrix elements. For L_3 and L_2 edge absorption one obtains [34]

$$\mu_{L_2} = \frac{1}{3}\rho_{s_{1/2}}\mathcal{M}^2_{p_{1/2}s_{1/2}} + \frac{1}{3}\rho_{d_{3/2}}\mathcal{M}^2_{p_{1/2}d_{3/2}} , \tag{3.1}$$

$$\mu_{L_3} = \frac{2}{3}\rho_{s_{1/2}}\mathcal{M}^2_{p_{3/2}s_{1/2}} + \frac{1}{15}\rho_{d_{3/2}}\mathcal{M}^2_{p_{3/2}d_{3/2}} + \frac{2}{5}\rho_{d_{5/2}}\mathcal{M}^2_{p_{3/2}d_{5/2}} .$$

Here $\rho_\kappa(E)$ is the unoccupied part of κ resolved density of states and $\mathcal{M}_{\kappa\kappa'}$ is the radial part of the transition matrix element for transitions from the core state with quantum index κ to the final state with index κ'. In case of $3d$ transition metals the relativistic effects are small, so that the shapes of the $d_{3/2}$ and $d_{5/2}$ density of state curves are quite similar which, in turn, leads to strong similarity between L_2 and L_3 absorption shapes. If spin-orbit interaction in the final state is neglected, then $\rho_{d_{5/2}}/\rho_{d_{3/2}} = 2/3$, and the relative magnitude of L_3 and L_2 edge intensities is 2:1, see Eq. 3.1, which just reflect the fact there are twice as many electron in the initial $2p_{3/2}$ level than in $2p_{1/2}$ level.

The relativistic effects in the final state are much more important in heavier atoms. In case of $4d$ transition metals they can be crucial for the correct description of $L_{2,3}$ edge x-ray absorption. For example, the white line at the L_2 absorption edge in metallic Pt is absent. This interesting effect is caused by the fact the unoccupied part of the final density of states is predominantly of $d_{5/2}$ character [9]. Due to spin-orbit interaction, the $d_{3/2}$ band is shifted toward lower energies and almost completely occupied.

3.2 Theoretical x-ray absorption spectra

Theoretical absorption spectra for fcc Cu metal calculated using the FEFF8 code are shown in Fig. 3.2. Calculations are done without a core hole (see next section). The plot shows L_3 and L_2 edge spectra separately, as well as the total spectrum. The shapes of the L_3 and L_2 spectra are very similar, and their relative intensities are close to the expected ratio of 2:1. Small differences between the two edges are due, to some extent, to the spin-orbit splitting within the $3d$ states. In addition, the L_2 edge has a larger core-hole lifetime broadening. Due to a significant overlap between L_3 and L_2 edges, calculated total spectrum above the L_2 edge has some extra oscillations

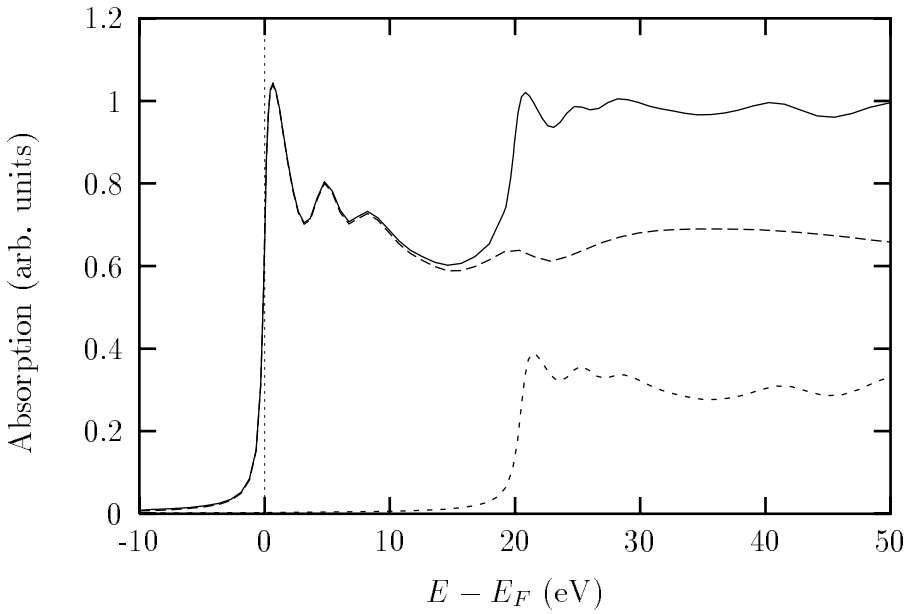

Figure 3.2: $L_{3,2}$ edge XANES in Cu. Solid line, long dashes, and short dashes correspond to the L_3, L_2, and the total spectrum respectively.

coming from the extended part of the L_3 absorption tail. We note that the thermal and structural disorder in the full multiple-scattering formalism are taken into account in an approximate way. We found that it is needed to add an extra factor $exp(-\sigma^2 k^2)$ (in addition to the usual value of the Debye-Waller factor for this material) in the propagator G^0, see Chapter 2, in order to obtain a better agreement with experiment in the region above the L_2 edge. So that the results for Cu presented in Fig. 3.2, and for other transition metals presented later in this Chapter, are obtained by using an additional $\sigma^2 \sim 0.01 - 0.05$.

Fig. 3.3 shows the d projected density of states aligned with the offset of the L_3 edge. As expected from Eq. 3.1, the absorption coefficient directly reflects the unoccupied part of the final density of states. All peaks in the spectrum can be traced back to corresponding peaks in the DOS curve, which in turn can be explained as van Hove singularities at the L and X point in the Brillouin zone [34, 45]. In Chapters 6 and 7 we will explore the relationship between DOS and XANES in more details and

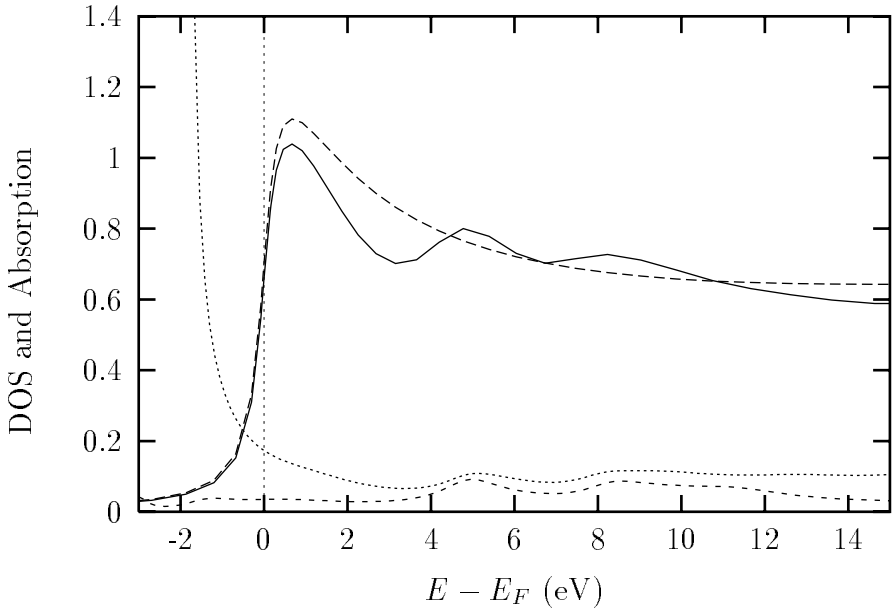

Figure 3.3: L_3 edge XANES (solid line) and d- and s-projected DOS (dashes and short dashes respectively) in fcc Cu. Also shown is the smooth atomic-like part of the absorption μ_0 (dots).

propose a quantitative approach for obtaining information about unoccupied part of the density of states from experimental XANES.

3.3 Treatment of the core hole

The transition of an electron from a deep core level into the unoccupied orbital results in the creation of a core hole in XAS process. Therefore, the initial (ground state) Hamiltonian and the final state Hamiltonian are different. A fully quantitative treatment of the core hole effect on XAS is not yet developed. Within the independent particle approximation calculations are typically carried out in two limits, namely for static initial and final state potentials. The "final state rule" [16] says that in the one-electron approximation the photoelectron states should be calculated in the presence of a core hole. On the other hand, the "initial state rules" says that the calculations should be done with a fully screened core hole (no core hole). In the

FEFF8 code, the core hole effect can be taken into account by putting a frozen core hole in the given core level. The SCF procedure then automatically screens the core hole. This approach yields a SCF treatment of core hole relaxation analogous to the Z+1 impurity approximation used by Zeller et al. [46] in the KKR formalism. As an approach intermediate between the final state rule (full core-hole) and the initial state rule (no core hole), one can calculate the photoelectron states in a potential that has a half electron removed from its core level, i.e. the so-called transition state rule suggested by Slater [47]. One can go even further and consider any fraction of an electron removed from the core level [48]. Since all prescriptions described above are *ad hoc*, the choice between the initial and final state rule is somewhat arbitrary and is usually made by comparing the results of calculations with experimental data. In many cases, for example in case of K-shell absorption in insulators such as BN [7], or in semiconductors [49], the final state rule gives a better agreement with experiment. However, in case of the L-shell absorption in transition metals, as discussed in the next section, the situations is opposite and the initial state rule is favorable. We stress that the question of whether x-ray absorption is a measure of the ground state or excited state DOS is of great importance for studying charge transfer, catalysis, and magnetic circular dichroism in transition metals and compounds. The generally accepted concept that the area under the white line in $L_{2,3}$ edge XANES of transition metals is directly proportional to the number of unoccupied d holes at or above the Fermi level, i.e. the ground state property, needs to be theoretically justified. The results presented in this Chapter demonstrate that it is indeed the case, at least for the transition metals with almost filled d band.

3.4 Comparison with experiment and discussion

Results of the calculations done with and without a core hole and experimental data for L_2 and L_3 edges of Cu are shown in Fig. 3.4. Remarkably, a better agreement

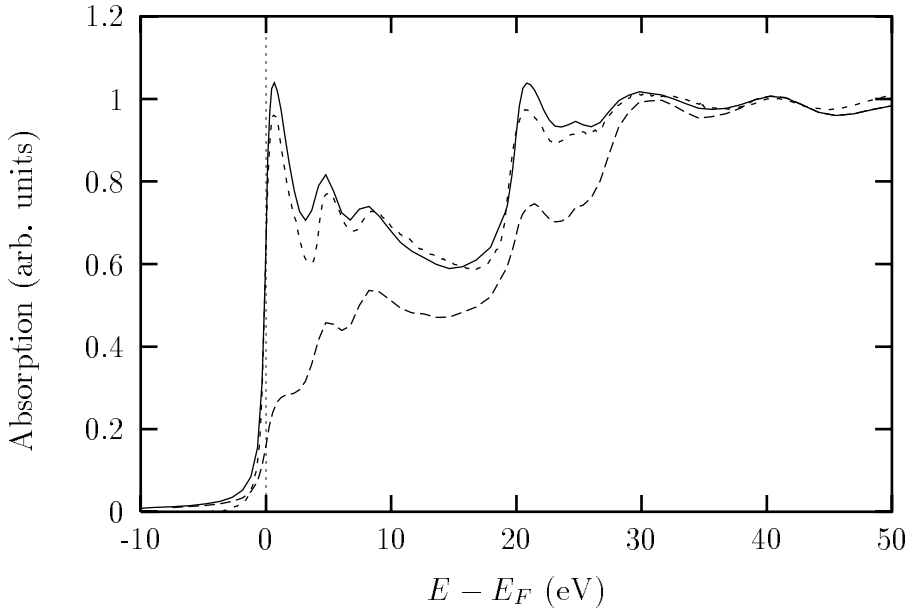

Figure 3.4: $L_{2,3}$ edge XANES of Cu, solid line and long dashes represent the results of calculations done without and with a core hole respectively, short dashes is experimental data.

with experimental data is obtained when the calculations are done without a core hole. The agreement between the theoretical spectrum calculated without a core hole and experiment is very good, both in terms of the integrated intensity and the fine structure. As we mentioned above, small differences between experiment and theory can be explained by an approximate treatment of Debye-Waller factors and structural disorder.

As one can observe from Fig. 3.4, there is a strong reduction of the calculated L_2 and L_3 edge white lines when a core hole is included in the calculation. The inclusion of a core hole leads to an energy shift of the d density of states due to electron - core hole interaction. The shift of the Fermi level, however, is much smaller. As a result, we observe a strong reduction, or even absence, of the white line in XANES when a core hole is taken into account. At the same time the p density of states, which is much broader that the d density of states, is basically unaffected by the presence

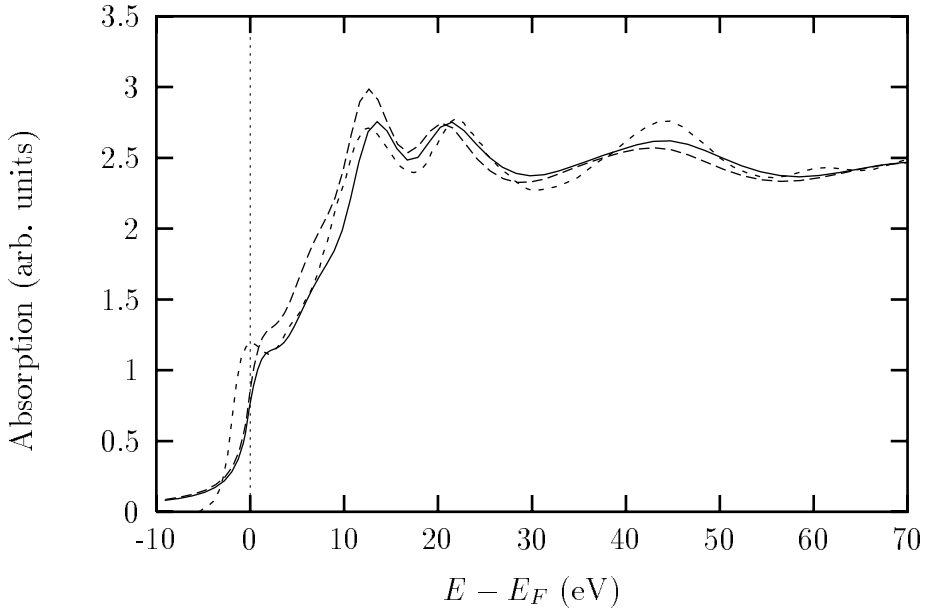

Figure 3.5: K edge XANES of Cu, solid line and long dashes represent the results of calculations done without and with a core hole respectively, short dashes is experimental data.

of a core hole. Consequently, the difference in XANES of K edge spectra with and without core hole is much less pronounced, see Fig. 3.5.

The results of the calculation for Co and Fe are shown on Figs. 3.6 and 3.7 (XAS in Ni is analyzed in details in Chapter 4). The agreement with experiment is good. As in case of Cu, we find that for the elements with more than half filled d band the initial state rule is more favorable, especially if one considers the integrated intensity and not just the white line peak heights. The experimentally observed fine structure is much less pronounced than the calculated one, which again suggest that a better treatment of the Debye-Waller factors and structural disorder and/or full potential (instead of muffin-tin approximation) calculations are needed. However, there is an additional discrepancy between theory and experiment, namely the calculations are not able to reproduce the observed asymmetric line shape, which is most noticeable in case of Fe. As we will see in Chapters 4 and 8, this discrepancy is most likely due to

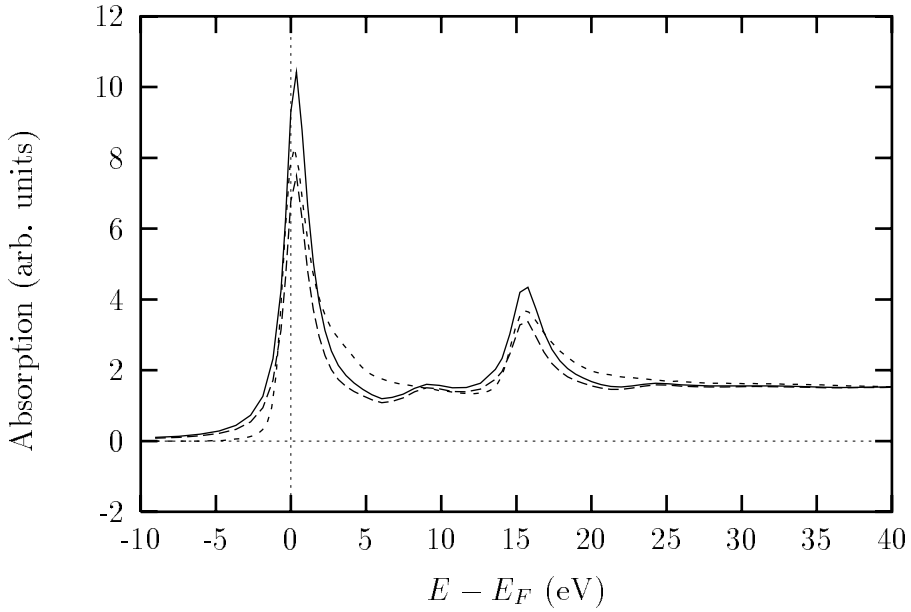

Figure 3.6: $L_{2,3}$ edge XANES of Co, solid line and long dashes represent the results of calculations done without and with a core hole respectively, short dashes is experimental data.

many-body effects such as multiplets and local field (dielectric polarization) effects.

The reasons for the failure of the final state rule are still not completely clear. One of the most often used arguments is that the screening of the core hole by valence electrons in metals is very efficient. Obviously, we are not able to resolve this problem within the independent particle picture. A very interesting observation was done by Stern and Rehr [50], who considered some many-body aspects of the near-edge structure in x-ray absorption. They used a reformulated Hartree-Fock model similar to the one of Friedel [51] and Combescot and Nozières [52]. Stern and Rehr found that, in general, the most natural single-particle state to describe the system are not the usual Hartree-Fock states but those that explicitly incorporate the exclusion principle in the transition. To satisfy the inclusion principle, the excited photoelectron states should be orthogonal to all initially occupied states and the resulting core hole orthogonal to all finally occupied states. The orthogonality requirement is satisfied

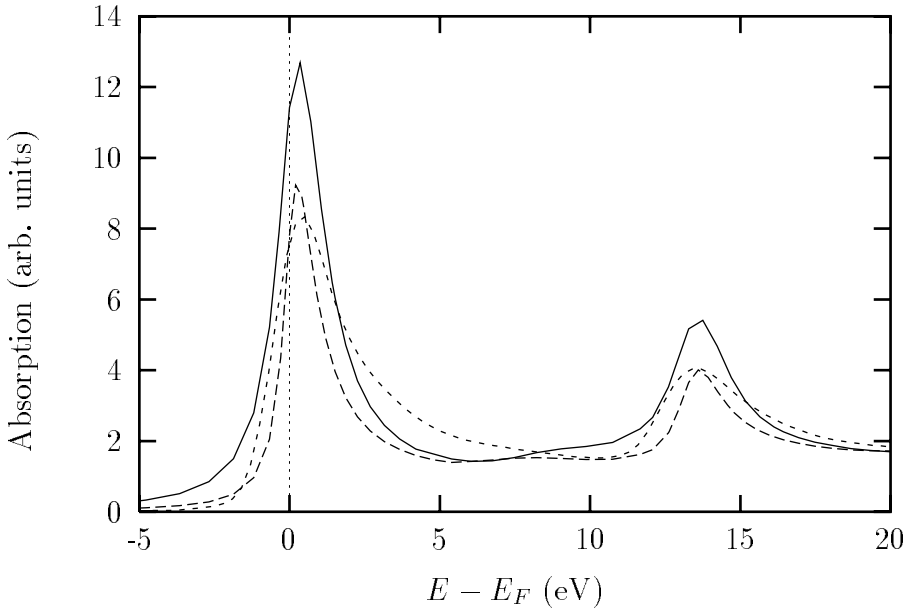

Figure 3.7: $L_{2,3}$ edge XANES of Fe, solid line and long dashes represent the results of calculations done without and with a core hole respectively, short dashes is experimental data.

by projecting out the overlap terms $\langle n|f'\rangle$:

$$|\tilde{f}'\rangle = P_{unocc}|f'\rangle \,, \tag{3.2}$$

where P_{unocc} is a projection operator

$$P_{unocc} = 1 - P_{occ} = 1 - \sum_{occ} |n\rangle\langle n| \,. \tag{3.3}$$

Here $|f'\rangle$ corresponds to the photoelectron state calculated with a core hole and $|n\rangle$ are the initially occupied (ground state) wave functions. In two limits the problem reduces to an effective single-particle problem. In case of transitions to initially empty band, one should use the local density of states of the final potential (final state rule), and $|\tilde{f}'\rangle \rightarrow |f'\rangle$. On the other hand, in case when the photoelectron completely fills that shell, the appropriate choice is the ground state density of states (initial state rule), and $|\tilde{f}'\rangle \rightarrow |f\rangle$, where $|f\rangle$ is the photoelectron state calculated with no core hole in the core level. Their theory cannot deal with the cases when the band is only

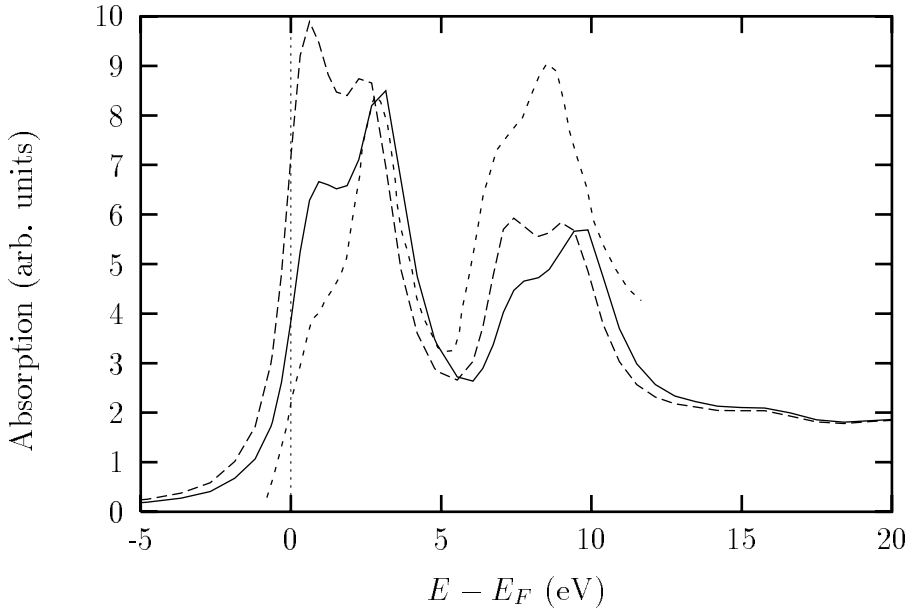

Figure 3.8: $L_{2,3}$ edge XANES of Ti, solid line and long dashes represent the results of calculations done without and with a core hole respectively, short dashes is experimental data.

partially filled (empty), but one would expect a gradual transition between the two limits.

The agreement between theory and experiment gets worse as one moves left across the periodic table toward elements with almost empty d band. Results for V and Ti are shown on Figs. 3.8 and 3.9. The experimental data are taken from [53]. The effect of a core hole becomes less dramatic for the transition metals with half filled or almost empty d band. For these elements, both initial and final state rule calculations cannot satisfactory explain experimental data, but the initial state rule still seems to be a preferable choice. Unfortunately, the available experimental data do not allow more detailed comparison between theory and experiment. Still, in case of V and Ti (and other transition metals with less than half field d band) there is an apparent need to consider many-body effects. The single-electron calculations, regardless of whether they are done using the initial or final state rule, predict the L_3/L_2 white

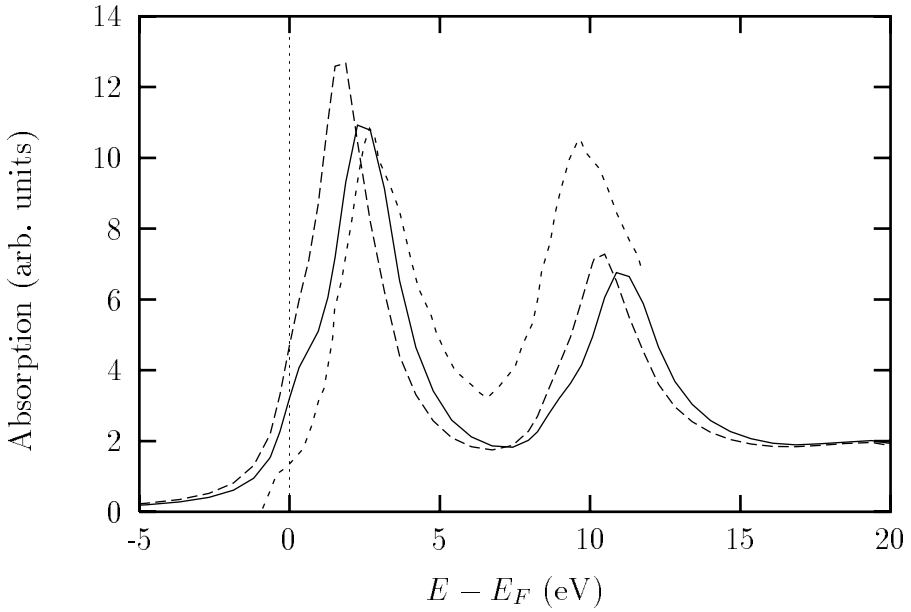

Figure 3.9: $L_{2,3}$ edge XANES of V, solid line and long dashes represent the results of calculations done without and with a core hole respectively, short dashes is experimental data.

line ratio that is close to 2:1, as expected on the basis of the $2j + 1$ degeneracy of the initial $2p$ core states. Strictly speaking, the L_3/L_2 ratio is modified due to differences in lifetime broadening of L_3 and L_2 edges and relativistic effects. However, in case of $3d$ transition metals this effects are small and cannot describe the strong deviation observed in experiment which shows that the observed L_3/L_2 ratio in these metals can be even smaller than 1:1. This problem has already been discussed in many experimental [18, 19, 53, 54] and theoretical [55, 56, 57, 58] studies. In Chapter 8 we will go beyond the independent-particle picture and address this problem by using the time-dependent local density approximation (TDLDA) formalism.

3.5 Cluster size effect and comparison with band structure codes

We also analyzed the importance of multiple scattering on the density of states and XANES. We found that the size of the cluster needed to obtain reliable results for

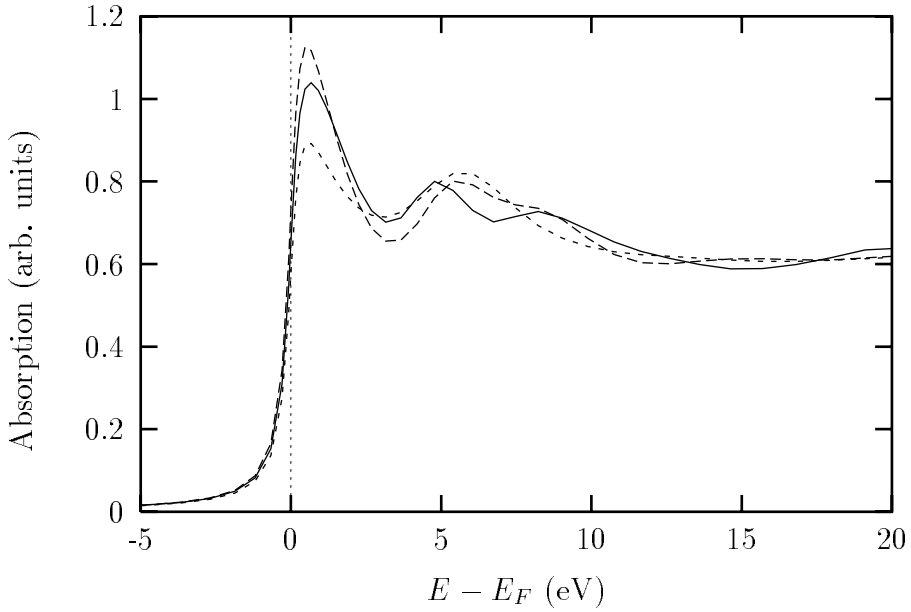

Figure 3.10: L_3 edge XANES of Cu, calculations are done for a cluster of 177 atoms (solid line), 87 atoms (dashes) and 43 atoms (dots).

the scattering potential is typically less than 40 atoms (first and second and third neighbor shells). For the density of states and XANES, a cluster of 100 atoms is usually sufficient to reproduce all major features, but a larger cluster is often needed to account for all fine details of the spectrum, see Fig. 3.10.

The results of FEFF8 are in excellent agreement with the results of full potential ground-state band structure methods [59]. In Fig. 3.11 we show the comparison for the d density of states calculated using FEFF8 and LAPW code WIEN97 [6]. Agreement between FEFF8 and WIEN97 calculations of XAS is also good [48]. Moreover, our calculations often produce better results for DOS and XANES at higher energies, where standard band-structure approaches fail due to their limitation on the number of basis states that could be taken into calculations.

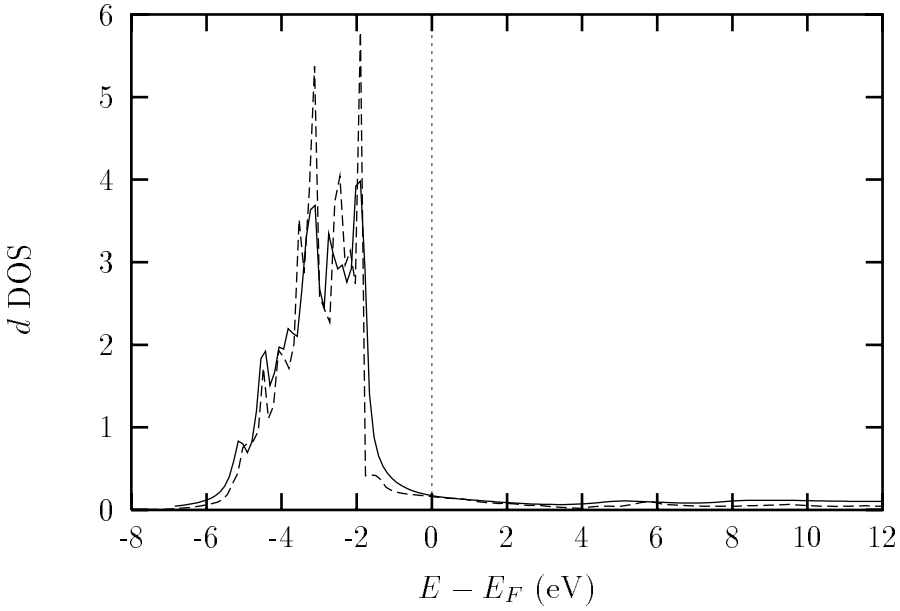

Figure 3.11: d-projected DOS in Cu calculated using FEFF8 (solid line) and LAPW code WIEN97 (dashes).

Chapter 4

INTERPRETATION OF X-RAY MAGNETIC CIRCULAR DICHROISM AND X-RAY ABSORPTION NEAR EDGE STRUCTURE IN NI

In this Chapter, we use theoretical calculations to interpret various spectral features in XANES and XMCD at the Ni $L_{2,3}$ edges [60]. Ni is a particularly instructive case for comparing theory and experiment among 3d elements, because the L_2 and L_3 edges are well separated by about 17.5 eV, the maximum separation possible for ferromagnetic 3d metals. This separation permits a detailed investigation of the region between the edges, where several interesting features are observed.

4.1 Interpretation of the experimental data: atomic multiplets vs multiple scattering

XANES and XMCD of Ni $L_{2,3}$ edges have been studied previously both for bulk Ni [61, 62, 63] and for films [64, 65, 66, 67, 68]. For example, these spectra have been used to investigate changes in electronic structure as a function of film thickness in Ni/Cu [64], Ni/Fe [65], Ni/Co/Cu [66], and Ni/Pt [67] films. Similarly, modification of the electronic structure by stepwise oxidation has been investigated [68]. Several interesting features are observed in the XMCD signal, including an extended negative plateau between the L_2 and L_3 edges, and notable satellite structures at 3 and 6 eV above the L_3 edge. However, an unambiguous interpretation of these features has been lacking. For example, it is not clear whether the shape and area of the L_3 white line in XAS is determined only by one-electron processes or whether multiplet transitions

and other many-particle excitations [69, 70, 71] also contribute to the overall intensity. To answer these questions it is important to understand the absorption cross-section in detail and to evaluate separately the contributions from single- and many-particle excitations.

Several different approaches are currently used to calculate XAS, each of which stresses different aspects of the electronic structure. Here we consider both atomic-multiplet [72, 73, 74] (AM) and real space multiple scattering (RSMS) approaches [7, 34, 75]. AM calculations generally reproduce experimental results close to the $L_{2,3}$ edges of transition metals [74]. However, the AM theory quickly becomes less reliable several eV away from the edges. For example, attempts to interpret the 6 eV satellite in terms of multiplet effects [66, 72, 73, 74] were inconclusive. Within the AM approach, the treatment of the atomic environment is greatly simplified, and usually reduced to one or more crystal field parameters determined by fitting to experiment. In addition, this approach contains only localized atomic orbitals and, therefore, fails to reproduce the XANES above about 6 eV of the edge, where the contribution from transitions to delocalized (i.e., continuum) d-states is dominant. On the other hand, the *ab initio* RSMS approach treats the atomic environment in terms of multiple-scattering without adjustable parameters, and generally gives good agreement with experiment for $3d$ transition metals, except very close to the edge. As discussed previously [69, 75, 76], the 6 eV satellite in XANES is reproduced by one-electron calculations. In particular, this peak has been attributed to a critical point in the band structure, and is therefore associated with multiple scattering. Here we reanalyze all spectral features observed in high resolution experimental data using both AM and RSMS [7] calculations, and thereby derive an interpretation that encompasses both single-electron theory and many-body multiplet effects.

In the previous Chapters we discussed the single-electron theory of x-ray absorption. Here let us start with the many-body expression for the x-ray absorption coef-

ficient:

$$\mu_j^\epsilon(E) \sim |\langle I| \sum_{i,F} \vec{\alpha}_i \cdot \vec{\epsilon}\, e^{i\vec{k}\cdot\vec{r}} |F\rangle|^2 \delta(E - E_F + E_I). \tag{4.1}$$

where $|I\rangle$ and $|F\rangle$ are many-body N particle wave functions for the initial (I) and final (F) states of the system. For an atomic system one can calculate approximate many-body states, e.g., as linear combinations of Slater determinants. For high energy continuum states, the atomic calculations are well represented with a separable approximation: i.e., the final N particle wave function $|F\rangle = |f\rangle|F'_{N-1}\rangle$ is a product of a single-electron photoelectron wave function $|f\rangle$ and an $N-1$ particle wave function $|F'\rangle$, where the prime denotes quantities in the presence of a core-hole. This approximation works well far above threshold, but ignores the effect of neighboring atoms and many-body effects. However, these problems can be corrected for by including various multiplet states and by introducing crystal fields to simulate the effect of the environment. In this work we use the AM code of de Groot [74] to treat such effects. On the other hand multi-atom, one-electron theories (e.g., band structure or RSMS) account well for the effect of the environment on the final state wave function $|f\rangle$ without any parameters, but usually neglect multiplet splitting effects.

4.2 Real space multiple scattering calculations

The spin-dependent relativistic calculations reported here are done using the real space Green's function code FEFF8 [7]. In the RSMS method the x-ray absorption coefficient μ_j^ϵ for a given edge j and polarization ϵ can be obtained from the spin-dependent, one-electron density matrix $\hat{\rho}(x, x', E) = \mathrm{Im}\, G(x', x, E)$,

$$\mu_j^\epsilon(E) \sim \langle j|\hat{\epsilon^*} \cdot \vec{r}\,' \hat{\rho}(x, x', E)\, \hat{\epsilon} \cdot \vec{r}\,|j\rangle \theta(E - E_F)\,, \tag{4.2}$$

where $|j\rangle$ is the core state, E_F is the Fermi energy, $\hat{\epsilon}$ is the x-ray polarization vector, and $x = (\vec{r}, s)$ denotes space and spin variables.

A fully relativistic theory for magnetic systems involves coupled equations [77, 78] which greatly increases the computational effort and complexity of the problem.

However, the problem can be greatly simplified by using an interpolative approach of Ankudinov and Rehr [24]. The x-ray absorption process involves two steps. First, a photoelectron is produced from a deep core level. Second, the photoelectron propagate and scatters on other atoms in a material. A relativistic approach including spin-orbit (SO) interaction is often needed for an accurate description of the first step (dipole matrix elements and core excitation energies), which depend on the structure of the inner core of atoms and on photon polarization. The second step is essentially non-relativistic in nature, even for photoelectrons of moderate kinetic energy ($\sim$1000 eV). As a results of this separation, it is possible to simplify the treatment of relativistic spin dependent XAS calculations.

The key features of the interpolative approach of Ankudinov and Rehr are: 1) a fully relativistic treatment of atomic properties and dipole matrix elements via the Dirac equation, which is solved for $j = \ell \pm 1/2$ orbitals in spin-up and -down potentials; 2) interpolation between the above four solutions of the Dirac equation via Clebsch-Gordon (CG) coefficients; 3) a non-relativistic treatment of propagation based on the spin-dependent MS expansion; 4) semi-relativistic t-matrices.

Within this approach the expression for XAS is directly analogous to the non-relativistic spin-independent form, apart from additional spin-indices:

$$\mu(\omega) = -\frac{4\pi\, c}{\omega}\mathrm{Im}\sum_{i,Js,J's'}\langle i|d^*_\epsilon|R_{Js}\rangle \qquad (4.3)$$
$$\left[-i2k_s\,\delta_{Js,J's'} + e^{i(\delta_{js}+\delta_{j's'})}G^{sc}_{Js,J's'}(\omega+\epsilon_i)\right]\langle R_{J's'}|d_\epsilon|i\rangle\theta(\omega+\epsilon_i-\mu)\,,$$

where $J = (j, m_j)$ and k_s is the wave number relative to the spin-dependent muffin tin potential. Equation 4.3 look exactly the same as the nonrelativistic MS expression given by Eq. 2.10.

As is conventional in MS theory described in Chapter 2, the Green's function $G_{Js,J's'}$ is represented in an angular momentum basis and can be separated into central and scattering parts, $G_{Js,J's'} = G^c_{Js}\delta_{Js,J's'} + e^{i(\delta_{js}+\delta_{j's'})}G^{sc}_{Js,J's'}$. The Green's function $G^{sc}_{Js,J's'}$ can be calculated using the non-relativistic quantities $G^{sc}_{Ls,L's'}$ and the Clebsh-

Gordan coefficients as follows

$$G^{sc}_{Js,J's'}(E) = \langle J|LS\rangle G^{sc}_{Ls,L's'}(E)\langle L'S'|J'\rangle \tag{4.4}$$

The propagator $G^{sc}_{Ls,L's'}$ can be calculated using MS theory described in Chapter 2, Eqs. 2.22 and 2.23 (with addition of spin indexes). In the MS expansion formula for $G^{sc}_{Ls,L's'}$, Eq. 2.22, the free propagators $G^{0}_{Ls,L_1 s}$ can be calculated non-relativistically. In the same MS expansion one can use semi-relativistic scattering t-matrices

$$\begin{aligned} t_{Ls,L's'} &= \sum_{j=\ell-1/2}^{\ell+1/2} \langle LS|J\rangle \frac{t_{js}+t_{js'}}{2} \langle J|L'S'\rangle \delta_{\ell,\ell'}\,, \\ t_{js} &= \frac{e^{2i\delta_{js}}-1}{-4\mathrm{i}\,k_s} \end{aligned} \tag{4.5}$$

This is a good approximation, since the scattering of electrons with moderate kinetic energy is dominated by the region where SO is small. The calculations of δ_{js} are based on Loucks Eq. 4-87 [79].

We note that the Ankudinov-Rehr approach used here becomes exact if either SO or spin-dependent interaction is zero. It can be proved [36] that this approach, like the coupled equation approach, is correct up to second order in perturbation theory.

The RSMS calculations here are carried out for initial (ground) state potentials, rather than with a core hole. As we discussed in Chapter 2, for 3d transition metals and systems with more than half-filled d-bands, such initial state calculations usually give better agreement with experiment than calculations done with final state potentials (with a core hole).

4.3 Results and Discussion

Fig. 4.3 shows the Ni $L_{2,3}$ XANES obtained from experiment and RSMS theory. Although the overall shape is in reasonable agreement, the amplitude discrepancies are due mostly to the approximate treatment of Debye-Waller factors in the calculations. Fig. 4.3 also shows the results of AM calculations obtained by using the AM code

of de Groot [74]. There is is an important difference between our AM calculation and those reported in [72, 73]. In [72, 73], and following papers, see e.g. [66], the ground state configuration of Ni was assumed to be a superposition of d^8, d^9 and d^{10} configurations. The relative weights were determined by fitting calculated XAS and XMCD spectra to experiment. Comparisons between theory and experiment were based on the assumption that the 6 eV satellite is due to multiplet effects. As a result, the weight of the d^8 configuration was obtained to be around 15-20%. However, if the 6 eV feature is due MS from the environment, as we would like to argue here, then a different set of the configuration weights would certainly be more appropriate. The hole count analysis of the experimental $L_{3,2}$ absorption in Ni presented in Chapters 6 and 7 shows that the atomic configuration must be much close the d^8 configuration than to any of the configurations reported in [72, 73]. Thus, we chose to perform AM calculations based a single d^8 configuration, and results are plotted in Fig. 4.3. The 3 eV satellite is clearly seen in the AM calculations, and corresponds to the asymmetric shape (or shoulder) on the white line of the of experimental XAS. Since the AM theory only takes into account contributions from localized atomic states, the absorption coefficient calculated using AM theory quickly goes to zero at higher energies.

The XMCD signal calculated by FEFF8 for a cluster of 50 atoms and measured in experiment are shown in Fig. 4.3. In Fig. 4.3 we blow up the energy scale to show the region between L_3 and L_2 absorption edges. A bigger cluster does not produce any significant changes, but for a 13 atom cluster (short dashes in Fig. 4.3) with only a single coordination shell, the 6 eV feature is missing. Ni L-shell XANES and XMCD in films has been studied in various works [64, 66]. The overall agreement between experiment and theory for XMCD is good, except that again (Fig. 4.3, 4.3) the RSMS calculations miss the 3 eV peak. From Fig. 4.3 it is clear that such a peak can arise from AM splitting of the main peak. Hence this appears to be a many-body feature which one cannot expect to obtain from broadened one-electron calculations. The

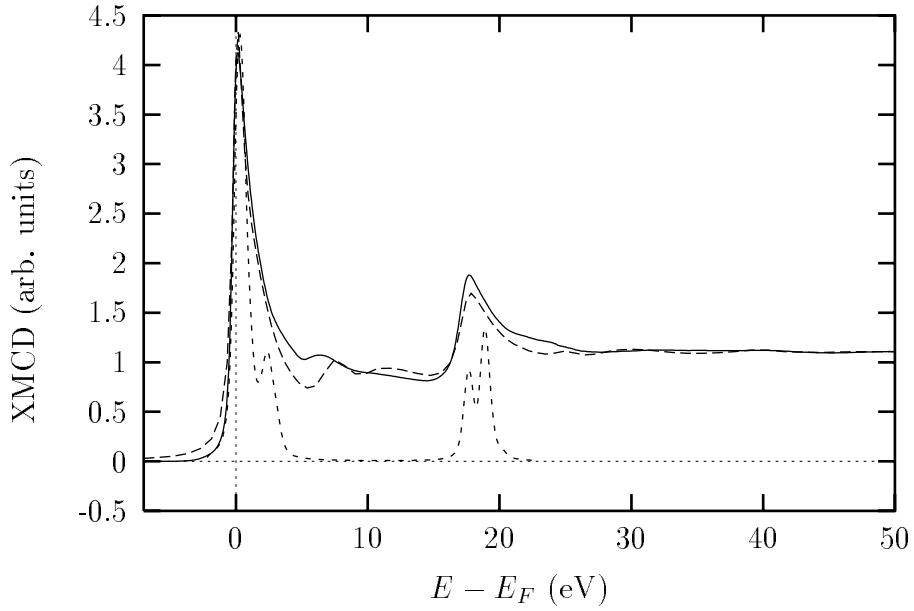

Figure 4.1: $L_{2,3}$ edge XANES in Ni, as calculated by RSMS (dashes) and AM theory (short dashes) and from experiment (solid).

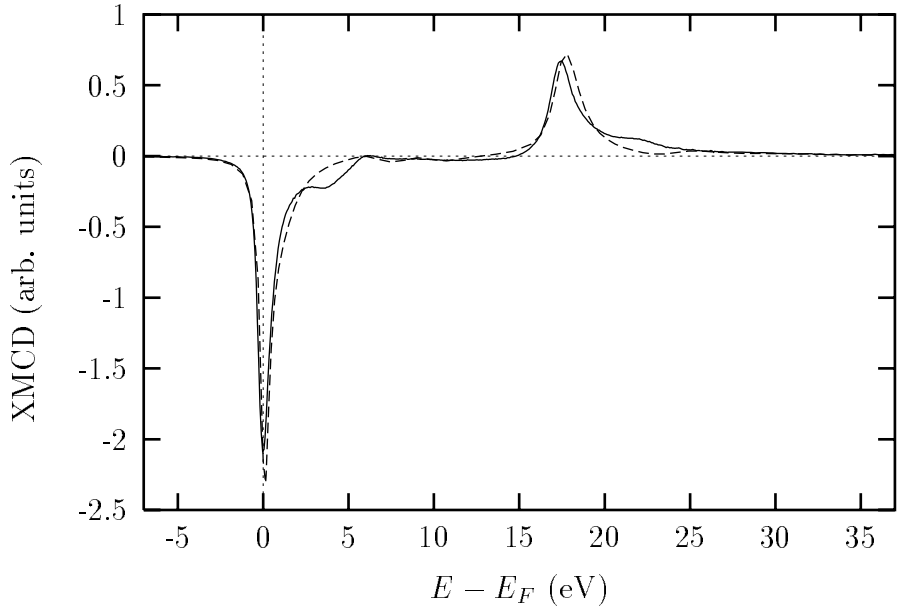

Figure 4.2: $L_{2,3}$ edge XMCD in Ni, as calculated by RSMS (dashes) and from experiment (solid).

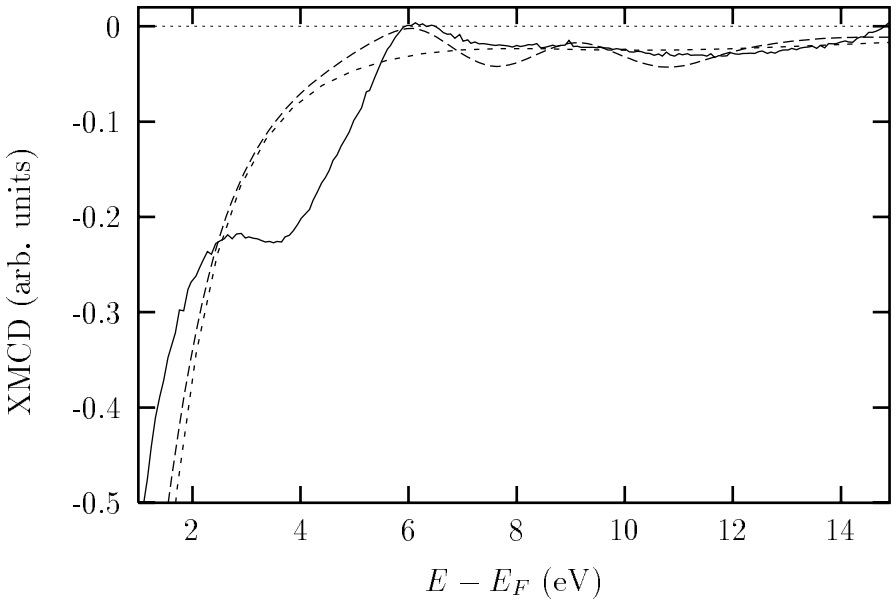

Figure 4.3: L_3 edge XMCD in Ni, as calculated by RSMS (dashes) and from experiment (solid). Also shown RSMS calculations for a small cluster of 13 atoms (short dashes).

intensity of the main peak or white line dominates the sum rules for orbital and spin moments, and hence the integrated intensity of the white line in XMCD is roughly proportional to the spin moment.

In some works, both the 3 eV and 6 eV satellites have been assigned to multiplets [66]. In this interpretation, the satellites correspond to transitions to singlet (6 eV) and triplet (3 eV) states of the final $2p^5 3d^9$ configuration, split by the core-valence exchange interaction. The singlet state cannot be reached from a triplet $3d^8$ initial state unless one allows spin-flip transitions due to the 2p spin-orbit interaction. A related investigation was conducted in case of photoemission [80]. We believe, however, that the effect of spin-flip transitions is negligible in this case, and present evidence that the 6 eV satellite is predominantly a multiple scattering effect. For the 3 eV satellite, however, the multiplet explanation is reasonable, and its presence is indicative of limitations of one-electron theory.

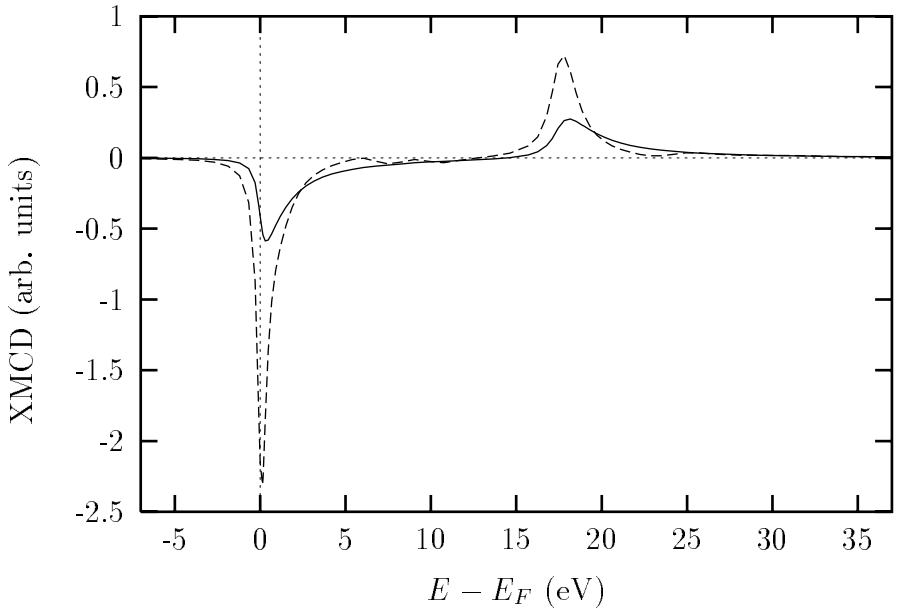

Figure 4.4: Calculated $L_{2,3}$ XMCD of Ni (dashes) and a smooth atomic background XMCD signal (solid line).

Both the 6 eV feature in XANES and the zero in the XMCD signal at about 6 eV are correctly reproduced by our RSMS calculations. Within MS theory, these features can be viewed as the effect of multiple scattering from the environment (dashes in Fig. 4.3) on top of a smooth atomic background signal (solid line). The importance of multiple scattering in magnetic L-edge EXAFS of 3d elements was previously noticed [81]. From XMCD theory the XMCD signal is the difference in XAS between spin-up and spin-down components, i.e., $\mu^+ - \mu^-$. Thus zeros in XMCD can be interpreted as the energies where the spin-up DOS is equal to spin-down DOS, while the extrema correspond to energies where the spin-up and -down DOS have the largest differences. Alternatively one can say that the XMCD signal is proportional to the derivative of the XAS, so the zeros of the XMCD correspond to peaks in the XAS.

It has been observed that the 6 eV feature disappears in case of very thin films. This observation is consistent with our interpretation, and since it results from a reduction of the multiple-scattering contribution due to an effectively reduced cluster

size (Fig. 4.3 short dashes). Thus we feel that the disappearance of the negative spin polarization at about 6 eV seen in experiment is due to spin dependent destructive interference from multiple scattering. The RSMS theory also predicts a small oscillation at about 8 eV above L_3 edge in both the XAS and XMCD due to multiple-scattering; however, experimental noise makes this feature difficult to observe conclusively.

The extended negative (positive) tail in the XMCD above L_3 (L_2) edges is well reproduced by RSMS calculations. The existence of such tails is not surprising within the derivative interpretation of XMCD. Since the atomic background absorption should become small at high energies, one expects to have smooth tails above L_3 (L_2) edges. In Fig. 4.3 it seems that the negative tail (plateau) between L_3 and L_2 edges is slightly more pronounced in experiment than in theory. However, this discrepancy might be due in part to overlap with L_2 edge, and theory allows one to disentangle these edges. The broadening of the L_2 theoretical spectrum with only the core-hole lifetime gives too big a signal in the region below the L_2 edge, and this in turn, kills the negative tail coming from L_3 edge. So instead of looking at the combined L_2 and L_3 signals, it is probably better to consider only the L_3 edge, as shown in Fig. 4.3. One sees that the theoretical XMCD signal for the L_3 edge alone clearly has a negative tail that extends up to $\sim$ 15 eV above the edge, and it is clear that this smooth signal is dominated by the atomic background contribution, see Fig. 4.3. A common explanation for the negative plateau between the L_3 and L_2 edges is the so called "diffuse magnetism" [62, 82], i.e. the contribution from delocalized s-electrons. We tested this hypothesis using RSMS calculations with only final d-states (i.e., without s-contributions), but did not see any difference within the line width in Figs. 4.3 and 4.3. This failure of the "diffuse magnetism" interpretation is perhaps not unexpected, at least for bulk systems. For bulk fcc Ni, s-states can contribute as much as 7% to the total spin moment [83]. However, the matrix element for transitions to s-states is about an order of magnitude smaller than that for transitions to d states. In addition, the matrix elements are smooth functions of energy and, as a result, the

contribution from s-states is evenly distributed in an extended energy range, and not just in a 5-10 eV interval between L_2 and L_3 edges. Therefore, we conclude that the observed negative plateau between L_3 and L_2 edges and, similarly, the extended positive tail above L_2 edge is due to transitions to spin-polarized continuum ϵd-states. Our RSMS calculations also show that the unoccupied part of the d density of states has long tails extending up to $\sim$ 15 eV, i.e. much broader than one would expect for a single atom. For this reason, AM codes cannot reproduce them, even with substantial crystal fields. Such long tails in XANES are important for an accurate application of the sum rules, since the L_3 plateau is small, but not negligible near the main L_2 peak.

4.4 Conclusions

Theoretical calculations can play an important role in the analysis of XANES and XMCD experiment, allowing one to disentangle various contributions to the experimental signal, e.g., one-electron and multi-electron features, or transitions from p to s and from p to d states. We have shown that one-electron RSMS simulations for Ni L_3 edge XMCD and XAS reproduce all spectral features in experiment, with the notable exception of the 3 eV satellite. This feature has been traced to a multiplet effect based on simulations with the AM code [74]. The main white line peak in the spectra is clearly due to transitions to the unoccupied spin-down $3d$-states. The smooth background gives rise to a smooth plateau in XMCD, which is traced to transitions to delocalized ϵd-states. The 6 eV peak is assigned to multiple scattering from the environment at intermediate range; indeed, three coordination shells are needed to simulate the peak. The zero in the XMCD signal at 6 eV is attributed to a cancelation between the central atom and multiple scattering contributions. Additional insight can be achieved by the observation that the $L_{2,3}$ XMCD is proportional to the difference in absorption between spin-up and spin-down electrons (neglecting small SO in final state). With such an interpretation one immediately expects a smooth plateau

from the central atom, and also rough proportionality of XMCD to the derivative of the XANES with energy. Although we have analyzed in detail only the XANES and XMCD for Ni, similar results are expected to hold for Co in Ni/Co films [84], and in related materials.

Chapter 5

X-RAY ABSORPTION NEAR EDGE STRUCTURE OF NI INTERMETALLIC MATERIALS

Binary intermetallic compounds that contain a transition metal and a group-III metal display interesting electronic and magnetic properties. For instance, Ni_3Al demonstrates weak itinerant ferromagnetism with $T_c = 41$ K and a very small magnetic moment [85], while Ni_3Ga is an exchange enhanced paramagnetic metal [86], and Ni_3In and NiGa are non-magnetic. Such compounds are excellent systems for studying the transition metal *d* bands, since group-III metals contribute only *s-p* states to the valence band.

While there were numerous XANES studies of bulk Ni metal and Ni thin films, XANES study of Ni intermetallic compounds, other than Ni-Al, is much less reported. The Ni L_3 near-edge structures in Ni_3Al were measured by electron-energy-loss spectroscopy (EELS) [87] and XANES [88, 89]. EELS spectra of Ni_3Al were theoretically calculated [90] by using band-structure method, but agreement with experimental data seems to be far from satisfactory. Muller et al. [91] and Chang et al. [89] used measured Ni L_3 edge white-line intensities to study charge transfer and hybridization effects in Ni_3Al. Though experimental Ni L_3-edge XANES spectra of Ni_3Al, Ni_3Ga, and NiGa have been reported previously [88], detailed theoretical analysis is still lacking. As in the case of Ni metal, several interesting features were observed in the L_3 and L_2-edge XANES spectra of these intermetallic compounds. However, a clear and detailed interpretation of those features is missing.

As we already discussed in Chapter 4, there are two different approaches used to

analyze XANES spectra of transition metals and related systems. One is based on atomic multiplet model [72, 74], and the other is based on single-electron multiple-scattering (MS) theory. In many cases, particular in photoemission experiments on Ni intermetallic compounds [92], photoemission valence band spectra are analyzed in terms of multiple particle excitations. Similarly, multiplet approach was used by Hsu et al. [93] in the case of intermetallic compounds.

In this Chapter we make a detailed comparison between the experimental and theoretical XANES spectra of Ni_3Al, Ni_3Ga, Ni_3In, and NiGa, and show that the theoretical XANES spectra of these materials can be explained within single-electron approach [94].

5.1 Calculation details

The calculations reported here were done in the absence of a core hole (the initial-state rule), i.e. with both the initial and final states represented by the ground-state wave functions. As in case of pure Ni, our calculations for $3d$ intermetallic compounds show that the initial state calculations are in better agreement with experiment than calculations done with final state potentials. A typical cluster size used in the calculation is about 170 atoms (up to the sixth shell). It was checked that doing full MS calculation for a larger cluster does not produce any significant changes in the absorption spectra. Transitions to both d and s states are included. The lattice constants of these materials used in the calculation are given in the third column in 5.1, along with their crystal structure. Ni_3Al, Ni_3Ga, and Ni_3In have the cubic $L1_2$ structure isotypic with Cu_3Au, NiGa has the B2 structure isotypic with CsCl [95]. It was reported [96] that Ni_3In has the ordered DO_{19} structure isotypic with Ni_3Sn. However, the XANES spectrum of Ni_3In calculated using this latter structure results in much worse agreement with the experimental spectrum than using the cubic $L1_2$ structure for Ni_3In.

Table 5.1: Crystal structure and lattice constant for Ni3Al, Ni3Ga, Ni3In, and NiGa

material	crystal	a(Å)
Ni_3Al	$L1_2$	3.568
Ni_3Ga	$L1_3$	3.576
Ni_3In	$L1_2$	3.75
NiGa	B2	2.895

5.2 Comparison with experiment and discussions

The experimental and theoretical Ni $L_{2,3}$ XANES spectra for Ni_3AI, Ni_3Ga, Ni_3In, and NiGa are displayed in Figs. 5.1- 5.4 in which the zero energy corresponds to the Fermi level of the respective Ni L_3 absorption edge. The experimental data were normalized to theory in the region 10 - 20 eV above the Ni L_2 edge.

Overall, we find a good agreement between theory and experiment. With exception of NiGa, all major features of the absorption coefficients, as well as white-line positions and intensities, are well reproduced. Small discrepancies in peak positions and intensities might be due to approximate treatment of Debye-Waller factors, or due to use of muffin-tin approximation in calculations of the scattering potentials. We note that in our calculations, most of the features observed in XANES spectra are reproduced by single-electron MS calculations. For example, the theoretical XANES spectrum for Ni_3Al well reproduces the three experimental peaks at approximately 4, 7, and 9.5 eV above the Ni L_3-edge white line, and the peak at 3.6 eV above the Ni L_2 edge white line. The same features are present in the calculated XANES spectra for Ni_3Ga and Ni_3In, though less pronounced and in less agreement with the experimental data for the peak positions. Thus, the MS single electron theory is successful in calculating the XANES spectra of intermetallic compounds. We note that the double-peak structure found for NiAl [87, 90] is not observed in NiGa. We also note

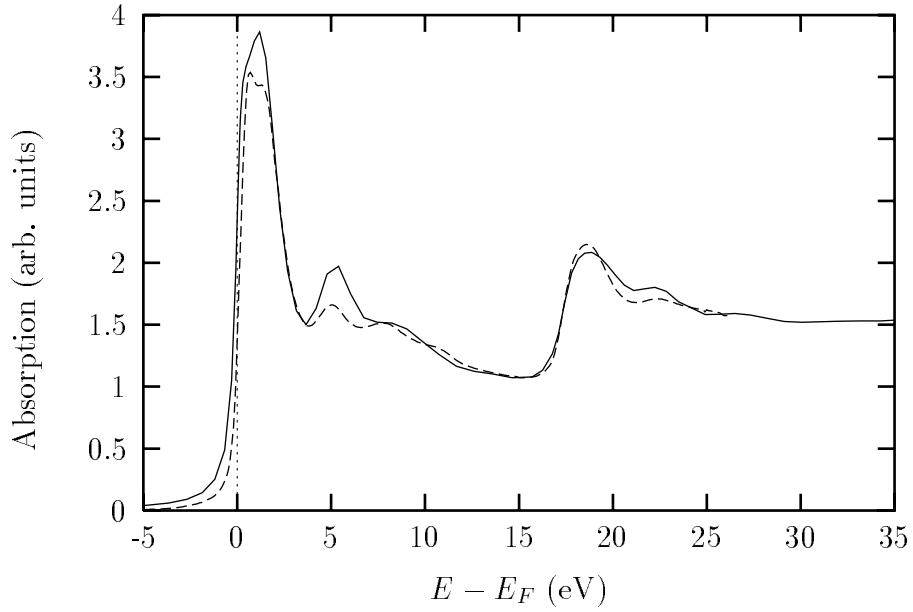

Figure 5.1: $L_{2,3}$ edge XANES of Ni_3Al, solid line a represent the results of calculations, long dashes is experimental data.

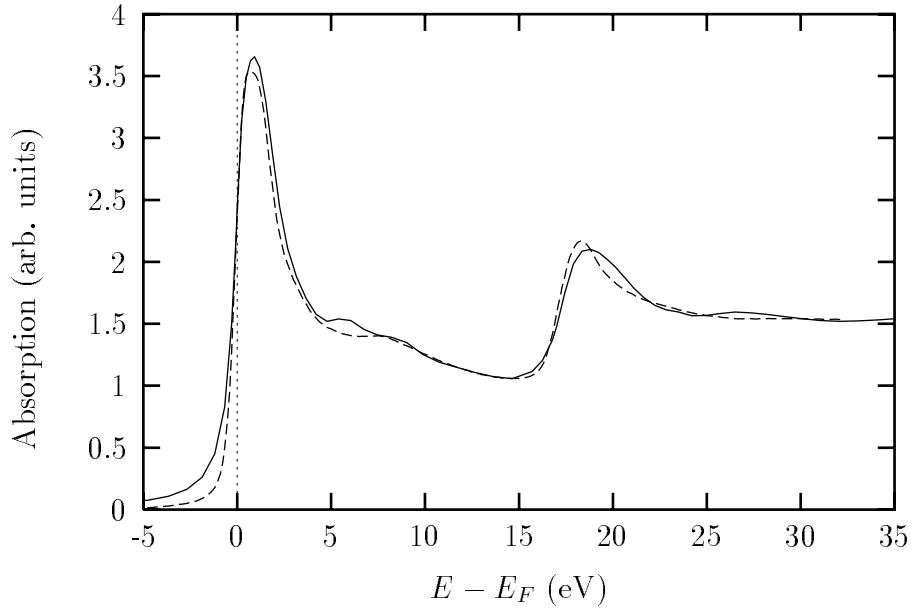

Figure 5.2: $L_{2,3}$ edge XANES of Ni_3Ga, solid line a represent the results of calculations, long dashes is experimental data.

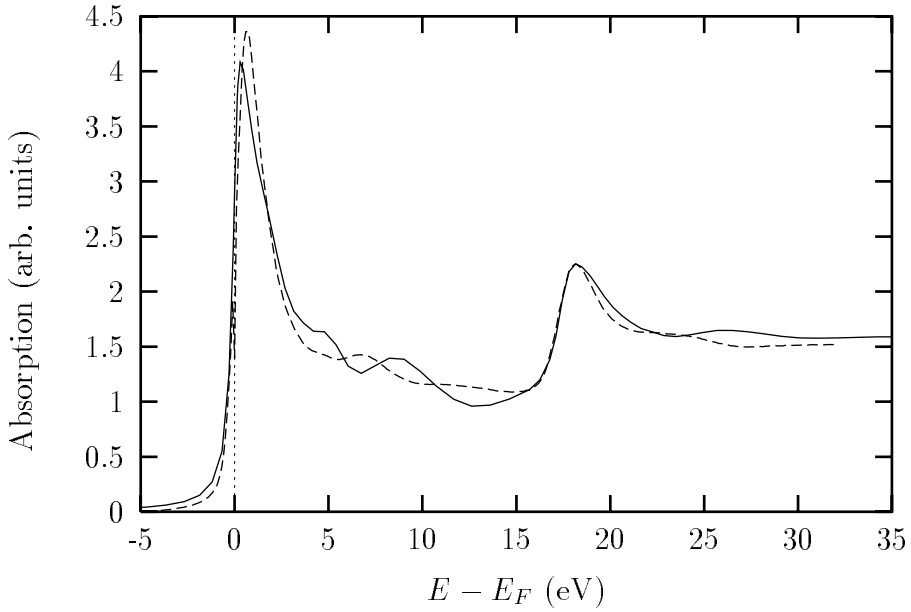

Figure 5.3: $L_{2,3}$ edge XANES of Ni_3In, solid line a represent the results of calculations, long dashes is experimental data.

that the theoretically calculated $\mu(E)$ of NiGa disagrees with experimental XANES data. The approximation that we use in treatment of structural disorder may not be adequate for the NiGa sample, which was reported to have a high concentration of anti-structure defects [93]. Anti-structure defects reduce MS contribution to the absorption coefficient. As a result, the experimental XANES spectrum for NiGa is in better agreement with the smooth atomic background absorption $\mu_0(E)$ than with $\mu(E)$, see Fig. 5.4. However, both theoretical spectra underestimate the Ni L_3 edge white-line intensity for NiGa by roughly 20%.

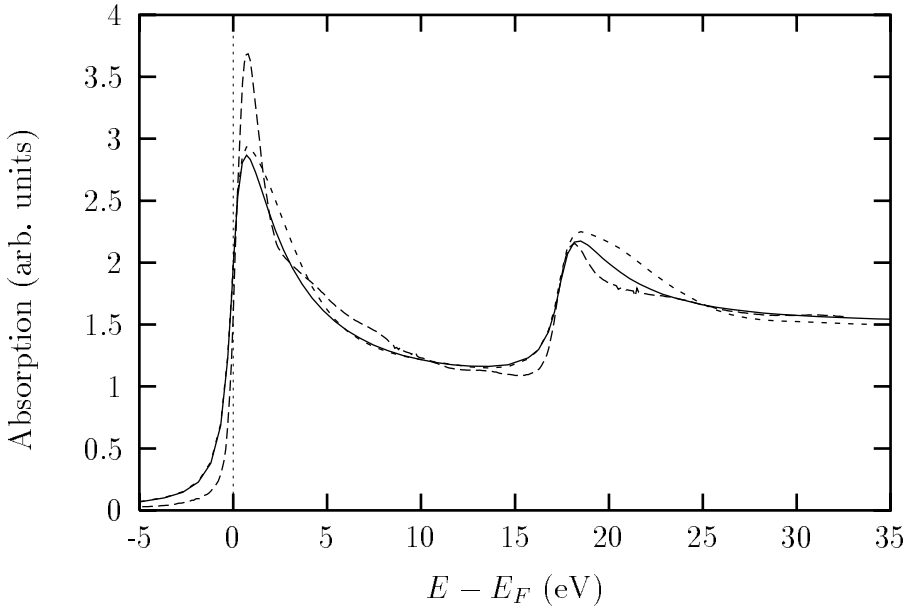

Figure 5.4: $L_{2,3}$ edge XANES of NiGa, solid line and short dashes represent calculated smooth background absorption $\mu_0(E)$ and full absorption $\mu(E)$ respectively, long dashes is experimental data.

Chapter 6

NORMALIZATION AND CONVERGENCE OF X-RAY ABSORPTION SUM RULES

X-ray absorption (XAS) and related spectroscopies are powerful tools for studying electronic and magnetic properties of solids. For example, x-ray magnetic circular dichroism (XMCD) and x-ray linear dichroism (XLD) are used for studies of magnetic properties ranging from magnetic anisotropy [13] to the exchange interaction [97, 98, 99]. The XMCD and XLD signals are directly related to the spin and orbital polarization of the final state and have unique element specific properties. Several sum rules that relate integrated XAS intensities to properties such as spin and orbital magnetic moments have been derived, [23, 75, 100, 101] which have attracted considerable interest [62, 63, 102, 103, 104, 105, 106]. In principle, these sum rules provide a way of determining these properties from experiment – information often hard to obtain with other techniques.

However, current methods for applying the sum rules have a number of theoretical and experimental difficulties which limit their accuracy and utility [102, 103, 104]. These include the problems of hole-count normalization and the difficulty of subtracting delocalized states. In particular, one of the problems with the usual approach for applying the sum rules to experiment lies in the crude *ad hoc* modeling the delocalized background contribution to the XAS by step-functions [62, 63, 105, 106] to determine hole counts, which can introduce uncontrolled errors in the analysis. In this approach the integrated intensity of an appropriate linear combination of XAS signals gives, after subtracting this background, the ratio of a particular operator expectation value

to the number of holes N_h, (e.g., $\langle S_z \rangle / N_h$ and $\langle L_z \rangle / N_h$). Thus to obtain results for spin $\langle S_z \rangle$ and orbital moments $\langle L_z \rangle$, one needs *a priori* the value of N_h. This number $N_h = 2(2l+1) - N_l$, where N_l is the number of occupied states of angular momentum l, is typically taken from independent theoretical calculations or measurements on model systems, and hence contains various systematic errors [107, 108]. Other difficulties are the use of a finite cutoff energy for the integration and the effect of core-hole and many-body effects.

In this Chapter, we introduce a quantitative procedure which overcomes most of the above difficulties, and simplifies the application of the sum rules to extract physical quantities from experiment [14]. Our approach to this inverse problem is based on a generalization of relations between XAS spectra and electronic structure, and yields analogous relations between the spectral densities of various operators and linear combinations of XAS spectra, together with additional steps to normalize the spectra and ensure convergence. These relations are calculated here using the *ab initio* real space Green's function code FEFF8, [7] which permits simultaneous, self-consistent calculations of both XAS and electronic structure. Tests show that our method is accurate to within a few percent, while the standard approach, even for an ideal one-electron test case, can significantly overestimate spin and orbital moments.

6.1 Relation between XAS and DOS

The basic idea behind our approach comes from the well known relations between XAS $\mu(E)$ and angular momentum projected density of states (LDOS) $\rho(E)$, [91, 109]

$$\rho(E) = \gamma(E)\,\mu(E)\,, \tag{6.1}$$

where $\gamma(E)$ is a smoothly varying function

$$\gamma(E) = \frac{\rho_0(E)}{\mu_0(E)}\,. \tag{6.2}$$

This relation follows from the fact that both $\mu(E)$ and $\rho(E)$ are matrix elements of the same one-body density operator $\hat{\rho}(E) = (-1/\pi)\mathrm{Im}\, G(E)$, where $G(E) = 1/(E - H - \Sigma)$ is the single particle Green's function operator, H is the final state Hamiltonian, and Σ the electron self-energy which implicitly contains most of the relevant many-body effects in our effective one-particle formalism. To determine the ratio $\gamma(E)$, we note that multiple scattering (MS) theory [7] yields analogous relations for the XAS and the LDOS,

$$\begin{aligned} \mu(E) &= \mu_0(E)[1 + \chi(E)]\,, \\ \rho(E) &= \rho_0(E)[1 + \chi(E)]\,. \end{aligned} \tag{6.3}$$

Here $\mu_0(E)$ and $\rho_0(E)$ are the smoothly varying (embedded) atomic contributions [30], while $\chi(E)$ is the fine structure or XAFS due to MS from the environment. Thus, provided the LDOS is calculated with the same potential as for XAS, the fine structure $[1+\chi(E)]$ in Eq. 6.3 cancels in the ratio, yielding the expression in Eq. 6.1 with $\gamma(E)$ given by Eq. 6.2. This proviso cannot be taken for granted due to core-hole and many-body effects. For example, the XAS naturally includes final state broadening due to core hole lifetime and photoelectron self energy shifts as well as a broadened Fermi factor, which are unavoidable in experiment. Another complication arises from the difference between the initial (ground state) and final state Hamiltonians, due to the creation of a screened core hole in the XAS process [16, 50, 58]. It has even been argued that such many-body effects can make the sum rules, as originally derived, questionable [58]. However, since $\gamma(E)$ is smooth, these effects may be expected to have negligible effects on integrated quantities, thus preserving the generality of the sum rules as originally derived. As a fully quantitative treatment of core-hole effects on XAS is not yet developed, calculations are typically carried out in two limits, namely for static initial and final state potentials. Here the calculations are done using initial state, see Chapters 3, 4. In any case, these additional many body effects can be largely simulated by replacing Eq. 6.1 with a convolution $\mu = A * \rho$ where A

represents a quasi-particle spectral density. As a result, the broadened LDOS $\rho(E)$ obtained from XAS by Eq. 6.1 differs somewhat from the ground state LDOS, which contains no self-energy or core-hole effects at all. Moreover, it may be possible to obtain an estimate for $\rho(E)$ closer to the ground state LDOS, e.g., by using the ground state function $\rho_0(E)$ in the ratio $\gamma(E)$, since the effect of the core-hole on scattering is small, i.e., $\chi' \approx \chi$, where the prime denotes quantities calculated with a core-hole.

Unlike the LDOS or the XAS, which both contain XAFS, the smooth *atomic* ratio $\gamma(E)$, is a local quantity which is more transferable and hence can be accurately calculated theoretically even for complex systems, for which band structure calculations are not routinely available. For this purpose we use the FEFF8 code [7], which permits quantitative calculations of XAS up to very high energies (of order 1000 eV above threshold). In Fig. 6.1 we show the ratio $\gamma(E)$ and smoothly varying atomic contributions $\rho_0(E)$ and $\mu_0(E)$. To show the similarity between XANES and DOS, in Fig. 6.1 we plot $\mu_0(E)$ calculated without the Fermi function cutoff $\theta(E - E_F)$. It is interesting to note that the variation of $\gamma(E)$ comes from the energy dependence in the radial states R_l and is independent of the normalization of R_l or atomic-XAFS effects [30]. To see this, note that $\gamma(E) \propto |M|^2/N$ depends on the ratio of the integrals $|M(E)|^2 = |\int dr \psi_c^*(r) r R_l(r,E)|^2$, $\psi_c(r)$ being the core state wave function, and $N(E) = \int dr |R_l(r,E)|^2$. Since each is bilinear in radial wave function $R_l(r,E)$, $\gamma(E)$ is independent of normalization, even though R_l can exhibit strong peaks due to the localized d-bands, etc. Analysis shows that the energy dependence comes from the difference in the effective range of integration. The integral for M is essentially cutoff by the radius of the core state, which is of order $1/Z$ where Z is the effective nuclear charge. However, the integral for $N(E)$ extends to the Norman (or Seitz) radius R_N, defined by overall charge neutrality of the embedded atom. As a result $N(E)$ and hence the embedded atomic LDOS $\rho(E)$ acquires a weak oscillatory behavior of the form $\sin(2kR_N - l\pi + 2\delta_l))/2kR_N$ (see Fig. 6.1), due to the oscillatory behavior of

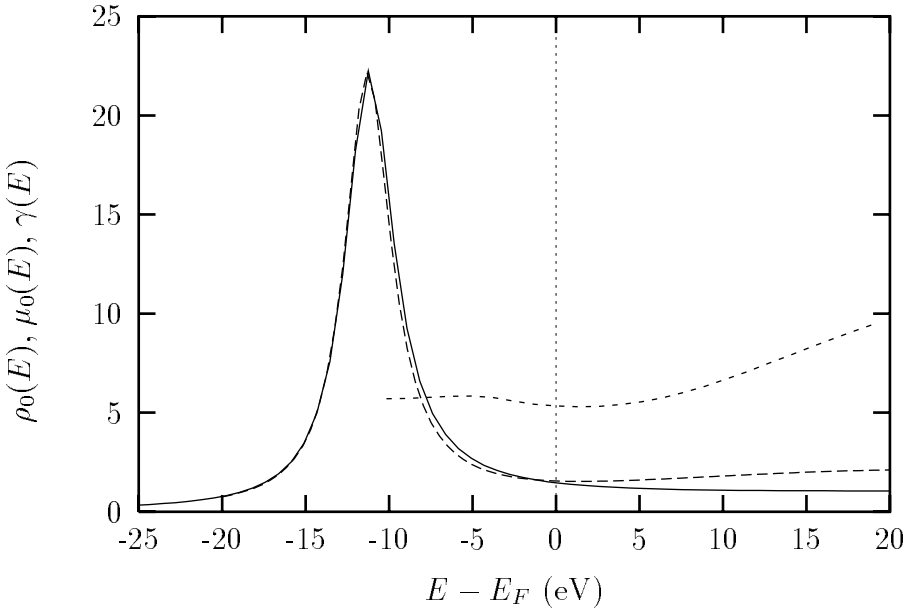

Figure 6.1: Smoothly varying (embedded) atomic contributions $\mu_0(E)$ (solid line) and $\rho_0(E)$ (dashes). Also shown is the atomic-like ratio $\gamma(E)$ (short dashes).

$R_l(r)$ near R_N [30].

The agreement between theory and experiment in the extended energy region permits an accurate normalization of experimental data from theoretical spectra. This is hard to do with conventional quantum chemistry or band-structure electronic structure codes, which are typically limited to 30-50 eV above threshold. Then from Eq. 6.1, one extracts the normalized unoccupied LDOS. This method has the advantages over the usual approach in that it does not involve either a separation into localized and delocalized parts or an integration with an arbitrary cutoff. The basic idea is illustrated for the L_3 edge of fcc Cu in Fig. 6.2, where the experimental L_3 XAS multiplied by the theoretical $\gamma(E)$ function calculated by FEFF8, is transformed into the normalized, unoccupied dDOS. For comparison, Fig. 6.2 also shows the ground state dDOS for a cluster of about 200 atoms calculated with initial state potentials. The good agreement between these results above the Fermi energy demonstrates that our procedure is justified. As anticipated, the discrepancies are due to final state

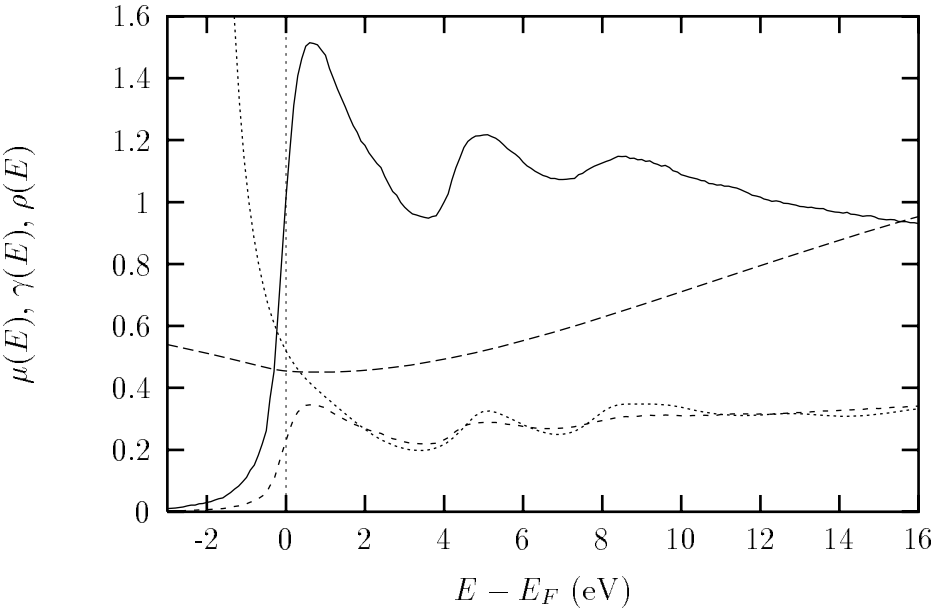

Figure 6.2: dDOS (short dashes) for fcc Cu obtained from the experimental L_3 absorption spectrum (solid line) by multiplying μ by the theoretical $\gamma(E)$ function (dashes), and for comparison the theoretical ground state dDOS (dots)

broadening effects and Debye-Waller factors.

6.2 Magnetic XAS and sum rules

We now generalize this basic idea to physical quantities in magnetic XAS that can be obtained from the spin-dependent one-electron density matrix $\hat{\rho}(x, x', E)$, where $x = (\vec{r}, s)$ denotes space and spin variables. For example, the x-ray absorption coefficient μ_j^ϵ for a given edge $j = K, L_1, L_2, \ldots$ and polarization ϵ is

$$\mu_j^\epsilon(E) = C\langle j|\hat{\epsilon^*} \cdot \vec{r}\,' \,\hat{\rho}(x', x, E)\,\hat{\epsilon} \cdot \vec{r}\,|j\rangle\theta(E - E_F)\,, \tag{6.4}$$

where C is a constant, $|j\rangle$ is the core state, E_F the Fermi energy, and $\hat{\epsilon}$ the x-ray polarization vector. Similarly, by applying the XAS sum rules, the ground state expectation values of various one-electron operators $\langle\hat{O}\rangle$, e.g., $\langle S_z\rangle$ or $\langle L_z\rangle$, can be

calculated in terms of $\hat{\rho}$,

$$\langle \hat{O} \rangle = \int_{-\infty}^{E_F} dE \ \mathrm{Tr}\, \hat{O}\hat{\rho} \ . \tag{6.5}$$

From MS theory the density operator $\hat{\rho}(x', x, E)$ can be separated into central atom and scattering terms and, in the LS representation, is

$$\begin{aligned} \hat{\rho}(x', x, E) &= \sum_{L,L'} R_{L's'}(r', E) \\ \times \quad & [\delta_{L's',Ls} + \chi_{L's',Ls}(E)] \bar{R}_{Ls}(r, E) \ . \end{aligned} \tag{6.6}$$

Here $L = (l, m)$, $R_L(r, E) = i^l R_l(r, E) Y_l^m(\hat{r})$ and $\bar{R}_L = i^{-l} R_l(r, E) Y_l^{m*}(\hat{r})$ are regular solutions of Schrödinger (Dirac) equation. It usually suffices to retain only $l = l_c + 1$ transitions (l_c being the initial core state orbital momentum), as the $l = l_c - 1$ transition is much weaker. In the sum rules of interest here, three linear combinations of polarized absorption measurements, defined respectively as $\mu_j^\alpha(E)$, play an important role: the polarization average $\mu_j^{avg} \equiv \frac{1}{3}\Sigma_\epsilon \mu_j^\epsilon$; the XMCD signal $\mu_j^{xmcd} \equiv \mu_j^1 - \mu_j^{-1}$; and the linear dichroic (XLD) signal $\mu_j^{xld} \equiv (\mu_j^1 - 2\mu_j^0 + \mu_j^{-1})/2$. If the trace of an operator over a complete LS shell is zero, one can change the limits of integration in Eq. 6.5 to $[E_F, \infty]$. In such cases (e.g., for S_z), one can obtain ground state expectation values from unoccupied spectra. These absorption coefficients are each associated with a corresponding set of operators $\hat{O}_j^\alpha$ (Table 6.1) and have similar decompositions in terms of central atom and scattering parts as follows

$$\mu_j^\alpha(E) = \sum_{ss'} \mu_0^{ss'}(E) \sum_{l,m,m'} [\delta_{Ls,L's'} + \chi_{Ls,L's'}] O^{j\alpha}_{Ls,L's'} \tag{6.7}$$

$$\langle O_j^\alpha \rangle = \int_{E_F}^{\infty} dE \sum_{ss'} \rho_0^{ss'}(E) \sum_{l,m,m'} [\delta_{Ls,L's'} + \chi_{Ls,L's'}] O^{j\alpha}_{Ls,L's'} \ , \tag{6.8}$$

where the expectation values $O^{j\alpha}_{Ls,L's'} = \langle LS|\hat{O}_j^\alpha|L'S'\rangle$ [23]. Thus the polarization average data contains information about $\hat{N}_h$ and $\vec{L} \cdot \vec{S}$; XMCD, the orbital and spin moments; and XLD, the quadrupole moment $\hat{Q}_{zz}$ and a linear combination of two other operators $\hat{R}_{zz}$ and $\hat{P}_{zz}$ [110].

Table 6.1: Operators $\hat{O}_j^\alpha$ for $K - N_5$ edges: $\hat{N}_h = 2(2l+1) - \sum_{m_l,m_s} |lm_l, m_s\rangle\langle lm_l, m_s|$ $\hat{Q}_{zz} = \frac{1}{2}[3L_z^2 - l(l+1)]$; $\hat{X}_{zz} = (2l^2 - 3l + 1)\hat{P}_{zz} + 6\hat{R}_{zz}$; $\hat{P}_{zz} = \frac{1}{2}(3L_zS_z - \vec{L}\cdot\vec{S})$; $\hat{R}_{zz} = \frac{1}{4}[5L_z\vec{L}\cdot\vec{S}L_z - [l(l+1)-2]\ \vec{L}\cdot\vec{S} - [2l(l+1)+1]L_zS_z]$.

$\alpha =$	avg	$xmcd$	xld
KL_1M_1	$\hat{N}_h$	$-3L_z$	$-3\hat{Q}_{zz}$
L_2M_2	$\hat{N}_h + \vec{L}\cdot\vec{S}$	$-\frac{3}{2}L_z + 2S_z + 7T_z$	$-\frac{1}{2}\hat{Q}_{zz} + \frac{1}{5}\hat{X}_{zz}$
L_3M_3	$\hat{N}_h - \frac{1}{2}\vec{L}\cdot\vec{S}$	$-\frac{3}{2}L_z - S_z - \frac{7}{2}T_z$	$-\frac{1}{2}\hat{Q}_{zz} - \frac{1}{10}\hat{X}_{zz}$
M_4N_4	$\hat{N}_h + \frac{2}{3}\vec{L}\cdot\vec{S}$	$-L_z + 4S_z + 12T_z$	$-\frac{1}{5}\hat{Q}_{zz} - \frac{1}{25}\hat{X}_{zz}$
M_5N_5	$\hat{N}_h - \frac{4}{9}\vec{L}\cdot\vec{S}$	$-L_z - \frac{4}{3}S_z - 4T_z$	$-\frac{1}{5}\hat{Q}_{zz} + \frac{2}{75}\hat{X}_{zz}$

Now, by making the reasonable approximation that the atomic ratios have negligible dependence on spin, we obtain linear relations connecting the various sum rules with polarization dependent XAS, i.e.,

$$\langle \hat{O}_j^\alpha \rangle \cong \int_{E_F}^{\infty} dE\ \gamma_j(E)\mu_j^\alpha(E)\ . \tag{6.9}$$

This approximation is justified because the ratios $\gamma_j(E)$ are smooth (Fig. 6.1), and values of exchange splittings are relatively small.

There are, however, a few minor technical difficulties in applying this procedure. One complication is due to the spin-orbit interaction [78, 111]: transitions to both $d_{5/2}$ and $d_{3/2}$ states are allowed at the L_3 edge, but only to $d_{3/2}$ states at the L_2 edge. This complication can be avoided, for purposes of comparing theory to experiment, by assuming that the final state wave function is purely of $d_{5/2}$ character when calculating ρ_0 for the L_3 edge; theoretical tests show that this approximation gives negligible error. Second, since it is impractical to remove final state broadening from XAS, its effect is accounted for simply by calculating both ρ_0 and μ_0 including such broadening. This is done by Lorentzian convolutions of the XAS and LDOS with $L[f(E)] =$

$\int_{E_F}^{\infty} dE'\, f(E')(\Gamma/\pi)/[(E-E')^2+\Gamma^2]$. Thus we obtain as a generalization of $\gamma = \rho_0/\mu_0$,

$$\gamma_j(E) = \frac{L[\rho_{j'0}(E)]}{L[\mu_0(E)]} \frac{\int_{V_{int}}^{E_F} dE\, \rho_0(E)}{\int_{V_{int}}^{E_F} dE\, \rho_{j'0}(E)}, \tag{6.10}$$

where V_{int} is the interstitial potential, and $\rho_{j'0}$ is calculated with R_l in Eq. 6.6 for a fixed $j' = j + 1 = l \pm 1/2$. The integral factors in Eq. 6.10 correct for small spin-orbit effects on ρ_0. Thus the broadened, unoccupied LDOS is obtained from XAS experiment by using Eq. 6.1 with $\gamma_j(E)$ given by Eq. 6.10. Finally an additional correction [102, 103, 104], should be added to correct for a finite cutoff E_c instead of ∞ in Eq. 6.9. This correction, e.g. for S_z, arises for finite exchange splitting $V_x = V_\uparrow - V_\downarrow$ and finite LDOS ρ_0, and is $\Delta S_z \approx (1/2)\rho_0 V_x$. Consider for example the spin density $S(E) = 1/2[\rho_\uparrow(E) - \rho_\downarrow(E)]$. With a finite cutoff E_c, $\int_{-\infty}^{E_F} S(E)dE \neq -\int_{E_F}^{E_c} S(E)dE$. The reason for this can be understood in the rigid band model: $\rho^\uparrow(E) = \rho_\downarrow(E + V_x)$. Thus the spin up DOS is basically the spin-down DOS shifted toward higher energies by V_x. Since the DOS becomes constant ρ_0 at high energies, one obtains

$$\int_{-\infty}^{E_F} S(E)dE \approx -\int_{E_F}^{E_c} S(E)dE + \frac{1}{2}\rho_0 V_x \tag{6.11}$$

However, at high energies $V_x \to 0$, and hence our infinite integration range sum rules apply without such a correction. With a cutoff below 100 eV this correction is typically small, about 2-3 % for spin and less than 1% for orbital moment, but can be estimated and taken into account.

Our final procedure is summarized as follows:

1) Obtain experimental μ_j^α signals.

2) Use calculated $\mu_0(E)$ to match threshold and normalize experiment to the theoretical $\mu_0(E)$ at about 50 eV above E_F. Then transform the μ_j^α into DOS units with calculated $\gamma_j(E)$.

3) Obtain expectation values $\langle \hat{O}_j^\alpha \rangle$ from the integrals in Eq. 6.9. Then, combine $\langle \hat{O}_j^\alpha \rangle$ to obtain values of $\langle S_z \rangle$, and $\langle L_z \rangle$, $\langle \hat{Q}_{zz} \rangle$, etc. (Table 6.1).

4) Add corrections for a finite cutoff E_c, if needed.

For example, from normalized XMCD at L_2 and L_3 edges, one obtains

$$\langle S_z \rangle + \frac{7}{2}\langle T_z \rangle = -\frac{1}{3}[\langle \hat{O}^{xmcd}_{L_3} \rangle - \langle \hat{O}^{xmcd}_{L_2} \rangle] \tag{6.12}$$

and

$$\langle L_z \rangle = -\frac{2}{9}[2\langle \hat{O}^{xmcd}_{L_3} \rangle + \langle \hat{O}^{xmcd}_{L_2} \rangle] \tag{6.13}$$

Note that the factor of 2 in front of $\langle \hat{O}^{xmcd}_{L_3} \rangle$ is due to our normalization convention for XAS and the operators in Table 6.1. For μ_j^{avg} it may be difficult to use steps 3) and 4), due to the slow decay of XAS with energy since $\mathrm{Tr}\,\hat{N}_h \neq 0$. This problem will be addressed in Chapter 7. Note that the spin sum rule gives a linear combination of $\langle S_z \rangle$ and $\langle T_z \rangle$. The value of $\langle T_z \rangle$ is small for bulk materials, but may be large for films. Thus one may also need theoretical simulations for $\langle S_z \rangle$ and $\langle T_z \rangle$ to separate the two contributions.

6.3 Theoretical tests

To verify our procedure for XMCD we carried out a purely theoretical test for Ni. Applying the standard approach [24], we used the same ground state density matrix $\hat{\rho}$ to calculate simultaneously $\langle S_z \rangle$, $\langle L_z \rangle$, $\langle T_z \rangle$ and μ^{xmcd}. Then we applied the above procedure to the calculated XMCD spectrum (L_3 and L_2 separated). We obtain very good agreement, with only about 1% error for $\langle S_z \rangle$ and 3% error for $\langle L_z \rangle$ between the full calculation and our procedure. We find, however, that without edge separation, the value of $\langle S_z \rangle$ with our approach would be underestimated by about 10%. Thus, when edge separation is not or cannot be made, one can use this error estimate to correct the results. We also compared the usual step-function background subtraction procedure [62, 105, 63] to normalize the XMCD spectra and obtained results higher by about 10% for $\langle S_z \rangle$, and $\langle L_z \rangle$. These results show that the standard sum-rule procedure overestimates the contribution from delocalized states which, in turn, yields significant overestimates of spin and orbital moments. Since this test was carried out

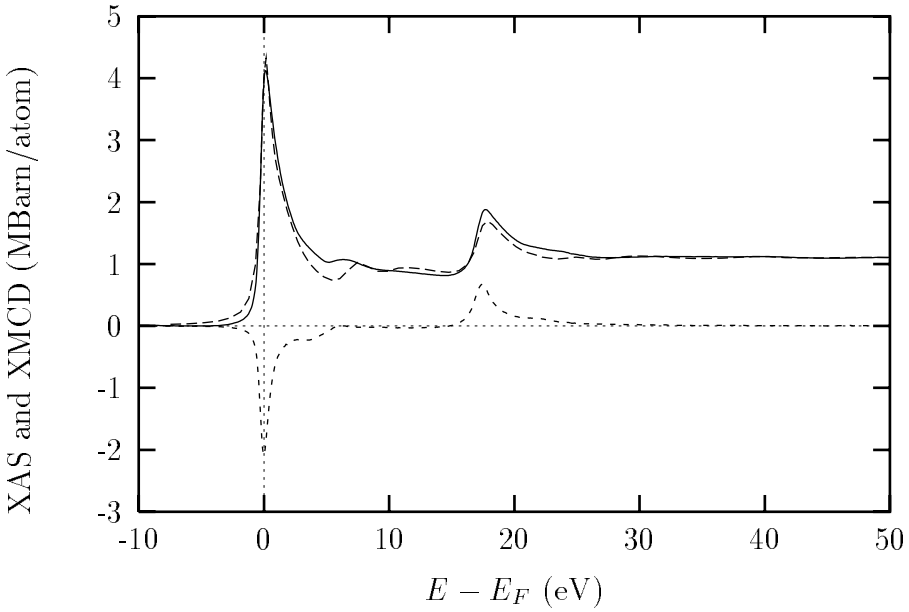

Figure 6.3: Experimental (solid line) and calculated (dashes) $L_{3,2}$ absorption spectrum μ^{avg} for Ni from FEFF8, and experimental XMCD spectrum μ^{xmcd} (dots)

for one-electron calculations, for which many-body corrections are not in doubt, the results imply that the standard procedure leads to larger errors than the approach proposed in the present paper.

6.4 Application to experimental data

Finally we apply our method to obtain spin and orbital moments from polarized XAS experiment for Ni, Co and Fe [112]. In Fig. 6.3 we plot both experimental (normalized as described above) and theoretical $L_{2,3}$ XAS spectra for Ni; results for Co are similar. Then the corresponding L_2 and L_3 parts of the experimental XMCD (Fig. 6.3), were multiplied by the corresponding $\gamma_j(E)$ functions. Appropriate linear combinations of the integrated intensities then gives $\langle S_z \rangle$ and $\langle L_z \rangle$, yielding after edge separation corrections, $\langle S_z \rangle = 0.23, 0.73$, and 0.83, and $\langle L_z \rangle = 0.049, 0.132$, and 0.094, for for Ni, Co, and Fe, respectively. We note that as one moves to metals with smaller atomic number, the spin-orbit splitting becomes smaller, so that L_2 and

L_3 edges overlap to a greater extent, and also local field effects [58] become more important. As a result, it becomes more difficult to estimate the correction to spin moments to correct for $L_{2,3}$ edge overlap. As expected from the theoretical tests, the moments obtained using our approach are $10-15\%$ smaller than those obtained from the standard sum rule procedure. This discrepancy has been corroborated [113], by measurements of the total magnetic moment for Ni films by XMCD and by polarized neutron reflection. Their results from XMCD spectra normalized using the standard step-function subtraction also turned out to be about 10% larger than those obtained by polarized neutron reflection. Although results of the usual approach, especially for the ratio $\langle L_z \rangle / \langle S_z \rangle$ [105], are in better agreement with gyromagnetic data [114], the precise relation between gyromagnetic and XMCD results is not clear, since the former is based on a purely classical atomic picture and involves several assumptions [115].

6.5 Transferability of the atomic ratio

As a test of the transferability of the atomic ratio $\gamma(E)$, we also performed calculations for the CoPt alloy system [116]. Fig. 6.4 shows the good agreement between $\gamma(E)$ calculated for the Co L_3 edge in Co metal and in a $Co_{0.5}Pt_{0.5}$ ordered alloy with $L1_0$-type crystal structure.

To enable quantitative comparisons between the charge counts in Co metal and CoPt alloys, which have quite different crystal structures, we fixed the volume of the Co cell in the CoPt alloy to that of the atomic sphere containing one atom in Co metal. The agreement in Fig. 6.4 shows that $\gamma(E)$ calculated for Co metal can be used to obtain Co hole counts for CoPt with less than 5% error. Thus, one can tabulate the L_3 and L_2 $\gamma(E)$ functions to obtain hole counts in complex transition metal systems. This transferable procedure yields cellular counts corresponding to the volume of the atomic sphere used in the calculation of $\gamma(E)$, and avoids the need

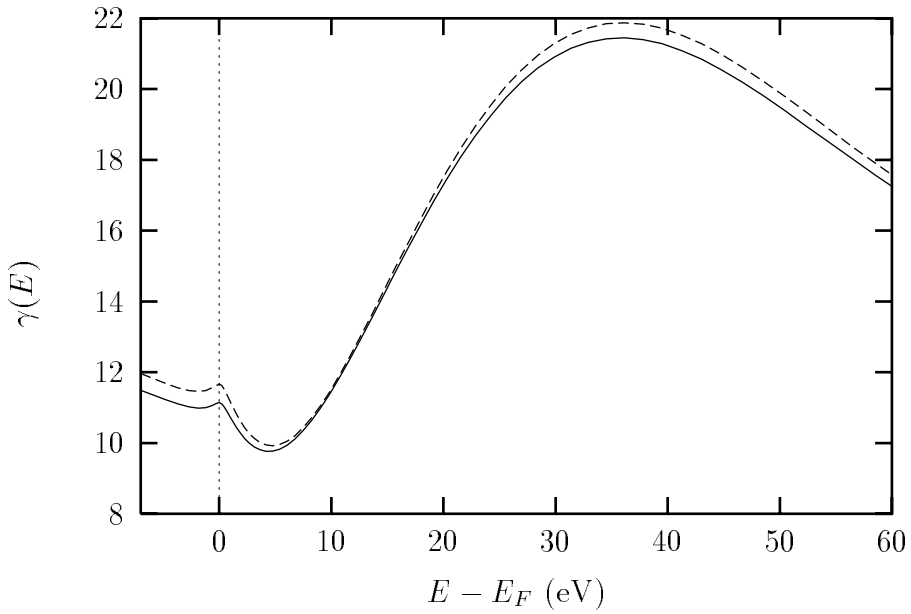

Figure 6.4: Comparison between the theoretical ratios $\gamma(E)$ for Co metal (solid line) and for CoPt alloy (dashes). For the alloy the atomic sphere volume of the Co was set equal to that for Co metal.

for separate atomic calculations in every case.

6.6 Discussion

As noted above, we have verified that our procedure works well in the single electron case. However, in XAS measurements, many body effects are unavoidable. Thus significant changes in x-ray spectra are expected due to core-hole lifetime broadening, self-energy, shake-up shake-down multielectron excitations, final state photoelectron - core hole interactions (multiplet effects and edge singularities), and the screening of the photon electric field. Final state broadening and self-energy effects are expected to have small effects on sum rules since they merely shift and broaden spectral features, and are not expected to change integrated quantities. Screening of the photon field can modify the dipole matrix element and hence will change μ_0 and hence the ρ_0/μ_0 ratio, but not the applicability of the above procedure for spin and orbital moments.

Also multielectron excitations, which usually have small effects in XAS are expected to shift oscillator strength, but not to change integrated quantities. The most challenging of these effects for our sum rule normalization procedure is the presence of multiplet splitting effects in typical magnetic materials. The core-hole interaction cannot change the unoccupied states, determined by the ground state, however the energy of unoccupied state may change due to the core-hole interaction. However, this effect leads to an additional multiplet splitting of order 5 eV [117]. Since ρ_0/μ_0 ratio is smooth on scale of 5 eV, such multiplet splitting cannot lead to significant errors. We also note that the original sum rules were derived for atomic system including multiplet and crystal-field effects, but excluding delocalized states. In the present paper we showed that previously used procedure to exclude delocalized states does not work well and leads to significant, and uncontrolled errors, even for a single-electron test. Thus the standard procedure cannot be expected to work well for many body case either. Also the approximations in their original atomic derivation limits the accuracy of the sum rules to a few percent, and the effects omitted in the derivation, will also lead to finite error.

Chapter 7

HOLE COUNTS FROM X-RAY ABSORPTION SPECTRA

The determination of hole counts from x-ray absorption spectra (XAS) has been of interest for many years, since the XAS is directly related to the final state angular momentum ℓ projected density of electron states (LDOS). In the 1970, the Pt white line was related to the number of d-holes [9]. Later, a quantitative procedure to obtain such hole counts was proposed [118]. These methods are based on a tight-binding linear combination of atomic orbitals (LCAO) picture and thus essentially give occupation numbers in terms of Mülliken counts. However, the procedure is complicated by the presence of contributions to the XAS spectra from both localized orbitals and delocalized atomic continuum states. Their separation is typically performed with an *ad hoc* step-function subtraction of delocalized states [62, 63, 105, 106, 119]. Also the procedure needs an *a priori* estimate of the number of holes or the reduced matrix element for the $p \rightarrow d$ transition. Thus a better approach is desirable.

The number of holes can be calculated theoretically in several ways, as reviewed by Miller et al. [91]. These authors criticized cellular counts, since the separation of space into cells is ambiguous, and argued in favor of a Mülliken analysis. However, as discussed below, the XAS from deep core levels is not sensitive to the density matrix beyond the cell boundaries, and thus cannot precise determine such Mülliken counts, which depend on the density matrix throughout the range of a given orbital. Also, the LCAO picture has a fundamental problem connected with nonzero amplitude of atomic orbitals at neighboring sites. This can be regarded as a violation of the Pauli principle [120], since the orbital tails do not satisfy Schrödinger equation in the potential near the neighbors. As a result, the total number of such d electrons

per site is not 10. To cope with this problem Hodges et al. [120] suggested the renormalized-atom (RA) method, which has many advantages for transition metal properties.

In this Chapter we develop a procedure to extract RA hole counts from XAS and compare them to directly calculated RA, cellular and Mülliken counts [15]. Our approach is based in part on *ab initio* atomic calculations of a smooth transformation relating the XAS spectrum to the LDOS.

7.1 Mülliken and renormalized atom hole counts

The theoretical approach described here is an extension of our work presented in Chapter 6. Here we discuss the use of projection operators to obtain Mülliken and RA counts from $\hat{\rho}$ and to separate the DOS into localized and delocalized parts.

The transformation from the XAS $\mu(E)$ to the LDOS $\rho(E)$, i.e., the number of electrons per unit energy, can be derived within MS theory [109], see Chapter 6. Starting from the Golden rule, one obtains a linear relation between $\mu(E)$ and the electron density matrix $\hat{\rho}(E)$, i.e., $\mu(E) = A * \hat{\rho}(E)$. The relationship between XAS and DOS is given by Eq. 6.1 The ratio $\gamma(E)$ is essentially an atomic quantity which can be calculated by any code based on MS theory or even appropriately modified atomic codes. Strictly speaking both μ_0 and ρ_0 refer to embedded atomic quantities, i.e., the effective atomic states defined by the local molecular potential at a given site. Multiple scattering theory is based on separation of space into cells (Voronoi polyhedra) and thus the number of holes (or the change in number of holes) corresponds to space separation counts. Such a space separation is not unique, and therefore one faces difficulty in interpreting the results.

Using Eq. 6.1 one can transform the experimental XAS spectrum into the normalized DOS above the Fermi level. However, this unoccupied DOS contains contributions both from localized atomic-like states and from delocalized atomic continuum

Table 7.1: Occupied and total (where applicable) d-electron counts with various methods. The last column give the RA hole counts from simulated x-ray absorption spectra. The discrepancy between last two columns is due to Γ_{ch} broadening, as discussed in the text.

counts	cellular	Mülliken	RA	RA holes (XAS)
Fe, $3d$	6.76	7.82	6.56	2.96
Fe, $3d$-tot		10.41	9.94	
Co, $3d$	7.52	8.43	7.32	2.26
Co, $3d$-tot		10.39	9.95	
Ni, $3d$	8.57	9.26	8.36	1.48
Ni, $3d$-tot		10.37	9.96	
Pt, $5d3/2$	3.56	4.40	3.49	0.46
Pt, $5d3/2$-tot		4.44	3.97	
Pt, $5d5/2$	4.68	6.58	4.60	1.14
Pt, $5d5/2$-tot		6.81	5.94	

states. A projection operator can then be used to obtain localized contribution into DOS. In particular, the Mülliken count is given by projection of all occupied wave functions onto a particular atomic orbital.

$$n_L = \sum_n^{occ} |\langle \psi_L^{at} | \psi_n \rangle|^2 = \int_{-\infty}^{E_F} \langle \psi_L^{at} | \hat{\rho} | \psi_L^{at} \rangle. \tag{7.1}$$

The main disadvantage of Mülliken counts is that if one sums the occupied and unoccupied $3d$-states, one gets a total count different from 10, due to the overlap of $3d$ orbital with orbitals centered on neighbors. Indeed, our estimate for the total Mülliken d-count in Fe, Co and Ni is 10.4 (Table 7.1). Therefore one faces the problem of separating tail contributions from Mülliken counts to obtain physically meaningful total $3d$ counts. The situation is even worse for s and p electrons, which extend much further.

The RA method has been proposed to overcome the above difficulty. Within the RA approach, each atomic orbital is set to zero outside a given radius R_0, and is multiplied by a constant factor inside to recover unit normalization. The RA states are therefore better approximations to the embedded atom states inside a cell. Also the wave functions used in the projection operator become essentially orthonormal to each other, and the tail contribution is expected to be much smaller. The RA counts thus overcome the problem of nonorthogonality of orbitals, and also justify the use of the formula $\rho = \rho_0(1 + \chi)$. The error in total RA count for occupied and unoccupied states was found to be an order of magnitude smaller for each d_j subshell than the corresponding Mülliken count (Table 7.1). Our calculations were performed with the self-consistent real space multiple-scattering code FEFF8 [7]. The total number of $3d$ electrons obtained with RA counts is 9.95 for Fe, Co, Ni and an integration up to 100 eV above the edge. The $4s$ RA count is 1.90 for all tested cases, with integration up to 400 eV. The error mostly arises from inaccuracy of our grid for the integration to that high energy. Thus with the RA method one can easily transform hole counts to meaningful electron counts and this transformation is valid for localized d and f electrons, as well as for highly delocalized s and p electrons.

The RA counts depend on the choice of the radius R_0. The most natural choice is that for which the total count for occupied and unoccupied d-states is equal to 10. Thus unlike the ambiguous cellular counts, the RA method fixes the radius of cell. The present work shows that this radius is very close to the Norman radius R_N, i.e., the radius for which the net charge enclosed is the atomic number [121]. With such a definition of a cell, both s and d total counts per site are simultaneously close to the numbers expected from the Pauli principle. Charge transfer also has a natural definition as the net charge within Norman sphere, which can be separated unambiguously into s, p, d and f electron contributions.

Table 7.1 summarizes our results for d-electron counts. The first three columns show the occupation numbers for cellular, Mülliken and RA counts. All of them show

Table 7.2: Occupied (cellular and RA) and total (RA) s-electron counts with cellular and renormalized-atom methods. The total RA number is obtained by integration up to 400 eV above the Fermi level.

counts	cellular	RA	RA total
Fe, 4s	0.61	0.61	1.90
Co, 4s	0.62	0.61	1.90
Ni, 4s	0.63	0.63	1.90
Pt, 6s	0.73	0.72	1.90

an expected change of about 1 d electron from Fe to Co and from Co to Ni. The cellular and RA counts are very close to each other, while Mülliken count is about 1 d electron larger. The fractional counts can be interpreted as the wave function being a mixture of $d^n s$ and d^{n+1} states. Note that the RA counts are much closer to those expected from atomic multiplet calculations, where Ni is regarded as having a d^8 configuration [74]. For Pt we find that the calculated ratio of $d_{5/2}$ holes to $d_{3/2}$ holes is 2.8, in agreement with the value 2.9 calculated by Mattheiss and Dietz [10], thus updating an earlier estimate [9]. The total number of d-holes for Pt in RA is 1.8, which is also consistent with Mattheiss and Dietz.

Table 7.2 presents the s-electron counts with cellular and RA methods. We could not make a reliable estimate of Mülliken counts in this case, since the 4s orbital extends significantly beyond the nearest neighbor distance. Note that for s-electrons, the occupied RA and cellular counts are also practically equal. The RA total count is 1.9 for all cases, and shows that RA method works well with highly non-localized s and p orbitals. However, the s-counts are not accessible from $L_{2,3}$ edge x-ray absorption due to domination of $\ell \rightarrow \ell + 1$ transition. However the p-count can be obtained from either K or L_1 edge XAS.

7.2 Separation of XAS and DOS into localized and continuum contributions

The main idea of our approach is to separate the localized and continuum contributions to $\hat{\rho}$ using the projection operator P_{at} which projects onto a particular atomic orbital (free or renormalized atom), i.e., $\hat{P}_{at} = |\psi^{at}\rangle\langle\psi^{at}|$. The radial part of the photoelectron wave function $\psi(\vec{r}, E)$ can be separated into localized and continuum parts, $\psi = \psi^{loc} + \psi^{cont}$

$$\begin{aligned} \psi^{loc}(\vec{r}, E) &= \hat{P}_{at}\psi(\vec{r}, E) = \langle\psi^{at}|\psi\rangle\psi^{at}(\vec{r}) \,, \\ \psi^{cont}(\vec{r}, E) &= \psi(\vec{r}, E) - \psi^{loc}(\vec{r}, E) \,, \end{aligned} \tag{7.2}$$

where the overlap integrals $\langle\psi^{at}|\psi\rangle$ are functions of energy only. Separation of the photoelectron wave function (with quantum index $\kappa = 5$) into localized and continuum parts is shown in Figs. 7.1 and 7.2. There we also show the atomic wave function ψ^{at} of the corresponding symmetry ($3d_{5/2}$). The photoelectron wave function in Fig. 7.1 is calculated at an energy very close to the Fermi level. In this case, the photoelectron wave function is mostly localized and its delocalized atomic continuum part is small. The second plot, Fig. 7.2, show the opposite situation when the energy is high above the edge (around 30 eV above E_F) and the photoelectron wave function is mostly delocalized.

The local DOS, $\rho(E) = \langle L|\hat{\rho}(E)|L\rangle$, can be decomposed as

$$\rho(E) = \rho^{loc}(E) + \rho^{cont}(E) \tag{7.3}$$

by substituting $\hat{\rho}(E) = \hat{P}_{at}\hat{\rho}(E) + (1 - \hat{P}_{at})\hat{\rho}(E)$. Note that the cross term contribution is exactly zero in this case, since $\rho^{cross} = 2\int d^3r\psi^{at}(\vec{r})\psi^{cont}(\vec{r}) = 0$, from the definition of projection operator. Thus the separation of DOS into localized atomic and continuum parts is unambiguous. The projection operator acts only on the radial part in Eq. 6.6, and therefore localized and delocalized contributions should have the same χ.

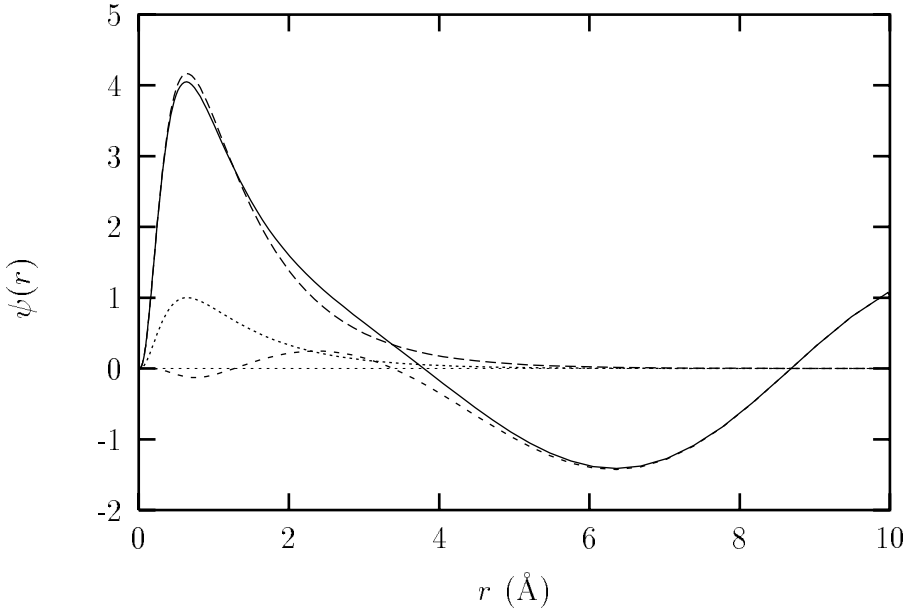

Figure 7.1: Separation of the d photoelectron wave function (solid line) in Ni into localized (dashes) and continuum contributions (short dashes). Also shown id $3d$ atomic orbital (dots). The photoelectron energy is close to the Fermi level.

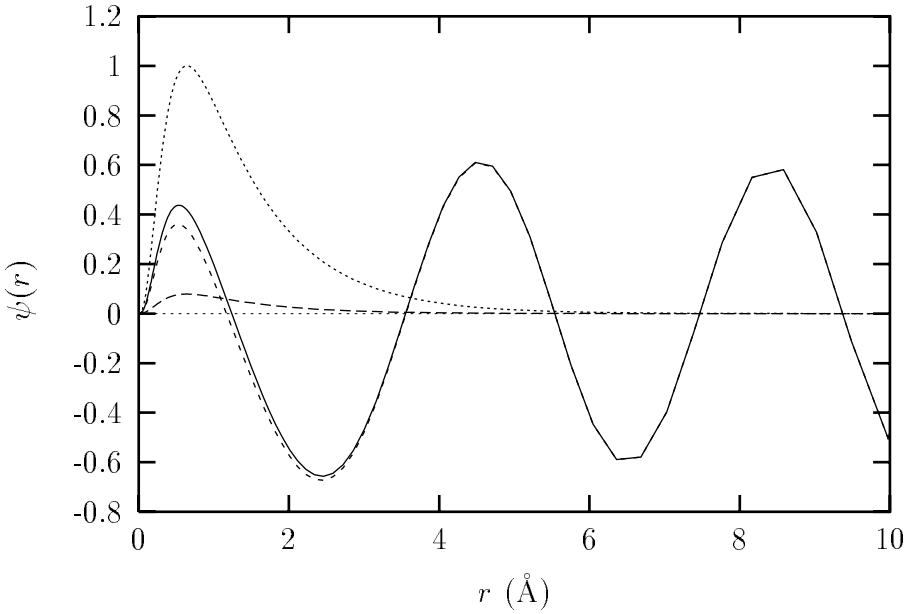

Figure 7.2: Separation of the d photoelectron wave function (solid line) in Ni into localized (dashes) and continuum contributions (short dashes). Also shown the $3d$ atomic orbital (dots). The photoelectron energy is 30 eV above the Fermi level.

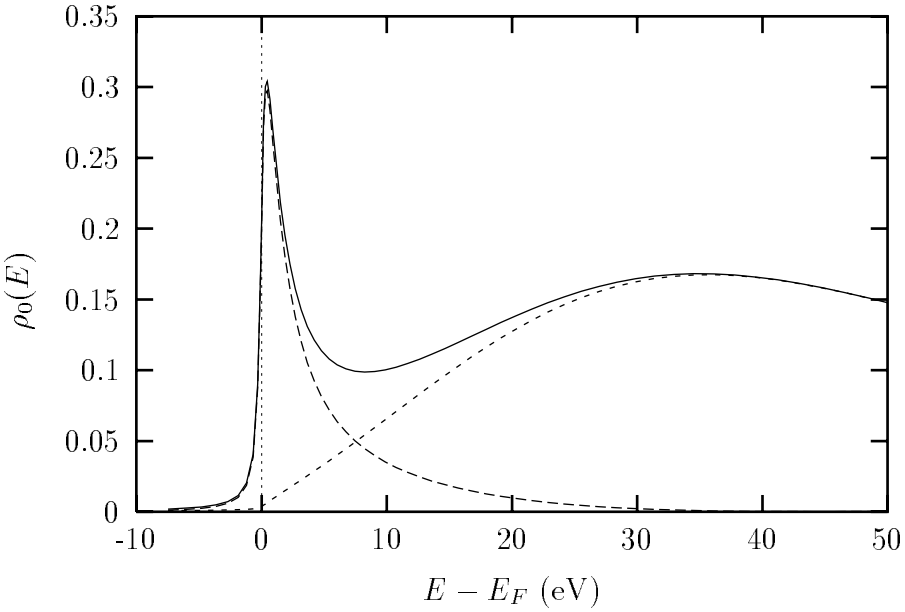

Figure 7.3: Separation of the d-projected density of states $\rho_0(E)$ (solid line) in Ni into localized (dashes) and continuum (short dashes) contribution.

In theoretical calculations, it is also possible to project onto any particular orbital character: e.g. to atomic t_{2g} or e_g orbitals. These orbitals result from splitting of d states by a cubic crystal field, and their occupation and ordering is often used to explain properties of $3d$ elements. However, such a projection cannot be performed for experimental spectrum. Within dipole approximation, only six irreducible operators can be extracted from polarization dependent XAS [23] and the number of holes is one of them. The direct separation of XAS into localized (i.e. projected atomic) and delocalized (i.e. continuum) parts cannot be made unambiguously. If the projection operator is used to separate final state wave function, the XAS spectrum can be expressed as

$$\mu \propto \langle i|\vec{\epsilon}\vec{r}|\psi^{loc} + \psi^{cont}\rangle|^2 = \mu^{loc} + \mu^{cont} + \mu^{cross}\,, \tag{7.4}$$

where the cross term is nonzero. Previous procedures [9] ignore μ^{cross}. But the cross term has the largest contribution exactly where localized and delocalized contributions are comparable and an *ad hoc* separation of μ^{cross} or its neglect can lead to erroneous

results.

7.3 Renormalized atom counts from XAS

In this section we describe a procedure to obtain hole counts from XAS, and apply it to theoretically calculated XAS. Such theoretical test is necessary both to check the validity of the procedure and also to estimate possible systematic errors of the method. For example, in theoretical calculations, one can include or exclude the $\ell \rightarrow \ell - 1$ transition, and thus estimate the error in hole count due to their inevitable presence in the measured signal.

Since χ is expected to be the same for localized and delocalized parts, and therefore the same as for XAS, one can transform the XAS directly to localized part of DOS:

$$\rho^{loc}(E) = \gamma^{loc}(E)\mu(E)\,, \tag{7.5}$$

where

$$\gamma^{loc}(E) = \frac{\rho_0^{loc}(E)}{\mu_0(E)}\,. \tag{7.6}$$

These equations provide the basis for our new procedure to obtain electron configuration counts from experimental absorption spectra. Thus one simply multiplies the experimental XAS after normalization, as discussed below, by the theoretically calculated atomic-like ratio $\gamma^{loc}(E)$, to obtain the contribution to the DOS from localized electrons. In Fig. 7.4 we show the atomic-like ratios $\gamma^{loc}(E)$ and $\gamma(E) = \rho_0(E)/\mu_0(E)$. The integral over energy of the localized contribution $\rho^{loc}(E)$ gives the number of holes in the electron configuration for a particular orbital character. Unfortunately due to the dipole selection rule, the determination of the number of s-holes, especially when d-shell is partially occupied, is not reliable. However, one can obtain from XAS an estimate for the number of p, d and f electron in terms of RA counts.

We would like to note that one can use a slightly different way of obtaining hole counts. In our procedure, the contribution from continuum states to XAS can be

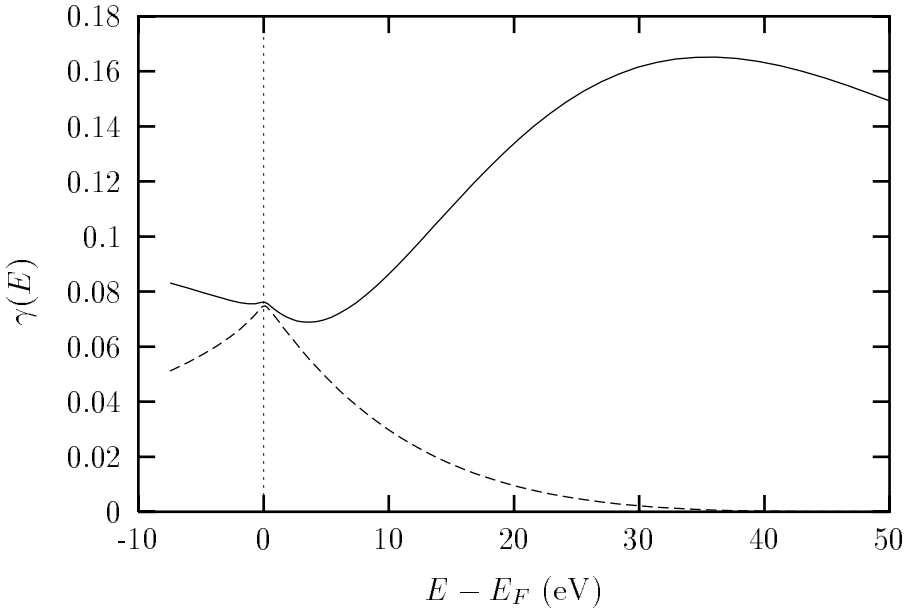

Figure 7.4: Theoretically calculated atomic-like ratios $\gamma(E)$ (solid line) and $\gamma^{loc}(E)$ (dashes) for L_3 edge in Ni.

calculated unambiguously in the following way

$$\mu^{cont}(E) = \gamma^{-1}(E)\rho^{cont}(E)\,. \tag{7.7}$$

Then, one can subtract $\mu^{cont}(E)$ contribution from the experimental XAS and transfer XAS into the localized DOS by multiplying it on $\gamma(E)$. The separation of the atomic background contribution $\mu_0(E)$ into localized and continuum part as described above is shown in Figs. 7.5. The two procedures for obtaining hole counts from experiment that we described, namely i) transformation of XAS into localized DOS using $\gamma^{loc}(E)$ and ii) subtraction of the continuum contribution from XAS and subsequent transformation of the resulting signal to localized DOS using $\gamma(E)$, are equivalent. The second one might have a more transparent connection with the usual approaches of obtaining hole counts from experiment which involve *ad hoc* subtraction of the contribution from the delocalized states.

To summarize, our procedure, which can be generalized for various experimental

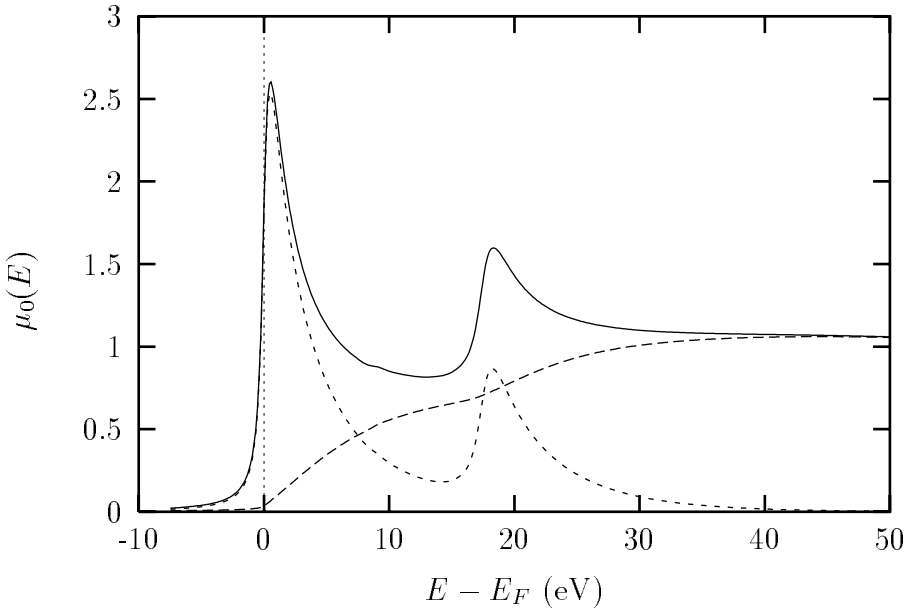

Figure 7.5: Separation of the calculated smooth atomic background contribution $\mu_0(E)$ in Ni (solid line) into localized (short dashes) and continuum (dashes) parts.

applications, has several steps.

1) Subtract the pre-edge contribution and (if possible) separate edges. This was not necessary in the theoretical test since one can calculate the L_2 and L_3 edges separately.

2) Normalize experimental XAS background about 50 eV above the edge to that theoretically calculated or measure the absorption coefficient in absolute units. This step was also not needed in out theoretical test.

3) Transform the XAS into DOS projected onto a particular renormalized atomic orbital using Eq. 7.5.

4) Integrate to get the RA hole count for the electron configuration.

5) Multiply by a theoretical factor to correct for lifetime broadening effects.

For final d and f states, one can obtain separately the number of electrons with total angular momentum $j = \ell \pm 1/2$ when the corresponding $L_{2,3}$ or $M_{4,5}$ edges are well separated. Only the total number of p electrons can be estimated from K, and L_1 edges.

Numerical tests of the first four steps of this approach for $3d$ transition metals show that typically the number of holes obtained from XAS by the above 4 steps is underestimated by about 10-20%. The main source of this reduction stems from the strong effect of core-hole lifetime broadening on white lines, as verified by observing that the reduction vanishes when Γ_{ch} is reduced to zero. To see this, suppose that all states below E_0 are localized and all states above are delocalized. Then due to core hole broadening, the localized DOS will leak above E_0, and the delocalized, below. However, since in the case of white lines the localized DOS is larger, the integration to the ideal localized - delocalized separation energy will give reduced number of localized states. The theoretically calculated reduction factor for the d-hole count due to Γ_{ch} broadening is 1.14 for Fe, 1.16 for Co, 1.07 for Ni, 1.04 for Pt d3/2, and 1.18 for Pt $d_{5/2}$ holes.

In the analysis of XMCD data one can avoid the use of reduction coefficient if the goal is to obtain spin and orbital moments in terms of cellular counts, see preceding Chapter 6. In that case one can use the smooth ratio $\gamma(E)$ instead of $\gamma^{loc}(E)$ given by Eq. 7.5. As one can see from Tables 7.1 and 7.2, the cellular counts within Norman sphere are very close to the RA counts. Their similarity means that the shape of d and s orbitals practically does not change within the Norman radius. The smoothness is important since, for example, multiplet effects can lead to an additional splitting of order 5 eV, but with a smooth $\gamma(E)$ the error in hole counts due to this effect is expected to be smaller than for the transformation to the localized DOS using $\gamma^{loc}(E)$, which has a significant rise at the border between localized and delocalized states. As one can see from the hole count calculations, such a procedure can lead to a significant errors.

In Fig. 7.6, we demonstrate the separation of XAS into localized and delocalized contributions. The directly calculated total XAS spectrum is represented by a solid line. The delocalized contribution is obtained by transforming XAS into DOS, subtracting the localized DOS contribution, and transforming the delocalized DOS

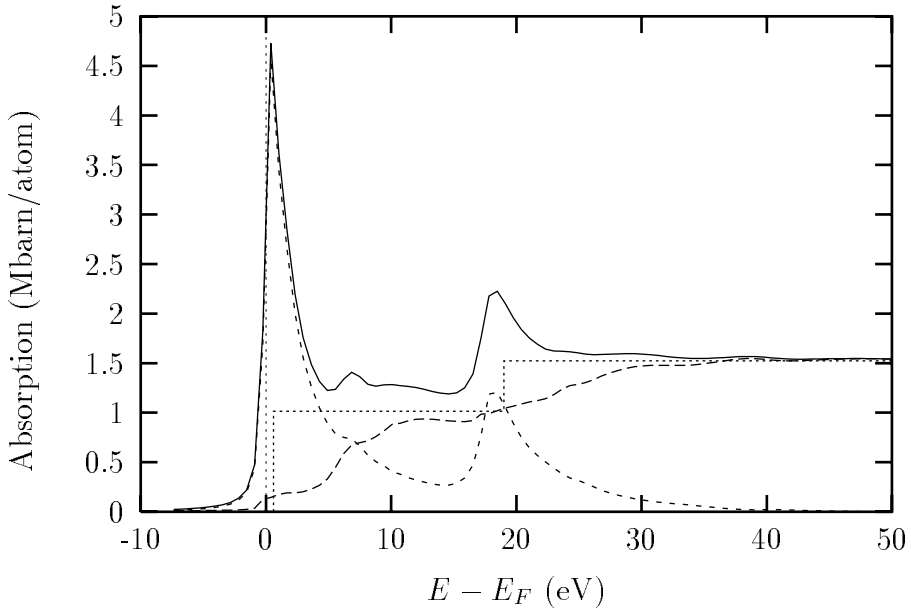

Figure 7.6: Separation of the calculated Ni XAS spectrum (solid line) into localized (short dashes) and delocalized (continuum) parts (dashes). The dots show the *ad hoc* step function representation of delocalized states in the conventional procedure.

back to an XAS spectrum. As expected, at high energies the delocalized contribution dominates, while near the edge practically all absorption comes the localized part. For comparison, we also present an *ad hoc* two edge-step modeling of the delocalized contribution, which is often employed in XMCD analysis and clearly gives a poor approximation to the unambiguous delocalized contribution calculated by FEFF8.

In the procedure of Brown et al. [9], the difference between Pt L_2 and L_3 is interpreted as solely caused by the localized contribution to the XAS data. If this were the case, the devision of the difference signal by the square of the $p \rightarrow d$ matrix element would yield the difference in the number of $d_{3/2}$ and $d_{5/2}$ holes. However, this analysis must be modified in the presence of the cross term, because the difference in $d_{3/2}$ and $d_{5/2}$ occupation will show up both in localized and in the cross-term contributions. Our procedure specifically avoids the cross-term contribution by transforming XAS spectra into DOS, and hence yields, we believe, a more reliable analysis of occupation

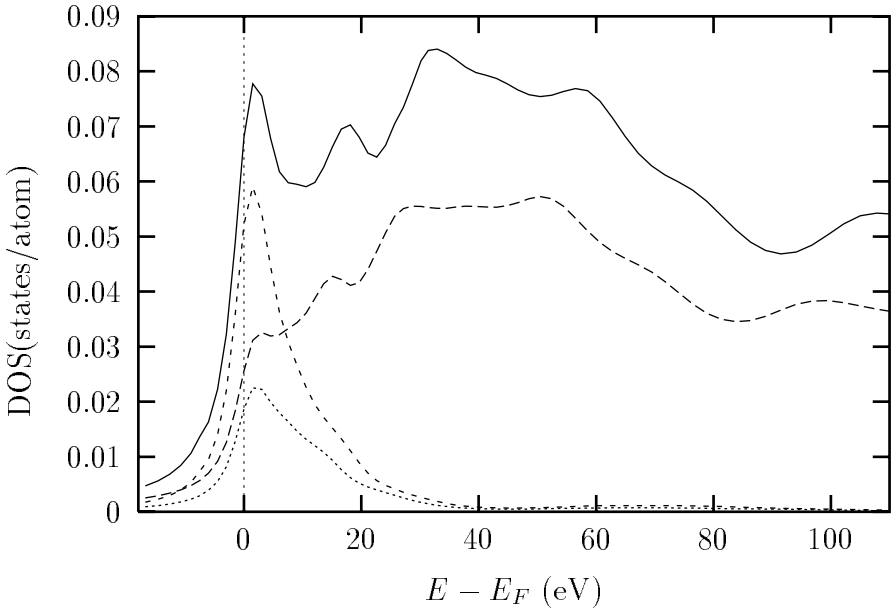

Figure 7.7: XAS transformed to localized d-DOS for Pt L_2 (solid line) and L_3 (dashes) edges. Short dashes and dots show delocalized DOS contribution.

numbers.

Fig. 7.7 represents the application of this procedure to Pt $L_{2,3}$ data. The FEFF8 calculations agree well with Pt XAS [122]. Even though the peak positions are not changed by our procedure, the ratio of peak intensities in the total DOS is significantly altered compared to XAS spectrum. The localized DOS is mostly limited to the region of first two peaks, i.e. about 40 eV above the edge. By inspection, one sees that the ratio of $5d_{5/2}$ and $5d_{3/2}$ hole counts should be around 3.

Several many-electron effects may be important for the extraction of hole counts. For example, the usual dipole matrix elements, which are not corrected with respect to local screening of the x-ray electric field, are not accurate for $3d$ metals, as the screening effect modifies the L_3/L_2 white-line ratio [58]. As we will show in Chapter 8, our procedure can account for this effect by including screening in the calculated μ_0. Multiplet splitting and multielectron excitations are neglected in the above single-particle derivation. However, such effects are not expected to change the counts significantly,

since the splitting is expected to transfer spectral density only within about 5 eV of absorption edge, where the ratio is smooth. Thus one expects a greater cancelation of these effect in Eq. 6.1, than in Eq. 7.5. Eq. 6.1 can be used to obtain S_z and L_z from XMCD, see Chapter 6, but inapplicable to the problem of hole determination.

Chapter 8

LOCAL FIELD EFFECTS IN X-RAY ABSORPTION

So far we considered the x-ray absorption process in the single-electron approximation. As discussed in the previous Chapters, the single-electron multiple scattering theory gives a very good agreement with experimental L-shell XANES in case of transition metals with almost filled d band. However, the agreement gets worse as one moves left across the periodic table toward elements with almost empty d band. Experimental [18, 19, 53, 54] and theoretical [55, 56, 57, 58] XAS and EELS studies show that one of the most serious failures of the single-electron picture is that it predicts a L_3/L_2 white line ratio of $2:1$, as based on the $2j+1$ degeneracy of the initial $2p$ core states whereas the observed ratio becomes smaller that $1:1$ for V. Strictly speaking, the L_3/L_2 ratio is modified due differences in lifetime broadening of L_3 and L_2 edges and relativistic effects. However, in case of $3d$ transition metals these effects are small and cannot describe the strong deviation observed in experiment.

Generally speaking, two types of many body effects, core hole relaxation and dielectric polarization, can be identified which modify the single-electron description of XAS. On one hand, the transition of an electron from a deep core level into the unoccupied orbital results in the creation of a core hole in XAS process. Therefore, the initial (ground state) Hamiltonian and final- state Hamiltonian are different since the core provides an attractive potential that affects all other electrons in the system. On the other hand, the external x-ray field acts on all electrons in the systems and distorts the atomic charge cloud. In response to the perturbation the electrons redistribute themselves and produce internal screening (or antiscreening) fields which in turn can strongly modify the photoabsorption cross-section. This effect was so far ignored in

our previous calculations, and will be addressed in this Chapter.

There have been numerous studies concerning the dielectric polarization and relaxation effects in closed shell atoms, especially in case of the so-called giant dipole resonances in the $4d$-photoionization cross-section of Xe, Ba, La, and similar atomic systems: for a review see [123, 124]. It became obvious long time ago that independent particle approaches based on potentials of the Hartree-Fock (HF) or the Hatree-Fock-Slater (HFS) type for the ground state charge distribution are not able to describe experimentally observed photoionization cross-section data in those systems. Thus, several new theoretical approaches were developed to deal with many-body effects. One of the approaches is an extension of the Hartree-Fock approximation, known as the random-phase approximation with exchange (RPAE) [125, 126, 127]. An alternative approach based on the time-dependent local density approximation (TDLDA) has been developed by Zangwill and Soven [17] and Stott and Zaremba [128] which avoids the difficulty of non local exchange. A similar scheme based on the local density random-phase approximation (LDRPA) was used in [129]. All these approaches yield good agreement for the photoabsorption and photoionisation cross sections for atoms and molecules. At the same, the implementation of the two approaches (TDLDA and RPAE) differ in how they treat the core-hole relaxation effect. More specifically, there is a question of whether the LDA ground state potential effectively contains a hole in the core region, as it was suggested in [130, 131]. This brings up an important, as yet unresolved, problem of the interplay between polarization and core hole relaxation effects. We will come back to it at the end of this Chapter, where we discuss the shortcomings of the TDLDA approach.

The original TDLDA approach of Zangwill and Soven have been extended to calculate the dielectric response of simple metals [132, 133], alkali metals [134], and metal clusters [135, 136, 137, 138, 139]. The goal of this work is to use TDLDA approach to account for many-body polarization type effects on $L_{3,2}$ edge x-ray absorption spectra in solids. This problem has been very recently addressed by Schwitalla and Ebert

[58]. Our approach is different from those of Zangwill and Soven and Schwitalla and Ebert in several ways. First, our approach is based on the real space Green's function formalism. Second, we treat the delocalized states in a way which leads to a better agreement between theoretical calculations and experiment. The third difference is more subtle. The effect under consideration is basically a dielectric polarization effect which can be taken into account by modifying the dipole matrix element to reflect the screening of the external x-ray photon field. Therefore, we prefer to put the many-body effects in the effective local field following Zangwill and Soven. Alternatively, one can keep the photon field unchanged and put the many-electron effects into the effective wave function (or response function) [131]. Since the only unique physical quantity is the absorption cross-section, this difference reflects different physical pictures of the same complex dynamic process of x-ray absorption.

8.1 Time-Dependent Local Density Function Theory

In this section we will briefly describe the TDLDA theory. We will mostly follow the original paper of Zangwill and Soven [17]. In this formalism the absorption coefficient μ can be written using its relationship to the response function χ

$$\mu(\omega) = -\frac{4\pi}{c\omega}\mathrm{Im}\int d\vec{r}\int d\vec{r}\,'\,\phi^{ext*}(\vec{r},\omega)\,\chi(\vec{r},\vec{r}\,',\omega)\,\phi^{ext}(\vec{r}\,',\omega)\,, \tag{8.1}$$

where we used a more convenient notation for the external field, $\phi^{ext}(\vec{r},\omega)$. The response function $\chi(\vec{r},\vec{r}\,',\omega)$ is the time Fourier transform of the retarded density-density correlation function,

$$i\chi(\vec{r},\vec{r}\,',t-t') = \langle[\hat{\rho}(\vec{r},t),\hat{\rho}(\vec{r}\,',t')]\rangle\,, \tag{8.2}$$

where $\hat{\rho}(\vec{r},t)$ is the density operator in the Heisenberg representation, $\theta(t)$ is a step function, and the angular brackets denote a ground state expectation value. The single-electron approximation for μ then corresponds to using the non-interacting response function $\chi_0(\vec{r},\vec{r}\,',\omega)$ and external (unscreened) x-ray field $\phi^{ext}(\vec{r})$. To go

beyond single-electron approximation, we can use the TDLDA approach. The starting point is the expression for the induced density of non-interacting electrons in the presence of the external x-ray field

$$\rho(\vec{r},\omega) = \int d\vec{r}\,'\chi_0(\vec{r},\vec{r}\,',\omega)\,\phi^{ext}(\vec{r}\,',\omega)\,. \tag{8.3}$$

Each individual electron, however, experiences a field produced by other electrons in addition to the bare external field. This induced field ϕ^{ind}, can be represented as a sum of two parts

$$\phi^{ind}(\vec{r},\omega) = \phi^{C}(\vec{r},\omega) + \phi^{xc}(\vec{r},\omega)\,, \tag{8.4}$$

an induced Coulomb potential

$$\phi^{C}(\vec{r},\omega) = \int d\vec{r}\,'\frac{\delta\rho(\vec{r}\,',\omega)}{|\vec{r}-\vec{r}\,'|}\,, \tag{8.5}$$

and an induced exchange-correlation (have taken to be static) potential

$$\phi^{xc}(\vec{r},\omega) = \left.\frac{\delta V_{xc}(\vec{r})}{\delta\rho(\vec{r})}\right|_{\rho(\vec{r})=\rho_0(\vec{r})}\delta\rho(\vec{r},\omega)\,. \tag{8.6}$$

obtained by linearizing the LDA functional around the ground-state density. More details about the time dependent density functional theory can be found in, e.g, [140].

We require now that electrons respond to a new self consistent field

$$\delta\rho(\vec{r},\omega) = \int d\vec{r}\,'\chi_0(\vec{r},\vec{r}\,',\omega)\phi^{scf}(\vec{r},\omega)\,. \tag{8.7}$$

where

$$\phi^{scf}(\vec{r},\omega) = \phi^{ext}(\vec{r},\omega) + \phi^{ind}(\vec{r},\omega) \tag{8.8}$$

It is convenient to introduce a kernel function $K(\vec{r},\vec{r}\,')$,

$$K(\vec{r},\vec{r}\,',\omega) = \frac{1}{|\vec{r}-\vec{r}\,'|} + \delta(\vec{r}-\vec{r}\,')\left.\frac{\delta V_{xc}(\vec{r})}{\delta\rho(\vec{r})}\right|_{\rho(\vec{r})=\rho_0(\vec{r})}\,, \tag{8.9}$$

which gives an integral equation for ϕ^{ind}

$$\phi^{ind}(\vec{r},\omega) = \int d\vec{r}\,'K(\vec{r},\vec{r}\,',\omega)\delta\rho(\vec{r}\,',\omega)\,, \tag{8.10}$$

and hence

$$\phi^{scf}(\vec{r},\omega) = \phi^{ext}(\vec{r},\omega) + \int d\vec{r}\,' d\vec{r}\,'' K(\vec{r},\vec{r}\,')\,\chi_0(\vec{r}\,',\vec{r}\,'',\omega)\,\phi^{scf}(\vec{r}\,'',\omega)\,. \tag{8.11}$$

The induced field $\phi^{ind}(\vec{r},\omega)$ and induced density $\delta\rho(\vec{r},\omega)$ are frequency dependent complex functions because the system may not oscillates in phase with the external driving field. Equations 8.4 - 8.8 are solved simultaneously and self-consistently.

The expression for the absorption coefficient then should be modified as

$$\mu(\omega) = -\frac{4\pi}{c\omega}\mathrm{Im}\int d\vec{r}\int d\vec{r}\,'\,\phi^{ext*}(\vec{r},\omega)\chi_0(\vec{r},\vec{r}\,',\omega)\,\phi^{scf}(\vec{r}\,',\omega)\,, \tag{8.12}$$

or, equivalently,

$$\mu(\omega) = -\frac{4\pi}{c\omega}\int d\vec{r}\int d\vec{r}\,'\,\phi^{scf*}(\vec{r},\omega)\mathrm{Im}\chi_0(\vec{r},\vec{r}\,',\omega)\,\phi^{scf}(\vec{r}\,',\omega)\,. \tag{8.13}$$

Eq. 8.13 has a very transparent physical meaning. It indicates that the local field effects on x-ray absorption can be accounted for by using the local field $\phi^{scf}(\vec{r},\omega)$ instead of the external field ϕ^{ext}.

Eq. 8.13 can be also written as

$$\mu(\omega) = -\frac{4\pi}{c\omega}\mathrm{Im}\int d\vec{r}\int d\vec{r}\,'\,\phi^{ext*}(\vec{r},\omega)\chi(\vec{r},\vec{r}\,',\omega)\,\phi^{ext}(\vec{r}\,',\omega)\,, \tag{8.14}$$

where $\chi(\vec{r},\vec{r}\,',\omega)$ is connected with non-interacting function $\chi_0(\vec{r},\vec{r}\,',\omega)$ through the integral equation

$$\chi(\vec{r},\vec{r}\,',\omega) = \chi_0(\vec{r},\vec{r}\,',\omega) + \int d\vec{r}\,''\int d\vec{r}\,'''\,\chi_0(\vec{r}\,',\vec{r}\,'',\omega)\,K(\vec{r}\,'',\vec{r}\,''',\omega)\,\chi(\vec{r}\,''',\vec{r}\,',\omega)\,. \tag{8.15}$$

The two forms 8.14 and 8.13 are mathematically equivalent [17].

In TDLDA the non-interacting response function can be calculated using the wave functions and energies obtained from the LDA calculations as

$$\chi_0(\vec{r},\vec{r}\,',\omega) = \sum_{ij}(f_i - f_j)\frac{\psi_i^*(\vec{r})\psi_j(\vec{r})\psi_j^*(\vec{r}\,')\psi_i(\vec{r}\,')}{E_i + \omega - E_j + i\delta}\,, \tag{8.16}$$

where the sum is taken over the complete spectrum, i.e. both occupied and unoccupied states, factors f_i are the occupation numbers, and δ is a positive infinitesimal. For convenience, we can define $\chi_0(\vec{r},\vec{r}\,',\omega)$ in terms of individual transitions $\chi_{ij}(\vec{r},\vec{r}\,',\omega)$ which have a pole in ω at $\omega = E_j - E_i + i\delta$,

$$\chi_{ij}(\vec{r},\vec{r}\,',\omega) = \frac{\psi_i^*(\vec{r})\psi_i(\vec{r}\,')\psi_j(\vec{r})\psi_j^*(\vec{r}\,')}{\omega - E_j + E_i + i\delta}\,, \tag{8.17}$$

so that (dropping dependence $\vec{r}$ and $\vec{r}\,'$)

$$\chi_0(\omega) = \sum_{ij}(f_i - f_j)\chi_{ij}(\omega) \tag{8.18}$$

Switching indices i and j one can rewrite it as

$$\chi_0(\omega) = \sum_{ij} f_i(\chi_{ij}(\omega) - \chi_{ji}(\omega))\,. \tag{8.19}$$

The explicit calculation of the wave functions can be avoided by using the spectral representation of the Green's function

$$G(\vec{r},\vec{r}\,',E) = \sum_m \frac{\psi_m(\vec{r})\psi_m^*(\vec{r}\,')}{E - E_m + i\delta}\,, \tag{8.20}$$

where summation is done over all states. Using 8.20 and the property $\chi_{ji}(\omega) = -\chi_{ij}^*(-\omega)$, equation 8.19 can be rewritten as

$$\chi_0(\vec{r},\vec{r}\,',\omega) = \sum_{i_{occ}} \psi_i^*(\vec{r})\psi_i(\vec{r}\,')\,G(\vec{r},\vec{r}\,',E_i+\omega) + \sum_{i_{occ}} \psi_i(\vec{r})\psi_i^*(\vec{r}\,')\,G^*(\vec{r},\vec{r}\,',E_i-\omega) \tag{8.21}$$

Eq. 8.21 was used by Zangwill and Soven in this form to calculate the response function for rare gases. In case of close shell atoms, there is no ambiguity in summation over the occupied states in Eq. 8.21 since the Fermi level lies between the highest occupied single particle energy level and the lowest unoccupied level. In extended systems, however, the situation gets more complicated, and there is no clear way of treating the states in a band that is not fully occupied. More specifically, in case of transition metals the d band is not completely filled, and, since the Green's function 8.20 implicitly sums over all states, Eq. 8.21 contains transitions involving the shallow

occupied $3d$ states. To deal with such transitions, both terms in equations 8.21 should be retained, even though it might first appear that the contribution from the Green's function $G(\vec{r},\vec{r}\,',E_i-\omega)$ is small, because it has a pole at large negative frequency. To show that both term in equation 8.21 are important, we can use Eq. 8.19 and insert $1=f_j+(1-f_j)$ in it:

$$\chi_0=\sum_{ij}\left[f_i(1-f_j)(\chi_{ij}(\omega)-\chi_{ji}(\omega))+f_if_j(\chi_{ij}(\omega)-\chi_{ji}(\omega))\right]\ . \tag{8.22}$$

The last term in 8.22 cancels due to antisymmetry of the occupation numbers f_i and f_j, and we get

$$\chi_0=\sum_{ij}f_i(1-f_j)[\chi_{ij}(\omega)-\chi_{ji}(\omega)]\ . \tag{8.23}$$

Comparing equations 8.21 and 8.19, the Green's functions $G(\vec{r},\vec{r}\,',E)$ can be replaced by the partial (time ordered) Green's function $G^+(\vec{r},\vec{r}\,',E)$,

$$G^+(\vec{r},\vec{r}\,',E)=\sum_{m_{unocc}}\frac{\psi_m(\vec{r})\psi_m^*(\vec{r}\,')}{E-E_m+i\delta}\ , \tag{8.24}$$

which has a sum over unoccupied states only. Therefore, the presence of the second term in 8.21 ensures the cancelation of the contribution from occupied states. The Green's function $G^+(\vec{r},\vec{r}\,',E_i-\omega)$, however, is hard to calculate. While we can, in principle, use expressions given in Chapter 2, one runs into numerical difficulties in calculation of the irregular solution at high energies. One way to deal with this problem is put a Fermi function cutoff in Eq. 8.21 for the imaginary part of $\chi_0(\vec{r},\omega)$ and then do a Kramers-Kronig transform for the real part. This procedure explicitly cancels the occupied parts. The $\chi_0(\vec{r},\omega)$ then can be represented in the following form

$$\chi_0(\vec{r},\vec{r}\,',\omega)=\frac{1}{\pi}\int_{E_F}^{\infty}dE\,\frac{\mathrm{Im}\,\chi_0(\vec{r},\vec{r}\,',E)}{\omega-E+i\delta} \tag{8.25}$$

where

$$\mathrm{Im}\,\chi_0(\vec{r},\vec{r}\,',\omega)=\sum_{i_{occ}}\psi_i^*(\vec{r})\psi_i(\vec{r}\,')\,\mathrm{Im}\,G(\vec{r},\vec{r}\,',\omega+E_i)\ . \tag{8.26}$$

To conclude this section, we note that in the case of non-interacting electrons the expression for the absorption cross-section 8.1 with the response function $\chi_0(\vec{r},\vec{r}\,',\omega)$ given by Eqs. 8.25 and 8.26 is equivalent to Eq. 2.16.

8.2 Local field effects in extended systems

We start with the single-electron expression for the absorption coefficient 2.10. As we already discussed, it can be written in the form $\mu(\omega) = \mu_0(\omega)[1+\chi(\omega)]$, where $\mu_0(\omega)$ is a smooth atomic contribution and $\chi(\omega)$ is a fine structure. Since the local fields considered here are of atomic nature, it is a good approximation to consider their effect on the dipole matrix elements only. Similarly, we neglect the solid state effects on the independent-particle response function $\chi_0(\vec{r},\vec{r}\,',\omega)$. Then the x-ray absorption fine structure $\chi(\omega)$ is not affected and we can concentrate on the atomic background absorption part $\mu_0(\omega)$ only. In non-interacting case the latter is given by (dropping index 0 in μ_0)

$$\mu(\omega) = \frac{8\pi\, c\, k}{\omega} \sum_{i,L} \left| \langle i|\phi^{ext}|R_L\rangle \right|^2 \theta(\omega + E_i - E_F) \tag{8.27}$$

which we can rewrite in matrix form as

$$\mu(\omega) = \frac{8\pi\, c\, k}{\omega} \sum_{i,L} |M_{iL}(\omega)|^2\, \theta(\omega + E_i - E_F) \tag{8.28}$$

where

$$M_{iL}(\omega) = \langle i|\phi^{ext}|R_L\rangle = \int d\vec{r}\psi_i^*(\vec{r})\phi^{ext}(\vec{r},\omega)R_L(\vec{r},\omega+E_i)\,. \tag{8.29}$$

As it follows from Eq. 8.13, the local field effect can be accounted for by using the self-consistent field ϕ^{scf} instead of ϕ^{ext} in Eq. 8.29, so that matrix elements $M_{iL}(\omega)$ are substituted by the screened matrix elements $\tilde{M}_{iL}(\omega)$.

The self-consistent field ϕ^{scf} is obtained by solving Eqs. 8.7- 8.11. The first step is to calculate the non-interacting correlation function

$$\chi_0(\vec{r},\vec{r}\,',\omega) = \sum_i \psi_i^*(\vec{r}\,')\psi_i(\vec{r}\,') \int_{E_F}^{\infty} \frac{dE}{\pi} \frac{\mathrm{Im}\, G(\vec{r},\vec{r}\,',E)}{\omega - E + E_i + i\delta} \tag{8.30}$$

Since we consider only atomic part of the absorption coefficient, in Eq. 8.30 it is sufficient to use the central atom Green's function

$$\mathrm{Im}\, G(\vec{r},\vec{r}\,',E) = -2k \sum_L R_L(\vec{r},E) R_L{}^*(\vec{r}\,',E) \tag{8.31}$$

After $\chi_0(\vec{r},\vec{r}\,',\omega)$ is determined, one can iteratively solve Eqs. 8.7- 8.11 in real space to obtain $\phi^{scf}(\vec{r},\omega)$. However, using the outlined procedure in the straightforward way is computationally expensive. The problem lies in doing KK transform in Eq. 8.30 for each $(\vec{r},\vec{r}\,',\omega)$ point. Since the radial integrals at high energies require having a fine grid in r space, the total number of points for which we would have to calculate the KK integral is large.

To address this difficulty, we separate the photoelectron states into localized and delocalized atomic continuum parts, as discussed in Chapter 7. This can be achieved by using the projection operator $\hat{P}_{at}$ which projects onto a particular atomic orbital $\hat{P}_{at} = |\psi^{at}\rangle\langle\psi^{at}|$. The density matrix $\hat{\rho}(\vec{r},\vec{r}\,',E)$

$$\hat{\rho}(\vec{r},\vec{r}\,',E) = -\frac{2}{\pi}\mathrm{Im}G(\vec{r},\vec{r}\,',E) \tag{8.32}$$

can be separated into localized and continuum parts as follows

$$\hat{\rho} = \hat{\rho}^{loc} + \hat{\rho}^{cont}\,, \tag{8.33}$$

where

$$\begin{aligned} \hat{\rho}^{loc} &= \hat{P}_{at}\rho\,, \\ \hat{\rho}^{cont} &= (1-\hat{P}_{at})\hat{\rho} = 1 - \hat{\rho}^{loc}\,. \end{aligned} \tag{8.34}$$

Using Eqs. 8.34 and 8.31 we find that the localized part of the electron density matrix has the following form

$$\hat{\rho}^{loc}(\vec{r},\vec{r},',E) = \frac{4k}{\pi}\sum_L \left|\langle\psi_L^{at}|R_L\rangle\right|^2 \psi_L^{at}(\vec{r})\psi_L^{at}(\vec{r}\,')\,, \tag{8.35}$$

where the overlap integrals

$$\langle \psi_L^{at} | R_L \rangle = \int d\vec{r}\, \psi_L^{at*}(\vec{r})\, R_L(\vec{r}, E) \tag{8.36}$$

are functions of energy only.

Same separation also holds for matrix elements

$$M(\omega) = M^{loc}(\omega) + M^{cont}(\omega)\,, \tag{8.37}$$

where

$$M_{iL}^{loc}(\omega) = \langle \psi_L^{at} | R_L \rangle \langle i | \phi^{ext} | \psi_L^{at} \rangle\,. \tag{8.38}$$

and $M^{cont} = M - M^{loc}$.

Similarly, the localized part of the response function is given by

$$\chi_0^{loc}(\vec{r}, \vec{r}'\omega) = \sum_{i,L} \psi_i^*(\vec{r})\psi_i(\vec{r}\,')\psi_L^{at}(\vec{r})\psi_L^{at*}(\vec{r}\,') \int_{E_F}^{\infty} dE\, \frac{-2k}{\pi} \frac{|\langle \psi_L^{at} | R_L \rangle|^2}{\omega - E + E_i + i\delta}\,. \tag{8.39}$$

which we can rewrite by introducing an energy dependent matrix $\hat{\chi}_{iL}^0(\omega)$

$$\begin{aligned} \chi_0^{loc}(\vec{r}, \vec{r}'\omega) &= \sum_{i,L} \psi_i^*(\vec{r})\psi_i(\vec{r}\,')\psi_L^{at}(\vec{r})\psi_L^{at*}(\vec{r}\,')\, \hat{\chi}_{iL}^0(\omega)\,, \\ \hat{\chi}_{iL}^0(\omega) &= \int_{E_F}^{\infty} dE\, \frac{-2k}{\pi} \frac{|\langle \psi_{L'}^{at} | R_{L'} \rangle|^2}{\omega - E + E_i + i\delta}\,. \end{aligned} \tag{8.40}$$

The imaginary part of $\hat{\chi}_{iL}^0(\omega)$ is related to the the density of states

$$\mathrm{Im}\, \hat{\chi}_{iL}^0(\omega) = -2k \left| \langle \psi_L^{at} | R_L(\omega + E_i) \rangle \right|^2 \theta(\omega + E_i - E_F) \propto h_\ell(\omega + E_i)\,, \tag{8.41}$$

where $h_\ell(E)$ is the unoccupied part of the ℓ-projected density of states. As one can see, the localized part of the correlation function does not require doing KK integral at each point $(\vec{r}, \vec{r}\,')$ since the localized part of the photoelectron wave function can be naturally separated into energy and r dependent parts.

Let's assume for a moment that we deal with a bound photoelectron. In this case its wave function is fully localized and there are no delocalized continuum states.

The self-consistent field is then can be found from Eq. 8.11 where we keep only the localized part of the response function,

$$\phi^{scf}(\vec{r},\omega) = \phi^{ext}(\vec{r},\omega) + \tag{8.42}$$
$$\sum_{i,L} \int d\vec{r}\,' \psi_i^*(\vec{r}\,') K(\vec{r},\vec{r}\,',\omega) \psi_L^{at}(\vec{r}\,')\ \hat{\chi}^0_{iL}(\omega)\ \int d\vec{r}\,'' \psi_i(\vec{r}\,'') \phi^{scf}(\vec{r}\,'',\omega) \psi_L^{at*}(\vec{r}\,'')\ .$$

Instead of solving Eq. 8.42 iteratively in r space, one can rewrite this equation in terms of matrix elements and find the screened matrix elements, rather than the field itself, by matrix inversion.

It is convenient to introduce a renormalized matrix element

$$\mathcal{M}^{loc}_{iL} = \frac{M^{loc}_{iL}}{\langle \psi^{at}_L | R_L \rangle}\ . \tag{8.43}$$

Then, the analog of Eq. 8.42 for the renormalized matrix elements can be written in a simple matrix form

$$\tilde{\mathcal{M}}^{loc}(\omega) = \mathcal{M}^{loc}(\omega) + \hat{K}(\omega)\,\hat{\chi}^0(\omega)\,\tilde{\mathcal{M}}^{loc}(\omega)\ , \tag{8.44}$$

where

$$\hat{K}_{iL,i'L'}(\omega) = \int d\vec{r} \int d\vec{r}\,' \psi_i^*(\vec{r}) \psi_L^{at}(\vec{r}\,')\, K(\vec{r},\vec{r}\,',\omega)\, \psi_{L'}^{at*}(\vec{r})\, \psi_{i'}(\vec{r}\,')\ . \tag{8.45}$$

As a result, the renormalized matrix elements $\tilde{\mathcal{M}}^{loc}$ can be found by simple matrix inversion

$$\tilde{\mathcal{M}}^{loc} = (1 - \hat{K}\hat{\chi}^0)^{-1}\,\mathcal{M}^{loc}\ . \tag{8.46}$$

Now, we come back to the real situation for solids where delocalized states are present. Generally speaking, one cannot arrive to an equation for matrix elements in the form 8.46 because it is no longer possible to separate the energy and space dependent parts of the photoelectron wave function. Even though authors of [58] attempted to do such a separation in general case, we believe that it can lead to serious numerical problems, especially in case of Co, Ni, and Cu, where the contribution from

continuum states to XAS is significant, or even dominant like in case of Cu. Here, we would like to argue that the continuum states and localized states should be treated differently. Since the local field effects are atomic in nature, it is a reasonable approximation to include local field effects in the matrix element corresponding to transition to localized states only. The fast oscillating continuum states should not give any significant contribution to the screening of the external field, and should not be affected by the internal local fields since the transitions to the continuum states happen on the short-time (high-energy) scale. Therefore, it is reasonable to assume that the part of XAS that is due to transitions to these continuum states is not significantly modified by the dielectric polarization effects. Then, the total screened matrix elements can be found as

$$\tilde{M}(\omega) = \tilde{M}^{loc}(\omega) + M^{cont}(\omega)\,, \tag{8.47}$$

The kernel $K(\vec{r},\vec{r}\,',\omega)$ is given by equation 8.9. Since it was found that the exchange-correlation contribution to K results in less than 10% effect in absorption spectrum in case of rare gases [17] and even less important in case of transition metals [58], one can keep the dominant Coulomb term only. In this case, the matrix elements $\hat{K}_{iL,i'L'}$ are energy independent four particle matrix elements of electrostatic interaction [35].

8.3 Matrix elements of electrostatic interaction

To evaluate the matrix elements of electrostatic interaction $\hat{K}_{iL,i'L'}$, we need to calculate its angular part. It is convenient to introduce a new combined index Λ for each dipole allowed transition from initial state labeled $i = (\kappa_i, m_i)$ to a final state $L = (\kappa_f, m_f)$, so that $\Lambda = (\kappa_i, m_i; \kappa_f, m_f)$. One can use the usual expansion

$$\frac{1}{r_{12}} = \sum_{\nu=0}^{\infty} \frac{r_<^\nu}{r_>^{\nu+1}} \left[C^{(\nu)}(1)C^{(\nu)}(2)\right], \tag{8.48}$$

where $r_>$, $r_<$ are the greater or lesser of r_1 and r_2 , and $C^{(\nu)}$ is a tensor operator whose components are

$$C_q^{(k)} = \left(\frac{4\pi}{2\nu+1)}\right)^{\frac{1}{2}} Y_\nu^q \ , q = -\nu, -\nu+1, ..., \nu \tag{8.49}$$

Substituting in 8.45, after long calculations one arrives at the following expression for matrix $\hat{K}_{\Lambda\Lambda'}$ [35]

$$\hat{K}_{\Lambda,\Lambda'} = \delta(m_i + m_f^{'}, m_f + m_i^{'}) \sum_\nu d_\Lambda^\nu d_{\Lambda'}^\nu R_{\Lambda,\Lambda'}^\nu \ , \tag{8.50}$$

where d_Λ^ν are the angular coefficients

$$d_\Lambda^\nu = (-1)^{m_i+\frac{1}{2}}[j,j']^{\frac{1}{2}} \begin{pmatrix} j_i & \nu & j_f \\ \frac{1}{2} & 0 & \frac{1}{2} \end{pmatrix} \begin{pmatrix} j_i & \nu & j_f \\ -m_i & \epsilon & m_f \end{pmatrix} , \tag{8.51}$$

and $R_{\Lambda,\Lambda'}^\nu$ are the radial integrals

$$R_{\Lambda,\Lambda'}^\nu = \int dr \int dr' \psi_i^*(r)\psi_f^{at}(r)\frac{r_<^\nu}{r_>^{2\nu+1}}\psi_f^{at*}(r')\psi_{i'}(r') \tag{8.52}$$

The angular coefficients d_Λ^ν are non-vanishing only when $\Lambda = (j, m; j', m')$ satisfies the following parity selection rule in conjunction with the triangular condition on 3j symbols:

$$|j - j'| \leq \nu \leq j + j' \text{ with } j + j' + \nu = \begin{cases} \text{even} & \text{if } a = a' \\ \text{odd} & \text{if } a \neq a' \end{cases} , \tag{8.53}$$

where the parity $a = 1$ if $l = j - 1/2$ and $a = -1$ if $l = j + 1/2$.

For example, in case of $L_{2,3}$ edge absorption, the initial $2p_{1/2}$ and final $3d_{3/2}$ states have negative parity while the $2p_{3/2}$ and $3d_{5/2}$ states have positive parity. As a results, only those d_Λ^ν coefficients that have $\nu =$ odd are non-zero. The radial integrals 8.52 with $\nu = 3$ are approximately two orders of magnitude smaller the those with $\nu = 1$, so that only the dominant $\nu = 1$ term will be kept.

8.4 Comparison with the approach of Schwitalla and Ebert

Schwitalla and Ebert [58] used a similar approach to address the problem. However, there are several differences between the two approaches that will be discussed in this section. In their approach, they consider effects of electron correlations on the response function while keeping the x-ray field unchanged. As we already mentioned, the effect under consideration is basically a dielectric polarization effect. Therefore, we think that it is more natural to take it into account by modifying the dipole matrix element to reflect the screening of the external x-ray photon field. We think that our Eq. 8.44 has a clearer physical meaning and easier to work with than its analog derived by Schwitalla and Ebert who kept the photon field unchanged and put the many-electron effects into the effective response function. For example, in their approach it is no longer possible to split the absorption into L_3 and L_2 spectra. Some interesting discussions about the differences between these two formulations can be found in [131].

What is more important, we believe, is a flaw in their way of treating the continuum part of photoelectron wave function. In order to reduce the computational effort required to solve Eq. 8.15 they assumed that the normalized photoelectron wave function can factorized in the following form

$$\mathcal{R}_L(\vec{r},E) = \frac{R_L(\vec{r},E)}{D_L(E)}\,, \tag{8.54}$$

where

$$D_L(E) = \int_0^{R_N} d\vec{r}\ \ |R_L(\vec{r},E)|^2\ . \tag{8.55}$$

If the functions $\mathcal{R}_L(\vec{r},E)$ were smooth function of energy, then the KK transform required to calculate the real part of the response function could be done at each energy point only once, since $\mathcal{R}_L(\vec{r},E)$ could be evaluated at the Fermi level and then taken out of the integral over energies in Eq. 8.30. As a result, one would arrive at

the following matrix equations which we give here in our notations

$$\mu(\omega) = -\frac{4\pi c}{\omega}\,\mathrm{Im}\sum_{\Lambda,\Lambda'}\mathcal{M}^{\dagger}_{\Lambda}\,\hat{\chi}_{\Lambda,\Lambda'}\,\mathcal{M}_{\Lambda'}\,, \tag{8.56}$$

where

$$\hat{K}_{iL,i'L'}(\omega) = \int d\vec{r}\int d\vec{r}\,'\,\psi^{*}_{i}(\vec{r})\,\mathcal{R}_{L}(\vec{r},\omega{+}E_i)\,K(\vec{r},\vec{r}\,',\omega)\,\mathcal{R}^{*}_{L'}(\vec{r}\,',\omega{+}E_{i'})\,\psi_{i'}(\vec{r}\,'). \tag{8.57}$$

The matrix $\hat{\chi}_{\Lambda,\Lambda'}$ is connected with $\hat{\chi}^{0}_{\Lambda}$ through a matrix equation

$$\hat{\chi}(\omega) = \hat{\chi}^{0}(\omega) + \hat{\chi}^{0}(\omega)\,\hat{K}\,(\omega)\,\hat{\chi}(\omega)\,, \tag{8.58}$$

or

$$\hat{\chi}(\omega) = \left(1 - \hat{\chi}^{0}\,\hat{K}\right)^{-1}\,\hat{\chi}^{0}\,. \tag{8.59}$$

In Eqs. 8.58- 8.60 $\hat{\chi}^{0}$ should be understood as a diagonal matrix $\hat{\chi}^{0}_{\Lambda,\Lambda'} = \hat{\chi}^{0}_{\Lambda}\delta_{\Lambda,\Lambda'}$.

If we used the same factorization, Eq. 8.54, then instead of our Eqs. 8.44- 8.46 we would arrive at similar equations but with $D_L(E)$ instead of $\langle\psi^{at}_{L}|R_L\rangle$ and $\mathcal{M}_{iL} = M_{iL}/D_L$ instead of $\mathcal{M}^{loc}_{iL}$. The final expression for the absorption coefficient is then could be written as

$$\mu(\omega) = -\frac{4\pi c}{\omega}\sum_{\Lambda,\Lambda'}\tilde{\mathcal{M}}^{\dagger}_{\Lambda}\,\mathrm{Im}\,\hat{\chi}^{0}_{\Lambda,\Lambda'}\tilde{\mathcal{M}}_{\Lambda'}\,. \tag{8.60}$$

Eq. 8.60 is mathematically equivalent to Eq. 8.56.

However, such separation of the photoelectron wave function given by Eq. 8.54 is not exact. More specifically, it is the continuum part of the wave function which is not treated correctly and this leads to serious numerical problems with KK transform. If we use Eq. 8.54, the matrix $\hat{\chi}^{0}$ in Eq. 8.40 has the form

$$\hat{\chi}^{0}_{iL}(\omega) = \int_{E_F}^{\infty} dE\,\frac{-2k}{\pi}\,\frac{D^2_L(\omega+E_i)}{\omega - E + E_i + i\delta}\,, \tag{8.61}$$

with its imaginary part given by

$$\mathrm{Im}\,\hat{\chi}^{0}_{iL}(\omega) = -2kD^2_L(\omega+E_i)\,. \tag{8.62}$$

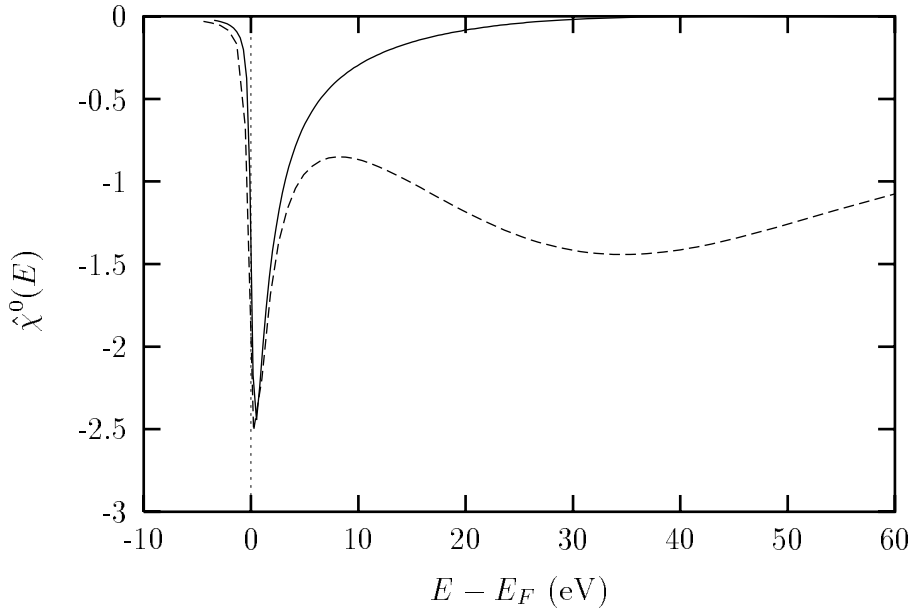

Figure 8.1: A typical element of the response matrix $\hat{\chi}^0(E)$ obtained using the projection on atomic states (solid line) and without (dashes).

Fig. 8.1 shows one of the elements of the matrix $\hat{\chi}^0$ calculated using Eq. 8.61. As one can see from Fig. 8.1, $\hat{\chi}^0$ goes to zero as a function of energy very slowly. Therefore, in order to calculate the real part of $\hat{\chi}^0$, one has to do the energy integral (KK transform) up to very high energies, in practice up to tens of thousands electron Volts, which is numerically impractical. Even more important, this slow decaying behavior of the matrix $\hat{\chi}^0$ is unphysical and appears to be an artifact of the invalid separation of the wave function into radial and energy dependent parts done using Eq. 8.54. Authors of [58] were able to obtain satisfactory results by using an arbitrary energy cutoff in the integral in Eq. 8.61. It is worth mentioning, hoverer, that they were somewhat helped by the following deficiency of their band structure approach. It seems that their calculation scheme fails do describe high energy continuum states, which is reflected by the fact that the calculated absorption coefficient quickly goes to zero at energies 40-50 eV above the edge. This, in turn, to some extend alleviates the problem of numerical integration in Eq. 8.61.

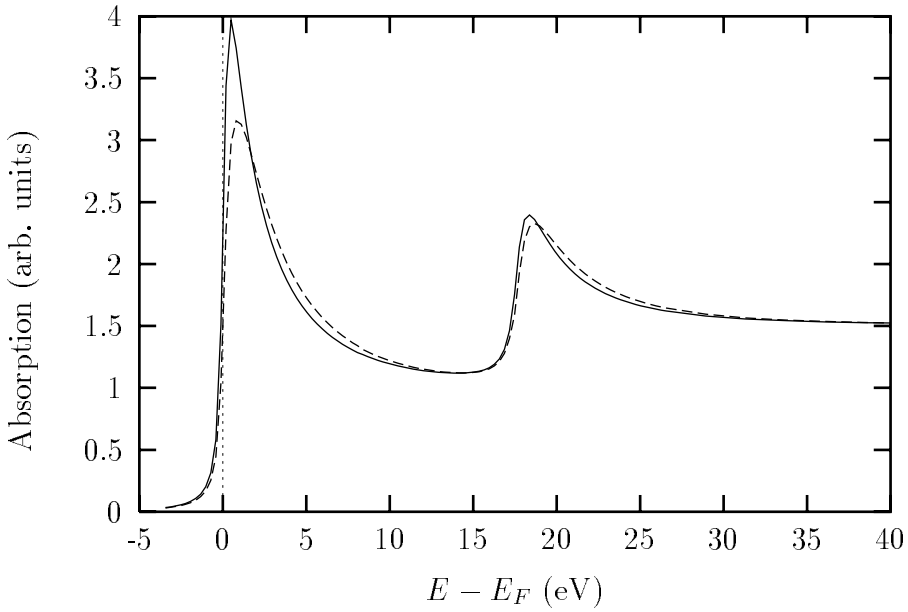

Figure 8.2: $L_{3,2}$ edge $\mu_0(E)$ in Ni calculated including local field effects (dashes) and in independent-particle approximation (solid line).

8.5 Results and discussions

The results of the calculation for several metals, Ni, V, and Ti, are presented in Figs. 8.5- 8.4. Since the effect of local fields on the fine structure $\chi(E)$ (not to be confused with matrix $\hat{\chi}(E)$) is expected to be small, we consider only the atomic part of the absorption coefficient, $\mu_0(E)$.

Inclusion of the dielectric polarization effect leads to several major changes in the absorption. Most noticeably, there is a significant redistribution of spectral weight between the L_3 and L_2 edges. In addition, there is a pronounced energy shift in the spectrum and an apparent asymmetric broadening of the absorption lines. These observed changes are somewhat expected from the work of Zangwill and Soven [17] for $4d$ photoabsorption in Xe and other rare gases. Our calculations show that the dielectric screening effects are relatively small in case of Cu, Co, and Ni, where the single-electron theory is already in a very good agreement with experimental data. At

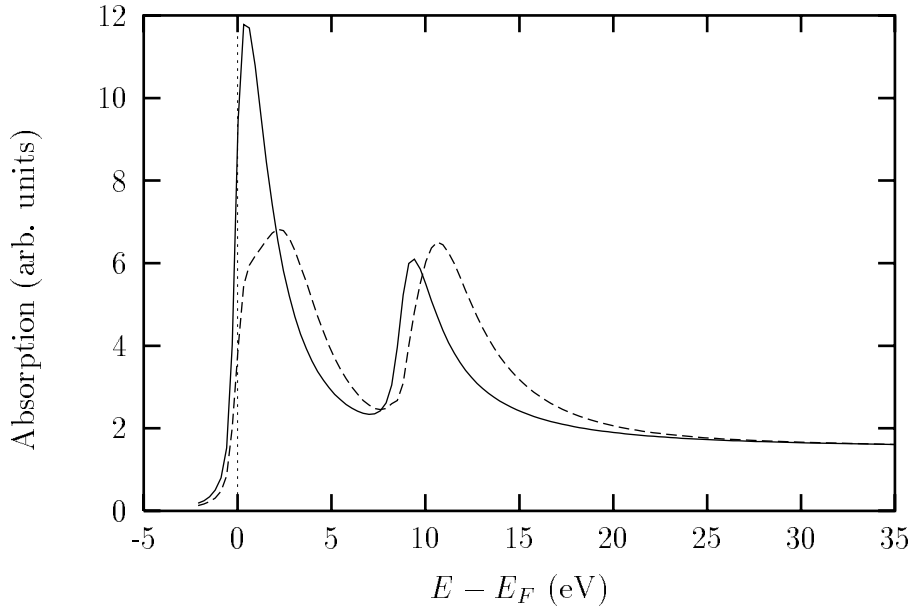

Figure 8.3: $L_{3,2}$ edge $\mu_0(E)$ in V calculated including local field effects (dashes) and in independent-particle approximation (solid line).

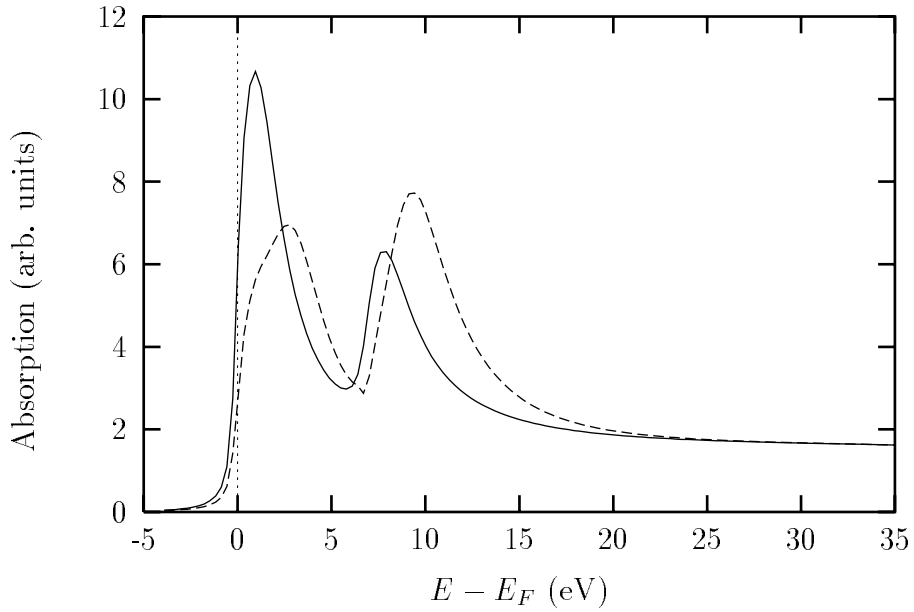

Figure 8.4: $L_{3,2}$ edge $\mu_0(E)$ in Ti calculated including local field effects (dashes) and in independent-particle approximation (solid line).

the same time, the inclusion of polarization effects results in a much better agreement with experiment, especially for the L_3/L_2 ratio, in case of light transition metals like V and Ti.

One way to interpret our results is to look directly at the local field [17] given by Eq. 8.11. Near the absorption edge, the imaginary part of the photon field is strongly screened in the region where the field has the largest overlap with the photoelectron wave function. As a result, the absorption cross-section at and just above the edge is reduced compared to that calculated in the single-electron picture. At higher energies, however, the real part of the local field becomes comparable with its imaginary part. As it was shown using an analogy with the driven harmonic oscillator [141], the complex induced field oscillates out of phase with the driving external x-ray field. As a result, the spectrum appears to be broader, shifted toward higher energies, and has a smaller amplitude at the its maximum.

We can use Vanadium to illustrate in more details all different changes in XAS caused by the polarization effect. We do it in terms of matrix elements rather than the fields, and separately for each of the two absorption edges. For the sake of clarity, here we keep only the leading first term in Eq. 8.46

$$\tilde{\mathcal{M}}^{loc} = (1 + \hat{K}\,\hat{\chi}^0)\,\mathcal{M}^{loc}\,. \tag{8.63}$$

We can rewrite Eq. 8.47 in the following form

$$\tilde{M}^{loc}_{\Lambda} = M^{loc}_{\Lambda} + \sum_{\Lambda'} \hat{K}_{\Lambda,\Lambda'}\,\hat{\chi}^0_{\Lambda'}\,M^{loc}_{\Lambda'}\,. \tag{8.64}$$

First, let us consider what would happen if the two edges, L_3 and L_2, were independent of each other. To achieve this we set the elements of the matrix $\hat{K}_{\Lambda,\Lambda'}$ to zero for all transition that involve mixing between the two absorption edges, $\hat{K}_{iL,i'L'} = 0$ if $i \neq i'$. The results are shown in Fig. 8.6. The solid line and short dashes are results obtained in single-particle approximation, dashes and dots are TDLDA calculations. Both edges demonstrate similar behavior, i.e. shifts in absorption peaks and

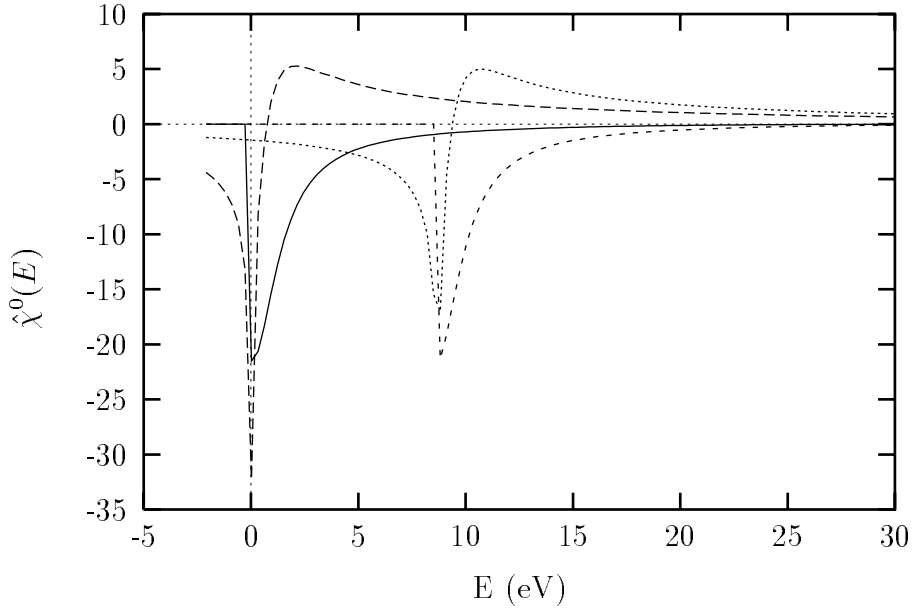

Figure 8.5: Real and imaginary part of $\hat{\chi}^0(E)$.

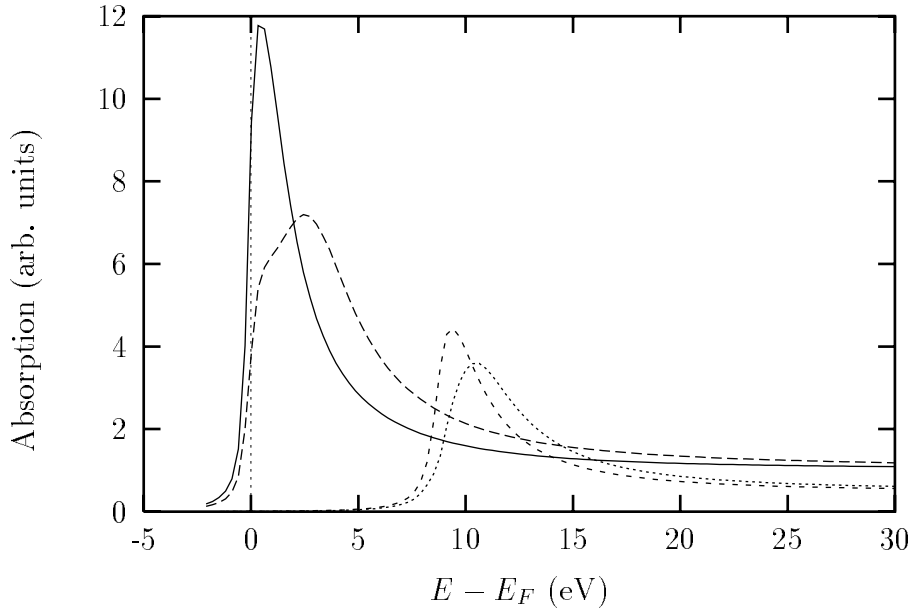

Figure 8.6: Local field effects at the L_3 and L_2 edges. The solid line and short dashes correspond to single-particle approximation, dashes and dots are TDLDA calculations.

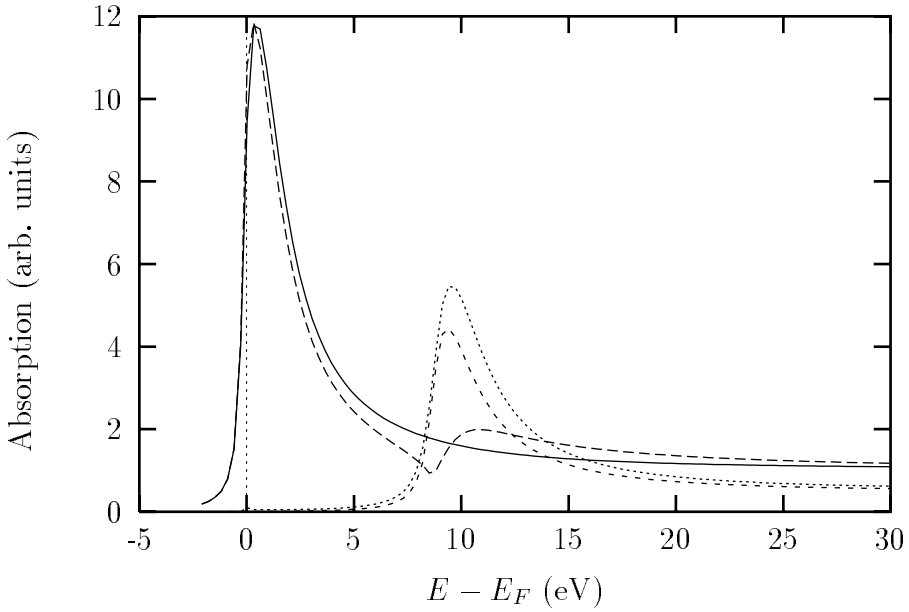

Figure 8.7: Effect of mixing between L_3 and L_2 edges. The solid line and short dashes correspond to single-particle approximation, dashes and dots are TDLDA calculations.

a suppression of their heights. Due to the presence of the complex matrix $\hat{\chi}^0$ on the right-hand side of Eq. 8.64, the screened matrix elements $\tilde{M}(E)$ are complex functions, with their real and imaginary parts oscillating out of phase reflecting the similar behavior of the self-consistent local field ϕ^{scf}. In Fig. 8.5 we show two elements of the matrix $\hat{\chi}^0$, one that corresponds to the L_3 edge, $\hat{\chi}^0_{L_3}$ and the other for the L_2 edge, $\hat{\chi}^0_{L_2}$. Both real and imaginary part are shown. The imaginary part of $\hat{\chi}^0$ is set to zero below the corresponding Fermi level. The origin on the energy axis corresponds to the L_3 edge Fermi level. Note that $\hat{\chi}^0_{L_2}$ is shifted toward higher energies with respect to $\hat{\chi}^0_{L_3}$ by the value of the spin-orbit splitting of the initial $2p_{1/2}$ core state.

In Fig. 8.7 we demonstrate the effect of mixing between the L_3 and L_2 absorption channel. To do this, we set $\hat{K}_{iL,i'L'} = 0$ for all transitions with $i = i'$. Eq. 8.64 then can be symbolically written as

$$\tilde{M}^{loc}_{L_3} = M^{loc}_{L_3} + \hat{K}_{L_3,L_2}\,\hat{\chi}^0_{L_2}\,M^{loc}_{L_2}\,, \tag{8.65}$$

$$\tilde{M}^{loc}_{L_2} = M^{loc}_{L_2} + \hat{K}_{L_2,L_3}\,\hat{\chi}^0_{L_3}\,M^{loc}_{L_3}\,. \tag{8.66}$$

As one can see from Fig. 8.7, there is a little change in the L_3 part of the spectrum far below the L_2 onset. At the onset of the L_2 edge, the $\tilde{M}_{L_3}$ matrix element have an addition resonance-like structure that is due to $\hat{\chi}^0_{L_2}$ in the second term in Eq. 8.65. The L_2 edge is affected to a larger extend. Most noticeable is the change in the height of the L_2 peak due to its mixing with the part of the L_3 spectrum that extends above the L_2 edge. The strength of the L_3 - L_2 edge mixing depends on several factors, most importantly on the value of the spin-orbit splitting in the initial state.

To summarize our results, in the Fig. 8.8 we plot the L_3/L_2 ratio calculated for all $3d$ transition metals. Clearly, inclusion of the local field effect leads to a much better agreement between theory and experiment, especially in case of elements on the left side of transition metals row. The worst agreement is found to be for Fe, probably due to approximate treatment of continuum states. It appears that the single-electron theory works reasonable well for Cu, Ni, and Co, thus justifying the quantitative procedure for obtaining hole counts and spin and orbital moments from XAS described in Chapters 6 and 7. It is also possible to modify that procedure to correct for many-body effects considered here. All we would have to do is to use a modified ratio $\tilde{\gamma}(E) = \tilde{\mu}_0(E)/\rho_0(E)$, with $\tilde{\mu}_0(E)$ being calculated using screened x-ray field.

8.6 Toward a better theory

Several improvements to the theory described above could be made in the future in order to make it applicable not only to transition metals, but to any system in general. The key approximation used by us was the separation of the photoelectron wave function into localized and continuum parts and the assumption that the matrix element for transitions to delocalized atomic continuum states could be calculated with unscreened x-ray electric field. To go beyond that approximation, we need to calculate the real part of $\chi(\vec{r}, \vec{r}\,', E)$ given by Eq. 8.30, which requires integration

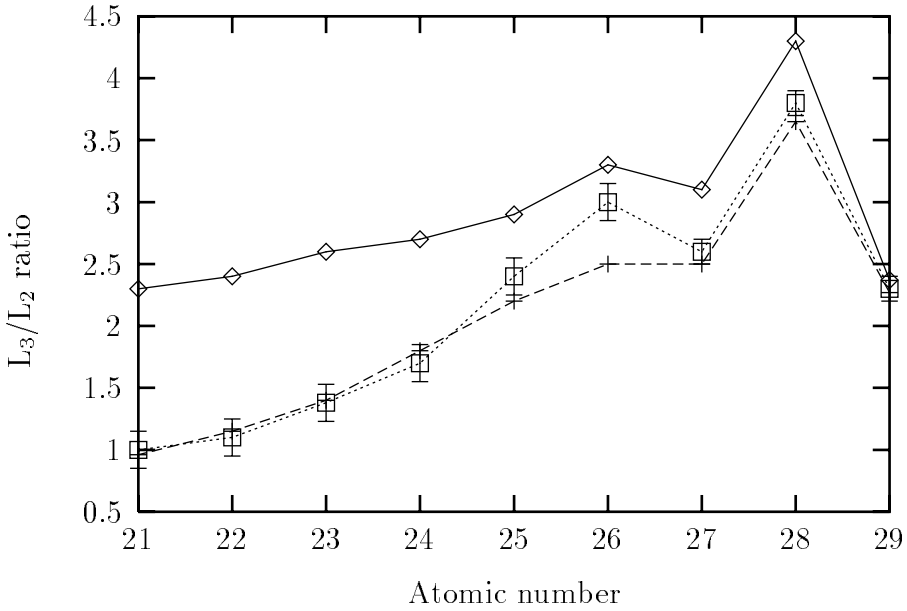

Figure 8.8: L_3/L_2 edge ratio, solid line and long dashes represent the theoretical ratios calculated with and without local field effects respectively, short dashes is experimental data.

up to very hight energies for all grid points (r, r', ω). However, the problem can be simplified if we use Eq. 8.7 directly to find the induced density $\delta\rho(\vec{r},\omega)$

$$\delta\rho(\vec{r},\omega) = \frac{1}{\pi}\int d\vec{r}\,' \int_{E_F}^{\infty} dE\, \frac{\mathrm{Im}\,\chi_0(\vec{r},\vec{r}\,',E)}{\omega - E + i\delta}\, \phi^{scf}(\vec{r}\,',E) \tag{8.67}$$

Using Eq. 8.30 and the expression for the imaginary part of the Green's function 8.31, we obtain after switching the order of integration

$$\delta\rho(\vec{r},\omega) = \sum_{i,L} \psi_i(\vec{r}) \int_{E_F}^{\infty} \frac{dE}{\pi} \frac{R_L(\vec{r},E)}{\omega - E + i\delta}\, f(\omega,E)\;, \tag{8.68}$$

where

$$f(\omega,E) = \int d\vec{r}\,\psi_i(\vec{r})\, R_L(\vec{r},E)\, \phi^{scf}(\vec{r},\omega)\;. \tag{8.69}$$

The induced field then can be found from Eq. 8.10. The function $f(\omega,E)$ already contains the integral over r', and solving Eq. 8.68 requires less computational effort.

Another approximation that we made was that we neglected the solid state effects on $\chi_0(\vec{r},\vec{r}\,',E)$ and used the central atom Green's function in expression in Eq. 8.31.

While we believe that this is a good approximation, one should be able to include the solid state effects by adding the scattering part of the Green's function, $\mathrm{Im}\, G_{Lc,L'c}$, in Eq. 8.31. Similarly, we assumed that the local field effects change the dipole matrix elements and the smooth atomic part of the absorption coefficient $\mu_0(E)$ only. The changes in the XAS fine structure $\chi(E)$ were neglected, but could be taken into account by using the screened reduced matrix elements in Eq. 2.18.

8.7 Interplay between core-hole interaction and polarization effects

In previous Chapters we analyzed the core-hole effect within the single-electron formalism. We concluded that the initial state rule (no core hole) is a preferable approximation in case of $L_{2,3}$ edge XAS in $3d$ transition metals. However, we could be only partially satisfied with the choice of the initial state rule, or any other "state rule" for that matter, since they are *ad hoc* and could be justified only by comparison with experiment.

Here we would like to come back to the problem of the electron - core hole interaction. From the work of Zangwill and Soven [17] and of Wendin[129], we know that LDA based self-consistent field approaches such as TDLDA can give an excellent description of photoionization cross section of outer and intermediate shells in free atoms. We note that TDLDA theory is based on the ground state LDA potential, that is with no account whatsoever for the core relaxation effects (initial state rule, no core hole). At the same time, the Hartree-Fock potential based approaches, such as RPAE, show that the core-hole relaxation process is very important and should be taken into account in order to achieve an agreement with experimental data. Therefore, the self-consistent Hartree-Fock calculations are usually performed for the system with a hole in the corresponding core level. The final state wave function then are different from the ground state ones since they are determined by the final state Hamiltonian that includes a relaxed core hole. Here we arrive at the important question posed by

Zangwill and Liberman[142] - what is the most appropriate way to describe both the core-hole relaxation and dielectric polarization effects within the TDLDA formalism? These authors performed TDLDA calculations for the case of $3d$ photoabsorption in Xe. Since, unlike the case of the $4d$ photoabsorption, they could not achieve a good agreement with experiment using the ground state TDLDA, they attempted to include the core-hole relaxation effect into their formalism. The calculations done with a relaxed core-hole potential did not bring the theory in agreement with experiment, erring this time in the opposite direction. However, they were able to achieve a good agreement when they employed the Slater "transition-state potential", i.e. with one half an electron removed from the core shell. However, there seems to be no justification (other than that it gives a better agreement with experiment) why the transition-state potential, or any potential with a fraction of an electron removed from the core level, should be used. In turn, Crljen and Wendin [130, 131] argued that if the core-hole is localized in the same region as the most compact excited orbital (screening), then the self-interaction in the LDA may be considered as simulating the relaxation effects. They demonstrated that in the core region there is close similarity between the LDA ground state potential and a relaxed, ionic V^{N-1} potential. This similarity is somewhat accidental and caused by a cancelation of the Hartree and exchange self-interactions within the LDA formalism. Crljen and Wendin argued that, while this cancelation is almost complete in case of $4d$ photoabsorption in Xe, it is not so in the case of the absorption from a deeper core level, where the relaxation effect should dominate. Then, one could use the Slater potential in TDLDA calculations of $3d$ photoionization in order to compensate for the incomplete cancelation between the self-interaction and relaxation.

Coming back to the problem of deep x-ray absorption considered in this work, what LDA potential should we use to correctly describe the interplay between core-hole relaxation and polarization? It seems that within the TDLDA formalism, as it is used in present form, the core-hole effects can be taken into account only in an *ad*

hoc way. The choice of the one-particle photoelectron orbitals (initial, final, transition state rule and etc.) ultimately depends on what prescription gives the best agreement between theory and experiment. Development of *ab initio* time-dependent approaches to excited states and response functions is a challenging problem.

One of the promising new directions is the GW approach [143, 39] (for a recent review see, e.g., [144]) and the two-particle (electron and core-hole) Bethe-Salpeter equation (BSE) [145, 146, 147, 148]. After the quasiparticle properties are determined from the GW description, one can allow quasielectrons and quasiholes to interact. The solution of this two-particle problem, called the Bethe-Salpeter equation, provides the exact two-particle Green's function. Alternatively, one can use a scheme similar to TDLDA but based on GW description instead of LDA. Unfortunately BSE is very difficult to implement numerically. Thus as yet there appears to be no tractable general procedure for XAS calculations that take into account core hole, polarization effects and inelastic losses.

Chapter 9

CONCLUSIONS

EXAFS, the oscillatory structure in the x-ray absorption coefficient beyond about 40 eV of threshold, is already well understood. At the same time, the quantitative analysis of XANES, the x-ray absorption near edge structure, is still not well developed and remains a challenge. In XANES region, the interaction of the photoelectron with its ion core, neighboring atoms, and other electrons is much stronger compared to its kinetic energy than in EXAFS. As a result, many processes that are not important in EXAFS are crucial for correct interpretation of XANES spectra. Since XANES is very sensitive to details of scattering potential the latter should be calculated self-consistently. The fast MS path expansion becomes divergent in XANES calculations due to the increase of the mean free path and backscattering amplitude. Thus, full MS calculations for a cluster of finite size are required. The computational time grows fast with the number of atoms in the cluster (N^3). Therefore, calculations for clusters larger than 200-300 atoms require special efforts. The transition of an electron from a deep core level into the unoccupied orbital is a complex and dynamic process that results in the creation of a core hole in the corresponding core level. A fully quantitative treatment of the core hole effect on XAS is not yet developed. Other many body effects, such as the photoelectron self-energy, local field effects, and atomic multiplets, might be also significant.

Despite all the complications, there is a great interest in XANES analysis because it directly probes the unoccupied part of the density of states. Thus, it provides a direct way of obtaining local chemical and electronic structure information of complex and disordered materials. In XANES region, L-shell absorption spectra are often the

most interesting and informative, especially in case of transition metals and metallic systems. Various XAS and XMCD sum rules have been used to investigate spin and orbital moments and hole counts in $3d$ transition metals. However, the practical application of the sum rules was complicated by the presence of contributions to the XAS from both localized orbitals and delocalized atomic continuum states. Their separation is typically done using *ad hoc* procedures which could not be well justified. There is also a question of whether x-ray absorption is a measure of the ground state or excited state DOS, and whether the sum rules are violated because of the many-body effects.

In this work we attempted to overcome the above mentioned difficulties of the XANES analysis and make it a quantitative tool for extracting chemical and electronic structure from experimental spectra. Most of the analysis is based on using the relativistic, self-consistent real space Green's function code FEFF8. We found the FEFF8 results for the electronic structure to be comparable, and for the XANES superior, to those obtained by full potential ground-state band structure methods.

We performed detailed analysis of the $L_{2,3}$ edge XANES of $3d$ transition metals and provided interpretation of the experimental data based on the results of single-electron multiple scattering calculations. We discussed several prescriptions for taking the effect of the core hole on x-ray absorption spectra. We found that in most cases the initial state rule (ground state, no core hole) calculations are in a better agreement with experimental data.

An interpretation of the spectral features in the Ni $L_{3,2}$ XANES and XMCD signals was presented, based on both one-electron multiple-scattering and atomic-multiplet calculations. Most of the observed features were reproduced by one-electron calculations. However, neither of these approaches was fully satisfactory. The necessity of both one electron and atomic-multiplet calculations to explain all features in the data demonstrates the need for a combined approach.

Overall, we achieved a good agreement between theory and experiment. This sug-

gested that a quantitative relationship could be established between XAS and XMCD spectroscopy and the unoccupied part of the local density of states. We developed a procedure for quantitative applications of the sum rules for x-ray absorption spectra. The approach is based on theoretical atomic calculations of transformations relating various experimental spectra to corresponding operator-spectral densities. This approach overcomes the difficulties of background subtraction and hole-count normalization of other sum rule analysis methods and yields quantitative values for spin- and orbital-moments from experimental absorption spectra. Although a number of approximations were made in the derivation of our approach, our theoretical tests verified that these approximations are reasonable and lead to systematic errors of only a few percent for spin and orbital moments.

Hole counts obtained from x-ray absorption spectra (XAS) are often interpreted in terms of free atom occupation numbers or Mülliken counts. However, such counts can violate the Pauli principle. We have proposed a quantitative technique, based on the use of projection operators, to subtract atomic delocalized states and hence to determine the electron configuration in term of RA counts from XAS. We demonstrated that renormalized-atom (RA) counts are a better choice to characterize the configuration of occupied electron states in molecules and condensed matter. Theoretical tests were performed for the s- and d-electrons in transition metals which verified that RA approach works well. The developed procedure has been incorporated in the new version of the FEFF8 code.

The one-electron theory of x-ray absorption near edge structure fails to describe the experimentally observed $L_{2,3}$ edge branching ratio in transition metals. We developed a formalism based on time dependent local density approximation theory that takes into account polarization-type many body effect. This effect, which is essentially a screening of the local x-ray field due to the Coulomb interaction, mostly affects dipole matrix elements. The effect is most important for soft x-rays with energies less than 1 keV. The developed TDLDA approach has been incorporated into the code

FEFF8. Results of our calculations for the $L_{2,3}$ edge branching ratio in 3d transition metals are in good agreement with experiment. The local field effects are found to be less important for transition metals with almost filled d band, such as Cu, Ni, Co. In these materials the single-electron theory works reasonable well. This justifies the quantitative procedure for obtaining hole counts and spin and orbital moments from XAS. It is also possible to modify our procedure to correct for the local field effect by calculating the atomic-like ratio $\gamma(E)$ using the the screened dipole matrix element.

While we achieved a significant progress toward full quantitative understanding of XANES, there is a lot of room for improvement and future work. In terms of the FEFF code development, several improvements can be made in order to make XANES calculations faster and more accurate. The treatment of scattering potentials must be improved by going beyond the muffin-tin approximation [6]. The FMS calculations should be done using more efficient algorithms, instead of the conventional approach based on matrix inversion. This work is already in progress [149]. The structural disorder and Debye-Waller factors in the FMS scheme are treated in an approximate way, as this also could be improved in the future.

Several improvements to our TDLDA formalism should be made in order to make it applicable not only to transition metals, but to any system in general. In our approach we separated the photoelectron wave function into localized and continuum parts and treated them differently. It is important to go beyond this approximation which would require to calculate the real part of $\chi(\vec{r},\vec{r}',E)$ by using KK transformation for each grid point (r,r',E). We could also include the solid state effects on $\chi(\vec{r},\vec{r}',E)$. Similarly, one should calculate the fine structure $\chi(E)$ using the screened reduced matrix elements.

One fundamental problem still remains unsolved, namely development of an *ab initio* time-dependent approach to excited states and response functions that would provide a general procedure for XAS calculations. A complete theory should take into account core hole, polarization effects and inelastic losses in an *ab initio* way

and on equal footing. At present, the core hole effects can be taken into account only in an *ad hoc* way. The choice of the one-particle photoelectron orbitals (initial, final, transition state rule and etc.) ultimately depends on what prescription gives the best agreement between theory and experiment. The question remains what LDA potential in the time dependent scheme one should use in order to correctly describe the interplay between core-hole relaxation and polarization. It seems that one would have to go beyond the LDA approximation. One of the possible new directions to resolve this problem is to determine quasiparticle properties by using the GW description, and then allow quasielectrons and quasiholes to interact. The solution of this two-particle problem, the Bethe-Salpeter equation, provides the exact two-particle Green's function. Unfortunately, the Bethe-Salpeter equation is very difficult to implement numerically. Thus as yet there appears to be no tractable general procedure for XAS calculations that take into account core hole, polarization effects and inelastic losses.

BIBLIOGRAPHY

[1] E.A. Stern and S.M. Heald. *Handbook on Synchrotron Radiation*, volume 1, chapter 10, Basic Principles and Applications of EXAFS. North-Holland Publishing Company, 1983.

[2] J.J. Rehr and R.C. Albers. *Rev. Mod. Phys*, **72**:621, 2000.

[3] C.R. Natoli, D.K. Misemer, S. Doniach, and F.W. Kutzler. *Phys. Rev. A*, **22**:1104, 1980.

[4] N. Binsted, R.W. Strange, and S.S. Hasnain. *Biochemistry*, **31**:12117, 1991.

[5] A. Filliponi and A. Di Cicco. *Phys. Rev. B*, **52**:15122, 1995.

[6] P. Blaha, K. Schwarz, and J. Luitz. *A Full Potential Linearized Augmented Plane Wave Package for Calculating Crystal Properties.* Karlheinz Schwarz, Techn. Universitat Wien, Austria, 1999.

[7] A.L. Ankudinov, B. Ravel, J.J. Rehr, and S.D. Conradson. *Phys. Rev. B*, **58**:7565, 1998.

[8] N.F. Mott. *Proc. R. Soc. Lond.*, **62**:416, 1949.

[9] M. Brown, R.E. Peierls, and E.A. Stern. *Phys. Rev. B*, **15**:738–744, 1977.

[10] R.E. Dietz L.F. Mattheiss. *Phys. Rev. B*, **22**:1663–1676, 1980.

[11] J. L. Erskine and E. A. Stern. *Phys. Rev. B*, **12**:5016, 1975.

[12] G. Schütz, W. Wagner, W. Wilhelm, P. Kienle, R. Zeller, R. Frahm, and G. Materlik. *Phys. Rev. Lett.*, **58**:737, 1987.

[13] J. Stöhr. *J. Magn. Magn. Mater.*, **200**:470, 1999.

[14] A.I. Nesvizhskii, A.L. Ankudinov, and J.J. Rehr. *Phys. Rev. B*, **63**:094412, 2001.

[15] A.L. Ankudinov, A.I. Nesvizhskii, and J.J. Rehr. *J. Synchrotron Rad.*, **8**:92, 2001.

[16] U. Von Barth and G. Grossman. *Solid State Commun.*, **32**:645, 1979.

[17] A. Zangwill and P. Soven. *Phys. Rev. A*, **21**:1561, 1980.

[18] R.D. Leapman and L.A. Grunes. *Phys. Rev. Lett.*, **45**:397–401, 1980.

[19] R.D. Leapman, L.A. Grunes, and P.L. Fejes. *Phys. Rev. B*, **26**:614, 1982.

[20] J.J. Rehr, J. Mustre de Leon, S.I. Zabinsky, and R.C. Albers. *J. Am. Chem. Soc.*, **113**:5135, 1991.

[21] S.I. Zabinsky. *Multiple Scattering Theory of XAFS*. PhD thesis, University of Washington, 1993.

[22] S.I. Zabinsky, J.J. Rehr, A. L. Ankudinov, R.C. Albers, and M.J. Eller. *Phys. Rev. B*, **52**:2995, 1995.

[23] A.L. Ankudinov and J.J. Rehr. *Phys. Rev. B*, **51**:1282, 1995.

[24] A.L. Ankudinov and J.J. Rehr. *Phys. Rev. B*, **56**:R1712, 1997.

[25] A.I. Nesvizhskii A.L. Ankudinov and J.J. Rehr. Theory and computation for synchrotron radiation spectroscopy. American Institute of Physics, 1999.

[26] W.L. Schaich. *Phys. Rev. B*, **8**:4028, 1973.

[27] P.A. Lee and J.B. Pendry. *Phys. Rev. B*, **11**:2795, 1975.

[28] J.P. Durham, J.B. Pendry, and C.H. Hodges. *Comput. Phys. Commun.*, **25**:193, 1982.

[29] T.A. Tyson, K.O. Hogson, C.R. Natoli, and M. Benfatto. *Phys. Rev. B*, **46**:5997, 1992.

[30] J.J. Rehr, C. H. Booth, F. Bridges, and S.I. Zabinsky. *Phys. Rev. B*, **49**:12 347, 1994.

[31] D.E. Sayers, E.A. Stern, and F.W. Lytle. *Phys. Rev. Lett.*, **27**:1204, 1971.

[32] E.A. Stern, D.E. Sayers, and F.W. Lytle. *Phys. Rev. B*, **11**:4836, 1975.

[33] C.A. Ashley and S. Doniach. *Phys. Rev. B*, **11**:1279, 1975.

[34] H. Ebert. *Rep. Prog. Phys.*, **59**:1665, 1996.

[35] I. P. Grant. *Advan. Phys.*, **19**:747, 1970.

[36] A.L. Ankudinov. *Relativistic Spin-dependent X-ray Absorption Theory.* PhD thesis, University of Washington, 1996.

[37] B.R. Judd. *Operator techniques in Atomic Spectroscopy.* McGraw-Hill, New York, 1963.

[38] A. Messiah. *Quantum Mechanics.* Interscience, New York, 1961.

[39] L. Heidin and S. Lundqvist. *Solid State Physics*, volume 23. Academic, New York, 1969.

[40] J.J. Rehr and R.C. Albers. *Phys. Rev. B*, **41**:8139, 1990.

[41] J.E. Müller, O. Jepsen, and J.W. Wilkins. *Solid. State Commun.*, **42**:365, 1982.

[42] R.C. Albers, A.K. McMahan, and J.E. Müller. *Phys. Rev. B*, **31**:3435, 1985.

[43] U. von Barth and L. Hedin. *J. Phys. C*, **5**:1629, 1972.

[44] A.I. Nesvizhskii and J.J. Rehr. *J. Synchrotron Rad.*, **6**:316, 1999.

[45] H. Ebert, J. Stöhr, S.S.P. Parkin, and A. Nilsson M. Samant. *Phys. Rev. B*, **53**:16067–16073, 1996.

[46] R. Zeller. *Z. Phys. B*, **72**:79, 1988.

[47] J.C. Slater. *Quantum theory of Molecules and Solids*. McGraw Hill, 1974.

[48] F. Luitz, M. Maier, C. Hébert, P. Schattschneider, P. Blaha, K. Schwarz, and B. Jouffrey. *Eur. Phys. J. B*, **21**:363–367, 2001.

[49] G. Duscher, R. Buczko, S.J. Pennycook, and S.T. Pantelides. *Ultramicroscopy*, **86**:355–362, 2001.

[50] E. A. Stern and J. J. Rehr. *Phys. Rev. B*, **27**:3351, 1983.

[51] J. Friedel. *Comm. Solid State Phys.*, **2**:21, 1969.

[52] M. Combescot and P. Nozières. *J. Phys. (Paris)*, **32**:9193, 1971.

[53] J. Fink, Th. Müller-Heinzerling, B. Scheerer, W. Speier, F.U. Hillebrecht, J.C. Fuggle, J. Zaanen, and G.A. Sawatzky. *Phys. Rev. B*, **32**:4899–4904, 1985.

[54] J. Barth, F. Gerken, and C. Kunz. *Phys. Rev. B*, **28**:3608, 1983.

[55] J. Zaanen, G.A. Sawatzky, J. Fink, W. Speier, and J.C. Fuggle. *Phys. Rev. B*, **32**:4905, 1985.

[56] W.G. Waddington, P. Rez, I.P. Grant, and C.J. Humphreys. *Phys. Rev. B*, **34**:1467, 1986.

[57] B.T. Thole and G. van der Laan. *Phys. Rev. B*, **38**:3158–3171, 1988.

[58] J. Schwitalla and H. Ebert. *Phys. Rev. Lett.*, **80**:4589, 1998.

[59] V. Eyert. *Density Functional Methods: Application in Chemistry and Material Science*. Willey, Sussex, 1997.

[60] A.I. Nesvizhskii, A.L. Ankudinov, J.J. Rehr, and K. Baberschke. *Phys. Rev. B*, **62**:15295, 2000.

[61] C.T. Chen, F. Sette, Y. Ma, and S. Modesti. *Phys. Rev. B*, **42**:7262, 1990.

[62] W.L. O'Brien and B.P. Tonner. *Phys. Rev. B*, **50**:12672, 1994.

[63] D. Arvanitis, M. Tischer, J. Hunter Dunn, F. May, N. Mårtensson, and K. Baberschke. *Spin-orbit influenced spectroscopies of magnetic solids*, page 259. Springer, Berlin, 1996.

[64] P. Srivastava, N. Haack, H. Wende, R. Chauvistré, and K. Baberschke. *Phys. Rev. B*, **56**:R4398, 1997.

[65] J. Vogel and M. Sacchi. *Phys. Rev. B*, **53**:3409, 1996.

[66] S.S. Dhesi, H.A. Dürr, G. van der Laan, E. Dudzik, and N. B. Brookes. *Phys. Rev. B*, **60**:12852, 1999.

[67] F. Wilhelm, P. Poulopoulos, P. Srivastava, H. Wende, M. Farle, K. Baberschke, M. Angelakeris, N. K. Flevaris, W. Grange, and J.-P. Kappler. *Phys. Rev. B*, **61**:8647, 2000.

[68] F. May, M. Tischer, D. Arvanitis, M. Russo, J. Hunter Dunn, H. Henneken, H. Wende, R. Chauvistré, N. Mårtensson, and K. Baberschke. *Phys. Rev. B*, **53**:1076, 1996.

[69] L.H. Tjeng, C. T. Chen, P. Rudolf, G. Meigs, G. van der Laan, and B. T. Thole. *Phys. Rev. B*, **48**:13378, 1993.

[70] N.B. Brooks, B. Sinkovic, L.H. Tjeng, J. B. Goedkoop, R. Hesper, E. Pellegrin, F. M. F. de Groot, S. Altieri, S. L. Hulbert, E. Shekel, and G. A. Zawatzky. *J. Electron Spectrosc. Relat. Phenom.*, **92**:11, 1998.

[71] M. Magnuson, A. Nilsson, M. Weinelt, and N. Mårtensson. *Phys. Rev. B*, **60**:2436, 1999.

[72] T. Jo and G.A. Sawatzky. *Phys. Rev. B*, **43**:8771, 1991.

[73] G. van der Laan and B.T. Thole. *J. Phys.: Condens. Matter*, **4**:4182, 1992.

[74] F. de Groot. *J. Electron Spectrosc. Relat. Phenom.*, **67**:529, 1994.

[75] G.Y. Guo. *Phys. Rev. B*, **57**:10295, 1998.

[76] N.V. Smith, C. T. Chen, F. Sette, and L. F. Mattheiss. *Phys. Rev. B*, **46**:1023, 1992.

[77] H. Ebert, P. Strange, and B. L. Gyoffy. *J. Appl. Phys.*, **63**:3055, 1988.

[78] H. Ebert and R. Zeller. *Phys. Rev. B*, **42**:2744, 1990.

[79] T. L. Loucks. *Augmented Plane Wave Method.* W. A. Benjamin, Inc., 1967.

[80] G. van der Laan, S. S. Dhesi, E. Dudzik, J. Minar, and H. Ebert. *J. Phys. Condens. Matter*, **12**:L275, 2000.

[81] H. Wende, P. Srivastava, D. Arvanitis, F. Wilhelm, L. Lemke, A. Ankudinov, J. J. Rehr, J. W. Freeland, Y. U. Idzerda, and K. Baberschke. *J. Synchrotron Rad.*, **6**:696, 1999.

[82] W.L. O'Brien, B.P. Tonner, G. R. Harp, and S.S.P. Parkin. *J. Appl. Phys.*, **76**:6462, 1994.

[83] O. Eriksson, A.M. Boring, R.C. Albers, G.W. Fernando, and B.R. Cooper. *Phys. Rev. B*, **45**:2868, 1992.

[84] S.S. Dhesi, H. A. Dürr, E. Dudzik, G. van der Laan, and N. B. Brookes. *Phys. Rev. B*, **61**:6886, 2000.

[85] B.I. Min, A.J. Freeman, and H.J.F. Jansen. *Phys. Rev. B*, **37**:6757, 1988.

[86] N.R. Bernhoeft, G.G. Lonzarich, P.W. Mitchell, and D. Mc Paul. *Phys. Rev. Lett.*, **62**:657, 1989.

[87] D.A. Muller, S. Subramanian, P. E. Batson, S. L. Sass, and J. Silcox. *Phys. Rev. Lett.*, **75**:4744, 1995.

[88] L.-S. Hsu, K.-L. Tsang, and S.-C. Chung. *Mat. Res. Soc. Symp. Proc.*, **437**:53, 1996.

[89] Y.K. Chung, K.P. Lin, W.F. Pong, M.-H. Tsai, H.H. Hsieh, J.Y. Pieh, P.K. Tseng, J.F. Lee, and L.-S. Hsu. *J. Appl. Phys.*, **87**:1312, 2000.

[90] P. Rez, J.R. Alvarez, and C. Pickard. *Ultramictroscopy*, **78**:175, 1999.

[91] D. A. Muller, D.J. Singh, and J. Silcox. *Phys. Rev. B*, **57**:8181, 1998.

[92] L.-S. Hsu. *Phys. Rev. B*, **437**:10858, 1995.

[93] L.-S. Hsu, K.-L. Tsang, and S.-C. Chung. *J. Magn. Magn. Mater.*, **177**:1031, 1998.

[94] L.S. Hsu and A.I. Nesvizhskii. *J. Phys. Chem. Solids*, **62**:1103–1109, 2001.

[95] *Handbook of Lattice Spacings and Structures of Metals.* Pergamon, New York, 1958.

[96] R.V. Baranova. *Sov. Phys.-Cryst.*, **10**:24, 1965.

[97] U. Bovensiepen, F. Wilhelm, P. Srivastava, P. Poulopoulos, M. Farle, A. Ney, , and K. Baberschke. *Phys. Rev. Lett.*, **81**:2368, 1998.

[98] A. Ney, F. Wilhelm, M. Farle, P. Poulopoulos, P. Srivastava, and K. Baberschke. *Phys. Rev. B*, **59**:R3938, 1999.

[99] W.J. Antel Jr., F. Perjeru, and G. R. Harp. *Phys. Rev. Lett.*, **83**:1439, 1999.

[100] B.T. Thole, P. Carra, F. Sette, and G. van der Laan. *Phys. Rev. Lett.*, **68**:1943–1946, 1992.

[101] P. Carra, B. T. Thole, M. Altarelli, and X. Wang. *Phys. Rev. Lett.*, **70**:694–697, 1993.

[102] R. Wu, D. Wang, and A. J. Freeman. *Phys. Rev. Lett.*, **71**:3582, 1993.

[103] R. Wu and A. J. Freeman. *Phys. Rev. Lett.*, **73**:1994, 1994.

[104] G. van der Laan. *J. Synchrotron Rad.*, **6**:694, 1999.

[105] C. T. Chen, Y. U. Idzerda, H.-J. Lin, N. V. Smith, G. Meigs, E. Chaban, G. H. Ho, E. Pellegrin, and F. Sette. *Phys. Rev. Lett.*, **75**:152, 1995.

[106] D. H. Pearson, C. C. Ahn, and B. Fultz. *Phys. Rev. B*, **47**:8471, 1993.

[107] I. Coulthard and T. K. Sham. *Phys. Rev. Lett.*, **77**:4824, 1996.

[108] H.H. Hsieh, Y.K. Chang, W.F. Pong, J.Y. Pieh, P.K. Tseng, T.K. Sham, I. Coulthard, S.J. Naftel, J.F. Lee, S.C. Chung, and K.L. Tsang. *Phys. Rev. B*, **57**:15204, 1999.

[109] J.E. Müller and J.W. Wilkins. *Phys. Rev. B*, **29**:4331, 1984.

[110] P. Carra, H. König, B. T. Thole, and M. Altarelli. *Physica B*, **192**:182, 1993.

[111] P. Strange and B. L. Gyorffy. *Phys. Rev. B*, **52**:R13091, 1995.

[112] R. Nakajima, J. Stöhr, and Y. U. Idzerda. *Phys. Rev. B*, **59**:6421, 1999.

[113] J. Lee, G. Lauhoff, C. Fermon, S. Hope, J. A. C. Bland, J. Ph. Shillé, G. van der Laan, C. Chappert, and P. Beauvillain. *J. Phys. Condens. Matter*, **9**:L137, 1997.

[114] D. Bonnenberg, K. A. Hempel, and H. P. J. Wijn. *Magnetic Properties of 3d, 4d, and 5d Elements, Alloys and Compounds*, volume **III/19a**, page 178. Springer-Verlag, Berlin, 1986.

[115] C. Kittel. *Phys. Rev.*, **76**:743, 1949.

[116] W. Grange, I. Galanakis, M. Alouani, M. Maret, J.-P. Kappler, and A. Rogalev. *Phys. Rev. B*, **62**:1157, 2000.

[117] F. de Groot. *Phys. Rev. B*, **42**:5459, 1990.

[118] A.N. Mansour, J.W. Cook Jr., and D. E. Sayers. *J. Phys. Chem.*, **88**:2330–2334, 1984.

[119] H.X. Wang, D.S. Patil, W.W. Gu, L Jacquamet, S. Friedrich, T. Funk, and S.P. Cramer. *J. Electron Spectrosc. Relat. Phenom.*, **114**:855–863, 2001.

[120] L. Hodges, R.E. Watson, and H. Ehrenreich. *Phys. Rev. B*, **10**:3953–3971, 1972.

[121] J. G. Norman Jr. *J. Chem. Phys.*, **61**:4630–4635, 1974.

[122] A.L. Ankudinov, J.J. Rehr, J.J. Low, and S.R. Bare. *J. Synchrotron Rad.*, **8**:578–580, 2001.

[123] M. Ya. Amusia. *Atomic Photoeffect.* Plenum Press, New York, 1990.

[124] V. Schmidt. *Rep. Prog. Phys.*, **55**:1483–1659, 1992.

[125] M. Ya. Amusia and N.A. Cherepkov. *Case Studies in Atomic Physics*, volume 5. New York: Plenum, 1975.

[126] H.P. Kelly, S.L. Carter, and B.E. Norum. *Phys. Rev. A*, **25**:2051–2055, 1982.

[127] G. Wendin. *New Trends in Atomic Physics*. Amsterdam: North-Holland, 1983.

[128] M.J. Stott and E. Zaremba. *Phys. Rev. A*, **21**:12, 1980.

[129] G. Wendin. *Phys. Rev. Lett.*, **53**:724, 1984.

[130] Z. Crljen and G. Wendin. *Phys. Scr.*, **32**:359–370, 1985.

[131] Z. Crljen and G. Wendin. *Phys. Rev. A*, **35**:1555–1570, 1987.

[132] W. Ekardt. *Phys. Rev. Lett.*, **52**:1925–1928, 1984.

[133] K. Sturm, E. Zaremba, and K. Nuroh. *Phys. Rev. B*, **42**:6973–6992, 1990.

[134] E. Zaremba and K. Sturm. *Phys. Rev. Lett.*, **66**:2144–2147, 1991.

[135] A. Rubio, J.A. Alonso, X. Blase, L.C. Malbas, and S.G. Louie. *Phys. Rev. Lett.*, **77**:247–250, 1996.

[136] L. Serra and A. Rubio. *Phys. Rev. Lett.*, **78**:1428–1431, 1997.

[137] K. Yabana and G.F. Bertsch. *Phys. Rev. A*, **60**:3809–3814, 1999.

[138] I. Vasiliev, S. Ögüt, and J. Chelikowsky. *Phys. Rev. Lett.*, **82**:1919–1922, 1999.

[139] I. Campillo, A. Rubio, and J.M. Pitarke. *Phys. Rev. B*, **59**:12 188 – 12 191, 1999.

[140] E.K.U. Gross, J.F. Dobson, and M. Petersilka. *Density Functional Theory*, page 81. Springer-Verlag, Heidelberg, 1996.

[141] A. Zangwill and P. Soven. *J. Vac. Sci. Technol.*, **17**:159–163, 1980.

[142] A. Zangwill and D.A. Liberman. *J. Phys. B*, **17**:L253–L257, 1984.

[143] L. Heidin. *Phys. Rev.*, **139**:796, 1965.

[144] F. Aryasetiawan and O. Gunnarsson. *Reports on Progress in Physics*, **61**:237, 1998.

[145] L.X. Benedict, E.L. Shirley, and R.B. Bohn. *Phys. Rev. Lett.*, **80**:4514–4517, 1998.

[146] M. Rohlfing and S.G. Louie. *Phys. Rev. Lett.*, **81**:2312–2315, 1998.

[147] S. Albrecht, L. Reining, R. Del Sole, and G. Onida. *Phys. Rev. Lett.*, **80**:4510–4513, 1998.

[148] E.L. Shirley. *Phys. Rev. Lett.*, **80**:794–797, 1998.

[149] A.L. Ankudinov, C.E. Bouldin, J.J. Rehr, J. Sims, and H. Hung. UW preprint, 2001.

VITA

Alexey I. Nesvizhskii was born in St. Petersburg, Russia, in 1971. He attended St. Petersburg State Technical University and graduated with honors in 1995. His specialization was in optical and electronic properties of semiconductor nanostructures. In 1995-1996, he was a graduate research assistant at the A.F. Ioffe Physico-Technical Institute in St. Petersburg. He started his graduate studies at the University of Washington in 1996. He received his Master of Science in Physics in 1997. He will be awarded Ph.D. in Physics in 2001.